

NUMERICAL INVESTIGATION OF CHARACTERISTICS OF PITCH AND
ROLL DAMPING COEFFICIENTS FOR MISSILE MODELS

A THESIS SUBMITTED TO
THE GRADUATE SCHOOL OF NATURAL AND APPLIED SCIENCES
OF
MIDDLE EAST TECHNICAL UNIVERSITY

BY

İSKENDER KAYABAŞI

IN PARTIAL FULFILLMENT OF THE REQUIREMENTS
FOR
THE DEGREE OF MASTER OF SCIENCE
IN
AEROSPACE ENGINEERING

SEPTEMBER 2012

Approval of the thesis

**NUMERICAL INVESTIGATION OF CHARACTERISTICS OF PITCH AND
ROLL DAMPING COEFFICIENTS FOR MISSILE MODELS**

Submitted by **İSKENDER KAYABAŞI** in partial fulfillment of the requirements for
the degree of **Master of Science in Aerospace Engineering Department, Middle
East Technical University** by,

Prof. Dr. Canan ÖZGEN
Dean, Graduate School of **Natural and Applied Sciences**

Prof. Dr. Ozan TEKİNALP
Head of Department, **Aerospace Engineering**

Assoc. Prof. Dr. Dilek Funda KURTULUŞ
Supervisor, **Aerospace Engineering Dept., METU**

Examining Committee Members:

Prof. Dr. Ozan TEKİNALP
Aerospace Engineering Dept., METU

Assoc. Prof. Dr. Dilek Funda KURTULUŞ
Aerospace Engineering Dept., METU

Prof. Dr. Yusuf ÖZYÖRÜK
Aerospace Engineering Dept., METU

Assist. Prof. Dr. Monier EL-FARRA
Flight Training Dept., UTAA

Ali AKGÜL, M.Sc.
Manager, ROKETSAN

Date: 10/09/2012

I hereby declare that all the information in this document has been obtained and presented in accordance with academic rules and ethical conduct. I also declare that, as required by these rules and conduct, I have fully cited and referenced all material and results that are not original to this work.

Name, Last name : İskender KAYABAŞI

Signature :

ABSTRACT

NUMERICAL INVESTIGATION OF CHARACTERISTICS OF PITCH AND ROLL DAMPING COEFFICIENTS FOR MISSILE MODELS

Kayabaşı, İskender

M.Sc., Department of Aerospace Engineering

Supervisor: Assoc. Prof. Dr. Dilek Funda Kurtuluş

September 2012, 112 Pages

In this thesis the characteristics of pitch and roll damping coefficients of missile models are investigated by using Computational Fluid Dynamics (CFD) techniques. Experimental data of NACA0012 airfoil, Basic Finner (BF) and Modified Basic Finner (MBF) models are used for validation and verification studies. Numerical computations are performed from subsonic to supersonic flow regimes. Grid refinement and turbulence model selection studies are conducted before starting the dynamic motion simulations. Numerical method of dynamic motion simulation is validated with a 2D NACA0012 airfoil. After the validation of numerical method, forced-oscillation motion is given to the BF and MBF models. In order to get deeper understandings about the characteristics of dynamic pitching and rolling motions, parametric studies are performed. The amplitude and frequency of forced-oscillation motions are investigated one by one. The effects of angle of attacks are also investigated for both pitching and rolling motions. The results of CFD simulations

are compared with experimental data obtained from different wind tunnel and free flight tests. It is seen from these comparisons that experimental and numerical results are in good agreement throughout the whole flow regime. In conclusion, the numerical method presented in this study is validated and can be used for the prediction of pitch and roll damping coefficient of any missile configurations.

Keywords: Computational Fluid Dynamics, Pitch Damping Coefficient, Roll Damping Coefficient, Reduced Frequency, Dynamic Motion

ÖZ

FÜZE MODELLERİ İÇİN YUNUSLAMA VE YUVARLANMA MOMENTİ SÖNÜMLENME KATSAYILARI KARAKTERİSTİĞİNİN SAYISAL OLARAK İNCELENMESİ

Kayabaşı, İskender

Yüksek Lisans, Havacılık ve Uzay Mühendisliği Bölümü

Tez Yöneticisi : Doç. Dr. Dilek Funda Kurtuluş

Eylül 2012, 112 Sayfa

Bu tezde füze modelleri için yunuslama ve yuvarlanma momenti katsayılarının karakteristiği Hesaplamalı Akışkanlar Dinamiği (HAD) ile incelenmiştir. Çalışmada kullanılan sayısal yöntemlerin doğrulanması ve geçerlenmesi için NACA0012, “Basic Finner (BF)” ve “Modified Basic Finner (MBF)” modellerinin deney verileri kullanılmıştır. Sayısal analizler ses-altı hızlardan ses-üstü hızlara kadar gerçekleştirilmiştir. Dinamik analizlere başlamadan önce çözüm ağı eniyileştirme ve türbülans modeli seçimi çalışmaları yapılmıştır. Dinamik hareket modellemesinde kullanılan sayısal yöntemi doğrulamak için NACA0012 kanat profili kullanılmıştır. Sayısal yöntemi doğruladıktan sonra BF ve MBF modellerine zorlanmış salınım hareketi yaptırılmıştır. Dinamik yunuslama ve yuvarlanma hareketi karakteristiğini daha iyi anlamak adına parametrik çalışmalar gerçekleştirilmiştir. Bu kapsamda sinusoidal salınım hareketinin büyüklüğü ve frekansı ayrı ayrı incelenmiştir. Her iki

hareket için hücüm açısının etkisine de bakılmıştır. HAD analizleri sonuçları farklı rüzgar tüneli ve uçuşlu test verileriyle kıyaslanmıştır. Kıyaslama sonucunda bütün akış rejimi boyunca sayısal sonuçların deney verileriyle uyum içinde olduğu görülmüştür. Bu çalışmanın sonucunda, dinamik hareketin modellenmesinde kullanılan sayısal yöntem doğrulanmış ve bu yöntem ile füzeler için yunuslama ve yuvarlanma moment sönümlenme katsayılarının hesaplanabileceği sonucuna varılmıştır.

Anahtar Kelimeler: Hesaplamalı Akışkanlar Dinamiği, Yunuslama Momenti Sönümlenme Katsayısı, Yuvarlanma Momenti Sönümlenme Katsayısı, İndirgenmiş Frekans, Dinamik Hareket

To My Wife

ACKNOWLEDGEMENTS

I would like to thank to my advisor Assoc. Prof. Dr. Dilek Funda Kurtuluş for her guidance, advice, criticism, encouragements and insight throughout the research.

I am very thankful to my mother Mrs. Güldane Kayabaşı, my brother Mr. İsa Kayabaşı and my sister Mrs. Fatma Keskin for their support during this study. I am also very thankful to my father Mr. Mehmet Kayabaşı for his endless support throughout my life. Without them, this work would not be completed.

I wish my deepest gratitude to my wife Mrs. Meltem Çulcu Kayabaşı for her understanding, patient and encouragements throughout the thesis.

I want to thank Mr. Berkan Mumcu and Mr. Suat Erdem Ertuğrul for their friendship during this study.

I also wish to thank Mr. Ali Akgül for his guidance and support during this study. I also would like to thank my colleagues in Aerodynamic Design and Analyses Department of ROKETSAN for all their help and support during the thesis.

TABLE OF CONTENTS

ABSTRACT	iv
ÖZ	vi
ACKNOWLEDGEMENTS	ix
TABLE OF CONTENTS	x
LIST OF FIGURES	xii
LIST OF TABLES	xviii
LIST OF SYMBOLS	xix
CHAPTERS	
1. INTRODUCTION	1
1.1 Stability	4
1.1.1 Static Stability	5
1.1.2 Dynamic Stability	6
1.2 Dynamic Derivatives	7
1.2.1 Pitch Damping Coefficient.....	8
1.2.2 Roll Damping Coefficient.....	10
1.3 Aim of Thesis	12
2. LITERATURE SURVEY.....	13
2.1 Pitch Damping Coefficient.....	13
2.2 Roll Damping Coefficient	16
3. NUMERICAL METHODS	18
3.1 Arbitrary Lagrangian-Eulerian Method.....	18
3.2 Governing Equations	19
3.2.1 Integral Compact Form of Governing Equations.....	20
3.2.2 Non-Dimensionalization of Governing Equations.....	23
3.3 Numerical Tools and Discretization.....	24
4. TEST CASE MODELS and CFD MODELING	27
4.1 Geometric Specifications and Solid Models	27
4.1.1 Test Case Model – 1.....	27
4.1.2 Test Case Model – 2.....	28
4.1.3 Test Case Model - 3	29

4.2	Grid Generation	30
4.3	Grid Quality Analysis	33
4.3.1	Skewness Ratio	34
4.3.2	Boundary Layer Analysis.....	36
4.4	Solution Domains and Boundary Conditions	40
4.4.1	Wall Boundary Condition	42
4.4.2	Pressure Far Field (Characteristic) Boundary Condition	43
4.4.3	Interface Boundary Condition.....	44
5.	VALIDATION STUDIES	45
5.1	Validation of Numerical Method	45
5.2	Grid Convergence Study for MBF model	58
5.3	Turbulence Model Selection for BF and MBF Models.....	61
5.3.1	Test Case Model – 2.....	62
5.3.2	Test Case Model - 3	64
5.4	Parametric Study	68
5.4.1	Pitching motion Simulations	68
5.4.2	Rolling Motion Simulations	87
6.	CONCLUSION AND DISCUSSION	106
	REFERENCES.....	109

LIST OF FIGURES

FIGURES

Figure 1.1 Coordinate system and sign convention	3
Figure 1.2 Graphical representation of static stability	5
Figure 1.3 Behavior of dynamically unstable missile	6
Figure 1.4 Behaviors of dynamically stable missile	6
Figure 1.5 Pitching motion with non-zero $\dot{\alpha}$ and zero q	8
Figure 1.6 Pitching motion with zero $\dot{\alpha}$ and non-zero q	8
Figure 3.1 Density-based algorithm [30]	26
Figure 4.1 Dimensions of BF test model [16].....	28
Figure 4.2 Solid model of BF test model	28
Figure 4.3 Dimensions of MBF test model [6], [7].....	29
Figure 4.4 MBF test model in T-38 Trisonic Wind Tunnel [7]	29
Figure 4.5 Solid model of MBF	30
Figure 4.6 Solution domain elements [33].....	30
Figure 4.7 Medium grid of NACA0012 airfoil	31
Figure 4.8 Medium volume grid of MBF model	32
Figure 4.9 Boundary layer grid of MBF model	32
Figure 4.10 Skewness ratio analysis	35
Figure 4.11 Turbulent boundary layer [36].....	36
Figure 4.12 u^+ vs. y^+ over a flat plate for turbulent flow [36].....	37
Figure 4.14 y^+ distribution on NACA0012 airfoil (Mach=0.755, $\alpha=0^\circ$)	39
Figure 4.15 y^+ distribution on MBF model (Mach=1.75, $\alpha=0^\circ$)	39
Figure 4.16 Solution domain and boundary conditions of NACA0012 for pitching motion simulations.....	40
Figure 4.17 Solution domain and boundary conditions of MBF model for pitching motion simulations.....	41
Figure 4.18 Solution domain and boundary conditions of MBF model for rolling motion simulations.....	42

Figure 5.1 Schematic view of pitching motion of NACA0012 airfoil.....	45
Figure 5.2 Sinusoidal pitching rates given to the NACA0012 airfoil.....	46
Figure 5.3 Pitching moment coefficient vs. angle of attack for different grids, Case-4.....	47
Figure 5.4 Pitching moment coefficient vs. angle of attack for different turbulence models, Case-4	48
Figure 5.5 Pitching moment coefficient vs. angle of attack, Case-1.....	48
Figure 5.6 Pitching moment coefficient vs. angle of attack, Case-2.....	49
Figure 5.7 Pitching moment coefficient vs. angle of attack, Case-3.....	50
Figure 5.8 Pitching moment coefficient vs. angle of attack, Case-4.....	50
Figure 5.9 Change of pitching moment coefficient and angle of attack with time for Case-1	51
Figure 5.10 Pressure distribution at different time steps, Case-1	52
Figure 5.11 Velocity distribution at different time steps, Case-1	52
Figure 5.12 Change of pitching moment coefficient and angle of attack with time for Case-2.....	53
Figure 5.13 Pressure distribution at different time steps, Case-2	53
Figure 5.14 Velocity distribution at different time steps, Case-2	54
Figure 5.15 Change of pitching moment coefficient and angle of attack with time for Case-3.....	55
Figure 5.16 Pressure distribution at different time steps, Case-3	55
Figure 5.17 Velocity distribution at different time steps, Case-3	56
Figure 5.18 Change of pitching moment coefficient and angle of attack with time for Case-4.....	57
Figure 5.19 Pressure distribution at different time steps, Case-4	57
Figure 5.20 Velocity distribution at different time steps, Case-4	58
Figure 5.21 Grid convergence for axial force coefficient (MBF model).....	59
Figure 5.22 Grid convergence for normal force coefficient slope (MBF model) .	60
Figure 5.23 Grid convergence for pitching moment coefficient slope (MBF model)	60
Figure 5.24 Residuals of steady simulations with medium grid (MBF model, Mach=1.0, $\alpha=0^\circ$).....	61

Figure 5.25 Axial force coefficient for different turbulence models (BF model $\alpha=0^\circ$)	62
Figure 5.26 Normal force coefficient slope for different turbulence models (BF model)	63
Figure 5.27 Pitching moment coefficient slope for different turbulence models (BF model)	63
Figure 5.28 Axial force coefficient for different turbulence models (MBF model, $\alpha=0^\circ$)	65
Figure 5.29 Normal force coefficient slope for different turbulence models (MBF model)	65
Figure 5.30 Pitching moment coefficient slope for different turbulence models (MBF model).....	66
Figure 5.31 Pressure distribution over MBF model and flow field (Mach=1.5, $\alpha=0^\circ$)	67
Figure 5.32 Mach number distribution over MBF model and flow field (Mach=1.5, $\alpha=0^\circ$).....	67
Figure 5.33 Sinusoidal pitching rates for different pitching rate amplitudes.....	69
Figure 5.34 Pitching moment coefficient vs. time for different pitching rate amplitudes (MBF model, Mach=0.6).....	69
Figure 5.35 Pitching moment coefficient vs. angle of attack for different pitching rate amplitudes (MBF model, Mach=0.6).....	70
Figure 5.36 Dynamic pitching moment coefficient vs. reduced frequency for different pitching rate amplitudes (MBF model, Mach=0.6).....	70
Figure 5.37 Pitching moment coefficient vs. time for different pitching rate amplitudes (MBF model, Mach=1.2).....	71
Figure 5.38 Pitching moment coefficient vs. angle of attack for different pitching rate amplitudes (MBF model, Mach=1.2).....	72
Figure 5.39 Dynamic pitching moment coefficient vs. reduced frequency for different pitching rate amplitudes (MBF model, Mach=1.2).....	72
Figure 5.40 Pitch damping coefficients of MBF model for different pitching rate amplitudes	73
Figure 5.41 Sinusoidal pitching rates for different pitching rate frequencies.....	74

Figure 5.42 Pitching moment coefficient vs. time for different pitching rate frequencies (MBF model, Mach=0.6).....	74
Figure 5.43 Pitching moment coefficient vs. angle of attack for different pitching rate frequencies (MBF model, Mach=0.6).....	75
Figure 5.44 Dynamic pitching moment coefficient vs. reduced frequency for different pitching rate frequencies (MBF model, Mach=0.6).....	76
Figure 5.45 Pitching moment coefficient vs. time for different pitching rate frequencies (MBF model, Mach=1.2).....	76
Figure 5.46 Pitching moment coefficient vs. angle of attack for different pitching rate frequencies (MBF model, Mach=1.2).....	77
Figure 5.47 Pitching moment coefficient vs. reduced frequency for different pitching rate frequencies (MBF model, Mach=1.2).....	77
Figure 5.48 Pitch damping coefficients of MBF model for different pitching rate frequencies	78
Figure 5.49 Pitching moment coefficient vs. time for different mean angle of attacks (MBF model, $X_{CG}=5D$, Mach=1.75)	79
Figure 5.50 Pitching moment coefficient vs. angle of attack, (MBF model, $X_{CG}=5D$, Mach=1.75)	80
Figure 5.51 Pitch damping coefficient vs. Mach number (BF model, $X_{CG}=5.5D$, $\alpha=0^\circ$)	81
Figure 5.52 Pitch damping coefficient vs. Mach number (MBF model, $X_{CG}=4.8D$, $\alpha=0^\circ$)	82
Figure 5.53 Pitch damping coefficient vs. angle of attack [39], (MBF model, $X_{CG}=5D$, Mach=1.75)	83
Figure 5.54 Pitch damping coefficient vs. angle of attack (BF model, $X_{CG}=6.1D$, Mach=1.96).....	83
Figure 5.55 Sinusoidal rolling rates for different rolling rate amplitudes.....	87
Figure 5.56 Rolling moment coefficient vs. time for different rolling rate amplitudes (BF model, Mach=0.7)	88
Figure 5.57 Rolling moment coefficient vs. roll angle for different rolling rate amplitudes (BF model, Mach=0.7)	88

Figure 5.58 Dynamic rolling moment coefficient vs. reduced frequency for different rolling rate amplitudes (BF model, Mach=0.7).....	89
Figure 5.59 Rolling moment coefficient vs. time for different rolling rate amplitudes (BF model, Mach=1.5)	90
Figure 5.60 Rolling moment coefficient vs. roll angle for different rolling rate amplitudes (BF model, Mach=1.5)	90
Figure 5.61 Dynamic rolling moment coefficient vs. reduced frequency for different rolling rate amplitudes (BF model, Mach=1.5).....	91
Figure 5.62 Roll damping coefficients of BF model for different rolling rate amplitudes	92
Figure 5.63 Sinusoidal rolling rates for different rolling rate frequencies.....	93
Figure 5.64 Rolling moment coefficient vs. time for different rolling rate frequencies (BF model, Mach=0.7)	93
Figure 5.65 Rolling moment coefficient vs. roll angle for different rolling rate frequencies (BF model, Mach=0.7)	94
Figure 5.66 Dynamic rolling moment coefficient vs. reduced frequency for different rolling rate frequencies (BF model, Mach=0.7).....	95
Figure 5.67 Rolling moment coefficient vs. time for different rolling rate frequencies (BF model, Mach=1.5)	95
Figure 5.68 Rolling moment coefficient vs. roll angle for different rolling rate frequencies (BF model, Mach=1.5)	96
Figure 5.69 Dynamic rolling moment coefficient vs. reduced frequency for different rolling rate frequencies (BF model, Mach=1.5).....	96
Figure 5.70 Roll damping coefficients of BF model for different rolling rate frequencies	97
Figure 5.71 Rolling moment coefficient vs. time for different angle of attacks (MBF model, Mach=1.75)	98
Figure 5.72 Rolling moment coefficient vs. roll angle for different angle of attacks (MBF model, Mach=1.75)	99
Figure 5.73 Rolling moment coefficient vs. reduced frequency for different angle of attacks (MBF model, Mach=1.75).....	99
Figure 5.74 Roll damping coefficient vs. Mach number (BF model, $\alpha=0^\circ$).....	100

Figure 5.75 Roll damping coefficient vs. angle of attack (MBF model, Mach=0.6)	101
Figure 5.76 Roll damping coefficient vs. angle of attack (MBF model, Mach=1.75)	102
Figure 5.77 Pressure distribution at the back of the BF model (Mach=0.7, A=200 rad/s, f=100 Hz)	105

LIST OF TABLES

TABLES

Table 1.1 Classification of missiles in terms of launching and impact type.....	1
Table 1.2 Classification of missiles in terms of control surfaces.....	2
Table 3.1 Non-dimensional form of variables	24
Table 4.1 Experimental conditions of pitching motion for NACA0012 airfoil....	28
Table 4.2 Grid convergence for NACA0012 airfoil	31
Table 4.3 Grid convergence for MBF model	32
Table 4.4 Skewness ratio parameters [34]	34
Table 4.5 Skewness ranges and cell quality [34]	35
Table 4.6 y^+ values and boundary layer zones [35]	37
Table 4.7 Geometric specifications of solution domains for NACA0012 airfoil .	40
Table 4.8 Geometric specifications of solution domains for BF and MBF models	41
Table 5.1 Pressure distribution and surface flow on MBF model (Mach=0.6, A=16 rad/s, f=62.5 Hz)	85
Table 5.2 Pressure distribution and surface flow on BF model (Mach=0.7, A=200 rad/s, f=100 Hz)	103

ABBREVIATIONS

A	: Amplitude of the oscillation
AC	: Aerodynamic Center
a_∞	: Speed of sound [m/s]
C_A	: Axial force coefficient
C_N	: Normal force coefficient
C_Y	: Side force coefficient
C_l	: Rolling moment coefficient
$C_{l\varphi}$: Static rolling moment coefficient slope [rad^{-1}]
$C_{l_{dynamic}}$: Dynamic rolling moment coefficient
C_{lp}	: Roll damping coefficient [rad^{-1}]
$C_{l_{static}}$: Static rolling moment coefficient
C_m	: Pitching moment coefficient
C_{m_α}	: Pitching moment coefficient slope [deg^{-1}]
$C_{m_{\dot{\alpha}}}$: Pitch damping coefficient due to rate of change of angle of attack [rad^{-1}]
C_{mq}	: Pitch damping coefficient due to pitch rate [rad^{-1}]
$C_{m_q} + C_{m_{\dot{\alpha}}}$: Pitch damping coefficient [rad^{-1}]
$C_{m_{dynamic}}$: Dynamic pitching moment coefficient
$C_{m_{dyn-\dot{\alpha}}}$: Dynamic pitching moment coefficient due to rate of change of angle of attack
$C_{m_{dyn-q}}$: Dynamic pitching moment coefficient due to pitch rate
$C_{m_{static}}$: Static pitching moment coefficient
C_n	: Yawing moment coefficient
C_{N_α}	: Normal force coefficient slope [deg^{-1}]
D	: Diameter of a missile [m]

f	: Frequency of the oscillation
fh	: First height thickness [m]
L	: Length of a missile [m]
L/D	: Length to Diameter
LES	: Large Eddy Simulation
L_{ref}	: Reference length (diameter of a missile) [m]
M_{∞}	: Free-stream Mach number
p	: Roll rate [rad/s]
PNS	: Parabolized Navier-Stokes
Pr	: Prandtl Number
q	: Pitch rate [rad/s]
r	: Yaw rate [rad/s]
RANS	: Reynolds Average Navier-Stokes
RBD	: Rigid Body Dynamics
RSM	: Reynolds Stress Model
SM	: Static Margin
S_{ref}	: Reference area (cross sectional area of a missile) [m ²]
T_{∞}	: Free-stream temperature [K]
u^+	: Non-dimensional velocity for boundary layers
V_{∞}	: Free-stream velocity [m/s]
X_{AC}	: Axial location of aerodynamic center
X_{CG}	: Axial location of center of gravity
y^+	: Non-dimensional spatial distance for boundary layers
2D	: Two Dimensional
3D	: Three Dimensional
α	: Angle of attack [deg]
$\dot{\alpha}$: Time rate of change of angle of attack [rad/s]
ρ_{∞}	: Free-stream density [kg/m ³]
Φ	: Roll angle [deg]
δ	: Control surface deflection (elevator or aileron) [deg]

CHAPTER 1

INTRODUCTION

Missiles, as compared to the airplanes, have increased ranges of speeds, altitude and maneuvering accelerations. These increased ranges may bring with them new aerodynamic problems such as aerodynamic heating, higher dynamic pressures, higher maneuvering accelerations, operating in the non-linear region of high angle of attacks, etc. Due to the needs of different mission profiles and also resulting from these wide ranges of aerodynamic problems, various missile model configurations are aroused.

Missiles are classified in different ways such as launching and impact type, control surfaces, trajectory, type of guidance system, propulsive system, etc. [1]. However, classification of missiles is generally done in terms of launching and impact type which is given in Table 1.1.

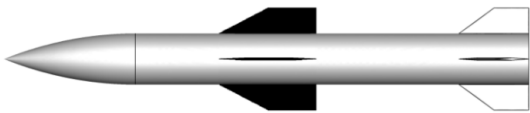
Table 1.1 Classification of missiles in terms of launching and impact type

AAM	Air-to-air missile
ASM	Air-to-surface missile
AUM	Air-to-underwater missile
SAM	Surface-to-air missile
SSM	Surface-to-surface missile
UUM	Underwater-to-underwater missile

The classification of missiles explained in Table 1.1 can be expanded. In addition to the classification of launching and impact type, missiles can be classified as guided

or unguided. Guided missiles are also classified in terms of control surfaces [2]. Classification of missiles in terms of control surfaces is given in Table 1.2.

Table 1.2 Classification of missiles in terms of control surfaces

Canard Control	
Wing Control	
Tail Control	

Besides conventional control systems, missiles may have alternative control systems such as side jets [3], [4] and thrust vector controls [5].

As it is seen in Table 1.2, a typical missile is consisted of an aerodynamic nose, cylindrical body, a lifting surface set and a control surface set. Missiles may have protuberances like umbilical, fairing, etc. However, in general most of the missiles have symmetric geometries.

Determination of aerodynamic forces and moments is an important task in missile industry. By knowing the accurate aerodynamic coefficients, the simulations of missile motions get closer to the real flights which will decrease production time and cost. However, prediction of aerodynamics of missiles is not an easy task because of wide ranges of aerodynamic problems such as aerodynamic heating, higher dynamic pressures, higher maneuvering accelerations, operating in the non-linear region of high angles of attack, etc. Moreover, various missile model configurations aroused from the needs of different mission profiles also result in difficulties for the determination of aerodynamics of missiles. In missile aerodynamics and control, as distinct from airplanes, different aerodynamic coefficients and sign convention systems are used. Non-dimensional aerodynamic forces and moments acting on a

missile for a six degree of freedom body-fixed coordinate system are shown in Figure 1.1.

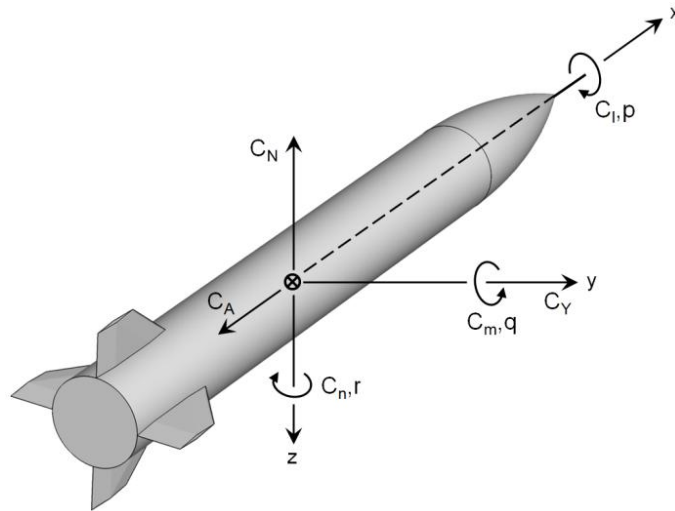


Figure 1.1 Coordinate system and sign convention

Whether guided or unguided, stability is one of the biggest problems for missiles because of larger changes in center of gravity (CG) location, speed and altitude. Prediction of static and dynamic stability of missiles is very important in terms of accuracy of impact of unguided missiles and maneuverability of guided missiles. In order to analyze the static and dynamic stability of missiles, static and dynamic aerodynamic coefficients have to be known accurately. Too many researches have been done for the calculation of static and dynamic aerodynamic coefficients of missiles for many years to predict their stability in static and dynamic conditions. These researches include theoretical, experimental and computational methods. Static aerodynamic coefficients are predicted very well for all missile models with experimental and numerical methods. Also, except for unconventional geometries, theoretical methods give very good results for all missile configurations. Prediction of dynamic aerodynamic coefficients, on the other hand, is not as easy as that of static aerodynamic coefficients. Theoretical methods are not applicable to all missile models and do not give good results even for conventional geometries. Wind tunnel measurements and free flight tests are very difficult, expensive and time consuming. Moreover, experiments may have lack of repeatability, in other words, same run for

the same missile model may exhibit great discrepancies [6]-[8]. Lack of faster and reliable prediction of dynamic aerodynamic coefficients is the biggest deficiency of the missile industry. In order to get faster and reliable results, numerical methods have been started to take place for the prediction of dynamic aerodynamic coefficients parallel to the advanced improvement on computer technology. Many researches focus on developing numerical methods for dynamic motion simulations. In this thesis, the characteristics of dynamic pitching and rolling motions of missiles are numerically investigated and the accuracy of numerical techniques developed for dynamic motion simulations are evaluated.

In the following parts, static and dynamic stability of missiles will be explained in details. The features of dynamic stability derivatives and their calculation methods will be presented. Finally, the aim and motivation of the thesis will be explained.

1.1 Stability

Forces and moments acting on a missile depend on the external geometry of the missile, deflection of control surfaces and flight conditions. Whether guided or unguided, determination of these aerodynamically generated forces and moments are very important to predict the path of the unguided missile or to control the guided missile. Nowadays, prediction of static aerodynamic forces and moments is not a difficult task. However, during the maneuver of the missile, the experienced forces and moments may be substantially different than that of the static ones. At this point, the changes in forces and moments with regard to the changes in flight conditions can be determined by missile stability derivatives. In addition to this, the changes of forces and moments with regard to time can also be determined by stability derivatives. These derivatives are classified as static and dynamic stability derivatives. Details of these stability derivatives are given in the following sub sections.

1.1.1 Static Stability

If the forces and moments acting on a missile resulted by any disturbances or control surface deflections tend to return the missile to its initial (equilibrium) position, the missile is said to be statically stable [9]. In order to be statically stable, the aerodynamic center of a missile should be behind the center of gravity location throughout the whole flow regimes [2]. In other words, for a statically stable missile, the pitching moment coefficient slope has to be negative which is shown in Figure 1.2.

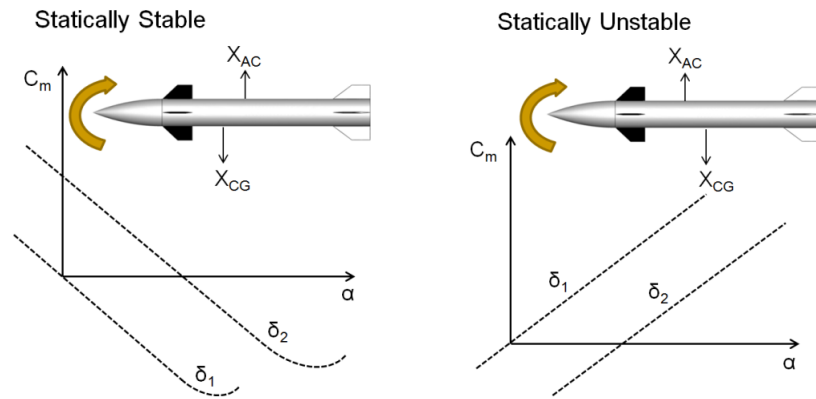


Figure 1.2 Graphical representation of static stability

Static stability of a missile is characterized by a concept called static margin Eq. (1-1) which is the ratio of axial distance between the center of gravity location and aerodynamic center over a diameter of a missile.

$$SM = \frac{X_{CG} - X_{AC}}{D} \quad (1-1)$$

If the SM value of a missile is less than zero the missile is said to be statically stable. If the SM value is greater than zero the missile is said to be statically unstable. If is equal to zero the missile is said to be neutrally stable.

1.1.2 Dynamic Stability

Dynamic stability is the behavior of a missile when disturbed from an original state of steady flight. If the missile is dynamically stable, the disturbing forces diminish with time and the missile gradually returns to its original state. If the missile is dynamically unstable, the disturbing forces and moments grow and, thus, the missile cannot return to its original state. The graphical representation of dynamic stability is given in Figure 1.3 and Figure 1.4.

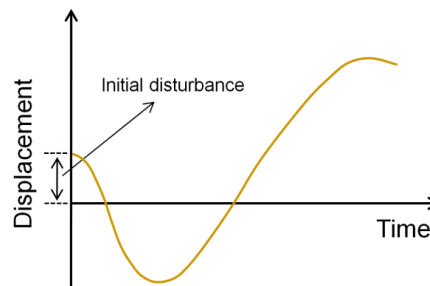


Figure 1.3 Behavior of dynamically unstable missile

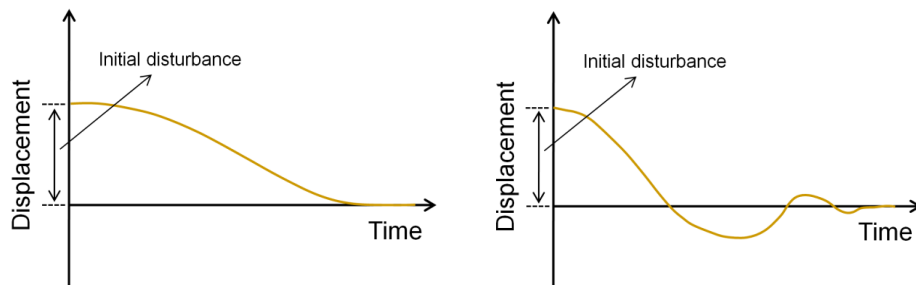


Figure 1.4 Behaviors of dynamically stable missile

As it is seen in Figure 1.4, the dynamically stable missile may show different behaviors to come back to its initial state. If the missile gradually returns to its original position like the one seen on the left graph in Figure 1.4, it is said to have monotonic dynamic stability. If the missile returns to its original state with oscillation like the one seen on the right graph in Figure 1.4, it is said to have oscillatory dynamic stability.

1.2 Dynamic Derivatives

The rates of change of aerodynamic forces and moments with respect to components of linear or angular velocities are called dynamic derivatives. These derivatives are very important in the analyses of dynamic stability of missiles. Especially, pitch and roll damping coefficients, which are the most dominant dynamic derivatives, are very crucial in missile design for evaluating dynamic stability of unguided missiles and maneuverability of guided missiles.

Pitch damping coefficient is usually treated as the sum of two individual coefficients that produce an aerodynamic moment proportional to the angular rate associated with the angle of attack. In fact, these two individual coefficients represent moments proportional to two different angular rates (q and $\dot{\alpha}$), although for many non-maneuvering flight trajectories, including those flown in ballistic aerodynamic ranges, these two angular rates are essentially equivalent. For this reason, pitch-damping coefficient sum is often treated as a single parameter.

Roll damping coefficient, which is another most important dynamic stability derivative, has an importance especially for the roll stability of unguided missiles and roll control of guided missiles. In order to decrease the effects of disturbances and asymmetric thrust generations, unguided missiles generally roll during their flights. Accurate prediction of roll damping coefficient is crucial for this type of missiles because roll stability of a missile has a great importance on precision of strike. Moreover, for guided missiles, accurate prediction of roll damping coefficients is again very important for the needs of higher roll maneuverability.

In the following parts, detailed information about pitch and roll damping coefficients will be presented.

1.2.1 Pitch Damping Coefficient

Pitching moment of a missile consists of two parts; static and dynamic. Dynamic pitching moment of a missile is also comprised of two parts. One of them is proportional to pitch rate (q) and the other one is proportional to the time rate of change of angle of attack ($\dot{\alpha}$). Dynamic pitching motion of the missile is better illustrated in Figure 1.5 and Figure 1.6.

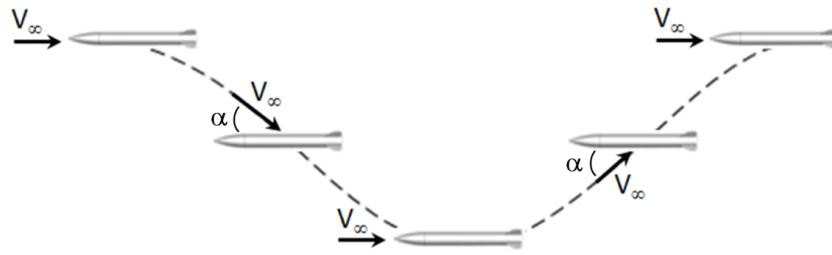


Figure 1.5 Pitching motion with non-zero α and zero q

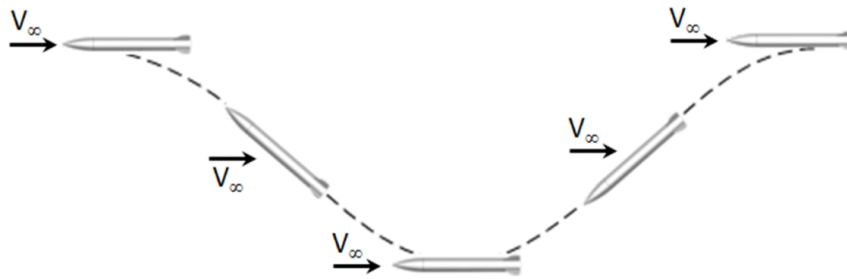


Figure 1.6 Pitching motion with zero α and non-zero q

Pitching moment coefficient of a missile consists of static and dynamic parts and can be shown as follows [10].

$$C_m = C_{m_{static}} + C_{m_{dynamic}} \quad (1-2)$$

Dynamic part of pitching moment coefficient is given in Eq. (1-3).

$$C_{m_{dynamic}} = \frac{\partial C_{m_{dyn-q}}}{\partial \left(\frac{qL_{ref}}{2V_{\infty}} \right)} \left(\frac{qL_{ref}}{2V_{\infty}} \right) + \frac{\partial C_{m_{dyn-\dot{\alpha}}}}{\partial \left(\frac{\dot{\alpha}L_{ref}}{2V_{\infty}} \right)} \left(\frac{\dot{\alpha}L_{ref}}{2V_{\infty}} \right) \quad (1-3)$$

Where, $C_{m_{dyn-q}}$ is the dynamic pitching moment coefficient resulted from pitch rate and $C_{m_{dyn-\dot{\alpha}}}$ is the dynamic pitching moment coefficient resulted from the time rate of change of angle of attack. The derivatives of these coefficients can be defined as follows:

$$\frac{\partial C_{m_{dyn-q}}}{\partial \left(\frac{qL_{ref}}{2V_{\infty}} \right)} = C_{m_q} \quad \text{and} \quad \frac{\partial C_{m_{dyn-\dot{\alpha}}}}{\partial \left(\frac{\dot{\alpha}L_{ref}}{2V_{\infty}} \right)} = C_{m_{\dot{\alpha}}} \quad (1-4)$$

Here, C_{m_q} and $C_{m_{\dot{\alpha}}}$ are the pitch damping coefficients. These pitch damping coefficients are generally treated as a sum, because, determination of these individual components is very difficult. Therefore, in most cases, q and $\dot{\alpha}$ are taken as identical. Therefore, by using the Eq. (1-3) and (1-4) dynamic pitching moment coefficient can be simply shown as follows.

$$C_{m_{dynamic}} = (C_{m_q} + C_{m_{\dot{\alpha}}}) \frac{qL_{ref}}{2V_{\infty}} \quad (1-5)$$

Finally, pitch damping coefficient can be found by using the Eq. (1-2) and (1-5).

$$C_{m_q} + C_{m_{\dot{\alpha}}} = \frac{C_{m_{dynamic}}}{\frac{qL_{ref}}{2V_{\infty}}} = \frac{C_m - C_{m_{static}}}{\frac{qL_{ref}}{2V_{\infty}}} \quad (1-6)$$

Where;

$$\frac{qL_{ref}}{2V_{\infty}} = k_q \quad (1-7)$$

Here; k_q is defined as the reduced frequency of pitching motion.

In wind tunnel experiments, forced-oscillation technique is used to calculate the pitch damping coefficients. In this study, same as wind tunnel measurements, sinusoidal pitching rates are given to the missile models. The sinusoidal pitching rates given to the test case models in present study are defined as follows.

$$q = A \cos(2\pi ft) \quad (1-8)$$

Here, A is the amplitude of pitching rate and f is the oscillation frequency.

1.2.2 Roll Damping Coefficient

Rolling moment coefficient of a missile consists of static and dynamic parts and it can be shown as follows [10].

$$C_l = C_{l_{static}} + C_{l_{dynamic}} \quad (1-9)$$

Dynamic part of rolling moment coefficient is given in Eq. (1-10).

$$C_{l_{dynamic}} = \frac{\partial C_{l_{dynamic}}}{\partial \left(\frac{pL_{ref}}{2V_{\infty}} \right)} \left(\frac{pL_{ref}}{2V_{\infty}} \right) \quad (1-10)$$

Here, $C_{l_{dynamic}}$ is the dynamic rolling moment coefficient resulted from roll rate. The derivative of this dynamic rolling moment coefficient can also be shown as follows.

$$\frac{\partial C_{l_{dynamic}}}{\partial \left(\frac{pL_{ref}}{2V_{\infty}} \right)} = C_{l_p} \quad (1-11)$$

Therefore, by using the Eq. (1-10) and (1-11), dynamic rolling moment coefficient can be simply shown as follows.

$$C_{l_{dynamic}} = C_{l_p} \left(\frac{pL_{ref}}{2V_{\infty}} \right) \quad (1-12)$$

Finally, roll damping coefficient can be found by using the Eq. (1-9) and (1-12).

$$C_{l_p} = \frac{C_{l_{dynamic}}}{pL_{ref}/2V_{\infty}} = \frac{C_l - C_{l_{static}}}{pL_{ref}/2V_{\infty}} \quad (1-13)$$

Where,

$$\frac{pL_{ref}}{2V_{\infty}} = k_p \quad (1-14)$$

Here; k_p is defined as the reduced frequency of rolling motion.

Again, forced-oscillation technique is used to calculate the roll damping coefficient both experimentally and numerically. Sinusoidal rolling rates are given to the missile models. The sinusoidal rolling rates given to the test case models in present study can be defined as follows.

$$p = A \cos(2\pi ft) \quad (1-15)$$

Here, A is the amplitude of rolling rate and f is the oscillation frequency.

1.3 Aim of Thesis

The importance of accurate and fast prediction of pitch and roll damping coefficients in missile design is stated before. As well as the expensive costs, the great discrepancies seen in wind tunnel measurements and free flight tests lead the missile designers to find the faster and reliable methods. For this purpose, with the increasing computer technology, researches have been focused on numerical methods where the motivation of this thesis comes from. The aim of this thesis is to investigate the characteristics of dynamic pitching and rolling motion of missiles and to evaluate the accuracy of numerical methods developed for the calculation of pitch and roll damping coefficients.

CHAPTER 2

LITERATURE SURVEY

Stability derivatives are the rates of change of aerodynamic force and moment coefficient with respect to angular or linear velocity components or time derivatives. In reality, these derivatives are partial derivatives of any degree and these derivatives have any number of independent variables of velocity components and time derivatives. These derivatives are the most important inputs to the dynamical analyses of missiles. Too many stability derivatives exist for missiles, however, most of them are negligible. The most important and dominant stability derivatives are the pitch and roll damping coefficients. In the following sub sections, researches conducted on pitch and roll damping coefficient calculations are presented.

2.1 Pitch Damping Coefficient

Pitch damping moment is very important in missile design for evaluating the dynamic stability of unguided missiles and maneuverability of guided missiles. However, determination of pitch damping coefficient is not as easy as the static aerodynamic coefficients. In order to determine the pitch damping coefficients too many theoretical, empirical, semi-empirical, numerical methods have been developed for years. While, theoretical, empirical and semi-empirical methods are fast and work well for simple and conventional geometries they do not work well for the unconventional and complex geometries. With the improvement of computer powers, numerical methods take places for the simulations of dynamic pitching motion of missiles. Besides this, numerical simulation results are used in the improvement of theoretical, empirical and semi-empirical methods.

Danberg and Weinacht [11] developed an approximate method for the prediction of pitch damping coefficients of axisymmetric geometries. Their method is based on the concepts of Slender Body Theory. They use correlation functions to improve the accuracy of the Slender Body Theory. Experimental database and validated CFD methods were used to derive the correlation functions. This simple method gives acceptable results for the conceptual design of axisymmetric bodies or for the parametric studies. Weinacht [12] predicted the individual components of the pitch damping coefficient sum. He did his computation around axisymmetric flight bodies by solving the thin layer Navier-Stokes equations with a Parabolized Navier-Stokes (PNS) technique. With this technique the unsteady problem changes into a steady problem by using a non-inertial rotating coordinate system because the fluid flow equations relative to this rotating coordinate system do not depend on time. He worked on Army Navy Spinning Rocket (ANSR) with different L/D ratios. He compared his results with Slender Body Theory results and experimental data. His results can be acceptable for the preliminary design of simple axisymmetric projectiles. Weinacht and Danberg [13] predicted the individual component of pitch damping coefficient for axisymmetric bodies by using the Sack's relations which is derived from Slender Body Theory. They used the PNS technique is used for solving the thin layer Navier-Stokes equations in a non-rotating frame of reference. They integrated the CFD results into a Sack's relations. They examined their techniques on ANSR projectile with different L/D ratios. Their methods give acceptable results for the conceptual design of simple axisymmetric geometries. Park et al [14], [15] used unsteady Euler equations in order to calculate the pitch damping coefficients of Basic Finner model. They also did the Navier-Stokes computations with $k-\omega$ turbulence models for the calculations of pitch damping coefficients of ANSR. They used forced harmonic and conic motions for the simulations. Their inviscid and viscous results show good agreement with experimental data. Murman [16] predicted the pitch damping coefficient by using a nonlinear, reduced frequency approach. In this method the response of a forced oscillation motion is simulated by using a single frequency constituent at the oscillation frequency. He used an inviscid cartesian mesh scheme with BF and MBF models. His results are quite close to the experimental data. Sahu [17] computed the dynamic derivatives of BF model by

using an unstructured, unsteady Navier-Stokes technique. He used an advanced coupled CFD/RBD technique which has the capability of grid motion. By using this technique, he simulated the motions of BF model on supercomputers. He extracted the dynamic derivatives from the numerical computations. Sahu [18] also computed the flight trajectories by using CFD/RBD techniques and he simultaneously predicted the unsteady free-flight aerodynamics of BF model. DeSpirito et al [19] evaluated the steady state Navier-Stokes methods for the calculation of dynamic stability derivatives. They evaluated the steady coning motion and transient planar motion for the calculation of pitch damping coefficients on three different projectiles. They get acceptable results for the preliminary design of the projectiles. Moore and Moore [20] developed two simple methods to predict pitch damping coefficient as a function of both angle of attack and Mach number. One of them was based on the static non-linear loads on the body and lifting surfaces. The other one was based on the improved linear value of pitch damping that was developed for the Aero-Prediction code (AP09). Silton [21] predicted the dynamic derivatives of a 0.50 caliber projectile by using multiple simulations which is called the virtual wind tunnel. She did time-accurate, moving mesh, Reynolds Average Navier-Stokes (RANS) analyses. She showed the great discrepancies between the experimental results as well as numerical results. Bhagwandin and Sahu [8] used the transient planar pitching and steady lunar coning method for predicting the dynamic derivatives of BF and MBF models. They showed that planar pitching method gives closer results to the experimental data than the steady lunar coning method for the subsonic, transonic and supersonic flow regimes. Lizhi et al. [22] numerically investigated the unsteady pitching characteristic of a missile. They are interested in the effects of position of rotation and reduced frequencies on lift, drag and pitching moment coefficient of missile models. In addition to the numerical studies, too many experimental and theoretical studies have been conducted for the calculations of pitch damping coefficients, because, calculation of dynamic aerodynamic coefficients is not as easy as calculation of static aerodynamic coefficients. Nowadays, there still exist great differences between the experimental results. Same run conducted in the same wind tunnel may have great discrepancies. In addition to this, the results of theoretical methods can be acceptable for only simple geometries

and they are applicable over limited flight conditions. Therefore, at this point, numerical calculation of pitch damping coefficients gains too much importance.

2.2 Roll Damping Coefficient

Roll damping moment is an opposing moment to the rolling motion of a missile, in other words, this moment tries to diminish the rolling motion. In real missile design, in some cases, roll damping moment is desired but in some cases this moment is not desired. In order to design or evaluate the roll stability of projectiles or guided missiles, roll damping moment should be determined accurately. In literature, many theoretical, empirical and semi-empirical methods have been developed for the prediction of this damping moment. The developed methods give faster and relatively good results for the simple and conventional geometries. However, these methods do not give good results for complex and unconventional geometries. In addition to this, accuracy of these methods is not good enough for the detailed design of missiles. These methods can only be used in the conceptual design phase. With the improvement of computer technology, numerical methods take places for the prediction of roll damping coefficients.

Gönç [23], in his Phd. Thesis, computed the roll damping coefficient for un-finned projectile with his 3D Navier-Stokes solver. He also used ALE method in order to simulate the dynamic motions. He implemented a Spalart-Allmaras turbulence model in his solver. After validating his code he tried to calculate the roll damping coefficient of un-finned projectile. He got acceptable results for this kind of difficult problem. Park et al [14], [15] used unsteady Euler equations in order to calculate the roll damping coefficients of BF model. He combined the dual-time stepping algorithm with an implicit multi-grid method. They calculated closer results to the experiment. Murman [16] also predicted the roll damping coefficient by using a nonlinear, reduced frequency approach. In this method the response of a forced oscillation motion is simulated by using a single frequency constituent at the oscillation frequency. He used an inviscid cartesian mesh scheme with BF and MBF models. His results are quite close to the experimental data. Morote and Liano [24]

developed a new method which is based on Slender Body Theory and strip. This method is applicable to all Mach numbers and angle of attacks. The calculated results showed that this method can be used in the preliminary design of simple missile models. Sahu [17] predicted the roll damping coefficient by using an unstructured, unsteady Navier-Stokes technique. He used an advanced coupled CFD/RBD technique which has the capability of grid motion. By using this technique, he simulated the motions of BF model on supercomputers and extracted the roll damping coefficients from the numerical computations. Sahu [18] also computed the flight trajectories by using CFD/RBD techniques and he simultaneously predicted the unsteady free-flight aerodynamics of Basic Finner model. DeSpirito and Heavey [25] tried to demonstrate the effects of CFD parameters for the prediction of Magnus and roll damping coefficient of projectiles. They showed that RANS computation is not adequate for the prediction of Magnus moments. They also showed that, time accurate RANS simulations are adequate enough with acceptable error margins for the prediction of roll damping coefficients. Moore and Moore [26] developed an approximate method which is a function of Mach number and angle of attacks. This method is valid for Mach numbers up to 20 and angle of attacks up to 90°. In this method, they tried to implement the effects of wing aspect ratio, stall, canard shed vortices, boat tail bodies, flare bodies and wing load due to roll. The results of this method can be acceptable in the preliminary design of the missiles. Siltan [21] tried to calculate the roll damping of a 0.50 caliber projectile with time-accurate, moving mesh, RANS simulations. She showed that RANS simulation is adequate for roll damping coefficient calculations. In addition to the numerical simulations, too many theoretical and experimental studies have been conducted for the calculations of roll damping derivatives. Theoretical methods may give good results for the simple conventional geometries but they do not give reliable results for the unconventional geometries. Experimental results do not have great discrepancies as that of pitch damping moment coefficients. However, it is still very difficult and expensive to calculate this coefficient with experiment. Therefore, in missile design, the accurate and cheapest way of roll damping coefficient calculation, numerical simulations take great importance.

CHAPTER 3

NUMERICAL METHODS

In this study, 3D, compressible, time-dependent, RANS equations are governed in an ALE frame of reference. Finite volume method is used to solve the numerical form of the governing equations with a second order discretization using FLUENT® [30] commercial software. The inviscid fluxes are evaluated with an upwind flux difference scheme Roe. In the following parts, details of governing equations, ALE method and discretization of the integral form of the equations will be presented.

3.1 Arbitrary Lagrangian-Eulerian Method

In fluid dynamics, the flow field is analyzed with two different methods which are the Lagrangian and Eulerian specifications. Particle tracking is the main idea of the Lagrangian specification of the flow field. In other words, the observer follows the fluid particles as it moves through space and time. In CFD applications of Lagrangian method, the computational mesh is attached to the fluid particles and moves with the local fluid velocity. In other words, each control volume is associated with the same fluid particles. In Eulerian specification of flow fields, the observer focuses on specific locations in space and observes the fluid particles passing through these specific locations as time passes. In CFD applications of Eulerian method, the computational mesh remains stationary and the fluid particles move from one control volume to another control volume.

The ALE method is the combination of Lagrangian and Eulerian methods in which the mesh motion can be chosen arbitrarily. This method was first mentioned by Hirt

et al. [25] in 1974 and since then many researchers have been used to handle the moving mesh CFD problems. Within this method, the conservation equations are modified to solve the moving mesh problems such that the grid velocities are integrated into the conservation equations. The modified form of the fluid flow equations appropriate for ALE method is explained in the following section.

3.2 Governing Equations

In this problem, the solution domain consists of two domains the inner and outer ones. The inner domain is the moving domain and the outer domain is the stationary domain. The integral forms of the governing equations are defined in non-inertial reference frame for both domains. These governing equations are given below [28].

Continuity:

$$\frac{\partial}{\partial t} \int_{\Omega} \rho d\Omega + \oint_S \rho (\vec{V} - \vec{V}_{C.V.}) \cdot d\vec{S} = 0 \quad (3-1)$$

Here,

$$\vec{V} = u\vec{i} + v\vec{j} + w\vec{k} \quad (3-2)$$

$$\vec{V}_{C.V.} = u_{C.V.}\vec{i} + v_{C.V.}\vec{j} + w_{C.V.}\vec{k} \quad (3-3)$$

\vec{V} is the fluid velocity, $\vec{V}_{C.V.}$ is the velocity of the moving volume Ω and S is the surface enclosed to this finite volume.

Conservation of momentum:

$$\frac{\partial}{\partial t} \int_{\Omega} \rho \vec{V} d\Omega + \oint_S (\rho \vec{V} \otimes \vec{V} + P\vec{I} - \rho \vec{V} \otimes \vec{V}_{C.V.}) \cdot d\vec{S} = \oint_S \tau_{ij} \cdot d\vec{S} \quad (3-4)$$

Here, $\vec{V} \otimes \vec{V}$ is the tensor product, P is the pressure.

Conservation of energy:

$$\begin{aligned} \frac{\partial}{\partial t} \int_{\Omega} \rho E d\Omega + \oint_S (\rho E \vec{V} + P \vec{V} - \rho E \vec{V}_{c.v.}) \cdot d\vec{S} \\ = \oint_S (\tau_{ij} \cdot \vec{V} - \dot{q}) \cdot d\vec{S} \end{aligned} \quad (3-5)$$

In Eq. (3-5) E is the total energy, \dot{q} is the heat transfer rate and τ_{ij} is the viscous shear stress tensor defined as:

$$\tau_{ij} = \mu \left[(\partial_j V_i + \partial_i V_j) - \frac{2}{3} (\vec{V} \cdot \vec{V}) \delta_{ij} \right] \quad (3-6)$$

3.2.1 Integral Compact Form of Governing Equations

The suitable form of governing equations for finite volume method is given below.

$$\frac{\partial}{\partial t} \int_{\Omega} \vec{U} d\Omega + \oint_S \vec{F} \cdot d\vec{S} = \oint_S \vec{Q} \cdot d\vec{S} \quad (3-7)$$

Where, \vec{U} is the conservative variables, \vec{F} is the convective flux and \vec{Q} is the viscous diffusive flux vectors. These vectors are as follows:

$$\vec{U} = \begin{bmatrix} \rho \\ \rho u \\ \rho v \\ \rho w \\ \rho E \end{bmatrix} \quad (3-8)$$

$$\vec{F} = \begin{bmatrix} \rho(\vec{V} - \vec{V}_{c.v.}) \\ (\rho\vec{V} \otimes \vec{V} + P\vec{I} - \rho\vec{V} \otimes \vec{V}_{c.v.}) \\ (\rho E(\vec{V} - \vec{V}_{c.v.}) + P\vec{V}) \end{bmatrix} \quad (3-9)$$

$$\vec{Q} = \begin{bmatrix} 0 \\ \tau_{ij} \\ (\tau_{ij} \cdot \vec{V} - \dot{q}) \end{bmatrix} \quad (3-10)$$

The convective flux vector \vec{F} can be defined as follows:

$$\vec{F} = F\vec{i} + G\vec{j} + H\vec{k} \quad (3-11)$$

Where;

$$F = \begin{bmatrix} \rho(u - u_{c.v.}) \\ \rho u(u - u_{c.v.}) + p \\ \rho v(u - u_{c.v.}) \\ \rho w(u - u_{c.v.}) \\ (\rho E + p)(u - u_{c.v.}) + u_{c.v.}p \end{bmatrix} \quad (3-12)$$

$$G = \begin{bmatrix} \rho(v - v_{c.v.}) \\ \rho u(v - v_{c.v.}) \\ \rho v(v - v_{c.v.}) + p \\ \rho w(v - v_{c.v.}) \\ (\rho E + p)(v - v_{c.v.}) + v_{c.v.}p \end{bmatrix} \quad (3-13)$$

$$H = \begin{bmatrix} \rho(w - w_{c.v.}) \\ \rho u(w - w_{c.v.}) \\ \rho v(w - w_{c.v.}) \\ \rho w(w - w_{c.v.}) + p \\ (\rho E + p)(w - w_{c.v.}) + w_{c.v.}p \end{bmatrix} \quad (3-14)$$

The diffusive flux vector \vec{Q} can be defined as follows:

$$\vec{Q} = \frac{M_\infty}{Re_L} (Q_x \vec{i} + Q_y \vec{j} + Q_z \vec{k}) \quad (3-15)$$

Here;

$$Q_x = \begin{bmatrix} 0 \\ \tau_{xx} \\ \tau_{xy} \\ \tau_{xz} \\ \tau_{xx}u + \tau_{xy}v + \tau_{xz}w - \dot{q}_x \end{bmatrix} \quad (3-16)$$

$$Q_y = \begin{bmatrix} 0 \\ \tau_{yx} \\ \tau_{yy} \\ \tau_{yz} \\ \tau_{yx}u + \tau_{yy}v + \tau_{yz}w - \dot{q}_y \end{bmatrix} \quad (3-17)$$

$$Q_z = \begin{bmatrix} 0 \\ \tau_{zx} \\ \tau_{zy} \\ \tau_{zz} \\ \tau_{zx}u + \tau_{zy}v + \tau_{zz}w - \dot{q}_z \end{bmatrix} \quad (3-18)$$

The viscous shear stress tensors are given below.

$$\tau_{xx} = 2(\mu + \mu_t) \frac{\partial u}{\partial x} - \frac{2}{3}(\mu + \mu_t) \left(\frac{\partial u}{\partial x} + \frac{\partial v}{\partial y} + \frac{\partial w}{\partial z} \right) \quad (3-19)$$

$$\tau_{yy} = 2(\mu + \mu_t) \frac{\partial v}{\partial y} - \frac{2}{3}(\mu + \mu_t) \left(\frac{\partial u}{\partial x} + \frac{\partial v}{\partial y} + \frac{\partial w}{\partial z} \right) \quad (3-20)$$

$$\tau_{zz} = 2(\mu + \mu_t) \frac{\partial w}{\partial z} - \frac{2}{3}(\mu + \mu_t) \left(\frac{\partial u}{\partial x} + \frac{\partial v}{\partial y} + \frac{\partial w}{\partial z} \right) \quad (3-21)$$

$$\tau_{xy} = \tau_{yx} = (\mu + \mu_t) \left(\frac{\partial u}{\partial y} + \frac{\partial v}{\partial x} \right) \quad (3-22)$$

$$\tau_{xz} = \tau_{zx} = (\mu + \mu_t) \left(\frac{\partial u}{\partial z} + \frac{\partial w}{\partial x} \right) \quad (3-23)$$

$$\tau_{yz} = \tau_{zy} = (\mu + \mu_t) \left(\frac{\partial v}{\partial z} + \frac{\partial w}{\partial y} \right) \quad (3-24)$$

The heat conductions are given below.

$$\dot{q}_x = -\frac{1}{(\gamma - 1)} \left(\frac{\mu}{Pr} + \frac{\mu_t}{Pr_t} \right) \frac{\partial T}{\partial x} \quad (3-25)$$

$$\dot{q}_y = -\frac{1}{(\gamma - 1)} \left(\frac{\mu}{Pr} + \frac{\mu_t}{Pr_t} \right) \frac{\partial T}{\partial y} \quad (3-26)$$

$$\dot{q}_z = -\frac{1}{(\gamma - 1)} \left(\frac{\mu}{Pr} + \frac{\mu_t}{Pr_t} \right) \frac{\partial T}{\partial z} \quad (3-27)$$

Finally, the pressure is defined as perfect gas.

$$P = (\gamma - 1) \left[\rho E - \frac{1}{2} \rho (u^2 + v^2 + w^2) \right] \quad (3-28)$$

3.2.2 Non-Dimensionalization of Governing Equations

The equations are non-dimensionalized with free stream speed of sound (a_∞), density (ρ_∞), temperature (T_∞), viscosity (μ_∞) and reference length (L_{ref}). The non-dimensional forms of the terms are given in Table 3.1.

Table 3.1 Non-dimensional form of variables

$u^* = \frac{u}{a_\infty}$	$a^* = \frac{a}{a_\infty}$	$\rho^* = \frac{\rho}{\rho_\infty}$	$\mu_t^* = \frac{\mu_t}{\mu_\infty}$
$v^* = \frac{v}{a_\infty}$	$P^* = \frac{P}{\rho_\infty a_\infty^2}$	$E^* = \frac{E}{a_\infty^2}$	$x^*, y^*, z^* = \frac{x, y, z}{L_{ref}}$
$w^* = \frac{w}{a_\infty}$	$T^* = \frac{T}{T_\infty}$	$\mu^* = \frac{\mu}{\mu_\infty}$	$t^* = \frac{t}{L_{ref}/a_\infty}$

3.3 Numerical Tools and Discretization

Equations of fluid motions are highly nonlinear and exact solutions of these governing equations are not possible for numerical simulations of missiles. Numerical modeling approach is used for the problems like that of missiles. Exact solution of the fluid motions exists only for special cases [29]. In this study, as a numerical solver, commercial CFD software FLUENT® (version 12.0.16) is used. FLUENT® solves the governing equations by using an unstructured finite volume based approach [30]. The solid models and solutions domain are generated with commercial tools GAMBIT® (version 2.4.6) and TGRID® (version 5.0.6). These grid generation programs have different capabilities. According to the capabilities, the surface grids of the test case models are generated with GAMBIT®, boundary layer grids are generated with TGRID® and finally volume grid is generated with GAMBIT®. Surface grids of the models are consisted of triangular elements. Boundary layer grids are of type wedge elements and volume grids are of type tetrahedral elements.

For all type of problems, FLUENT® solves the discretized form of conservation equations for mass and momentum. Additional energy equation is solved for the problems like heat transfer or compressibility or additional transport equations are solved for the turbulent flow problems.

In FLUENT®, two different solver type, pressure-based and density based, can be used. Pressure-based solver is mainly used for low speed incompressible flows whereas density based solver is mainly used for high speed compressible flow

problems. However, these two methods have been modified to solve and operate for a wide range of flow regimes beyond their original intents.

In both approaches, the velocity field is calculated from momentum equations. In density-based method, the density field is calculated from continuity equation and the pressure field is calculated from the equation of state. In pressure-based approaches, the pressure field is calculated from pressure or pressure correction equation which is obtained by modifying the equations of momentum and continuity.

In both pressure-based and density-based method, FLUENT® solves the integral form of governing equations and if necessary additional equations such as energy and transfer by using the finite volume technique. In this technique:

- The solution domain is divided into discrete finite control volumes by using computational grids.
- The governing equations are integrated on individual finite control volumes to build up algebraic equations for dependent variables such as pressure, temperature and velocities.
- The discretized equations are linearized and the resultant linear equations system is solved to update the dependent variables.

Pressure-based and density based methods use a similar discretization technique, however, they use different approaches to linearize and solve the discretized equations.

In pressure-based solver, conservation equations are solved sequentially whereas in density-based solver these equations are coupled and thus solved simultaneously. These result in higher instantaneous computational memory demand. The algorithm of density-based solver is given in Figure 3.1.

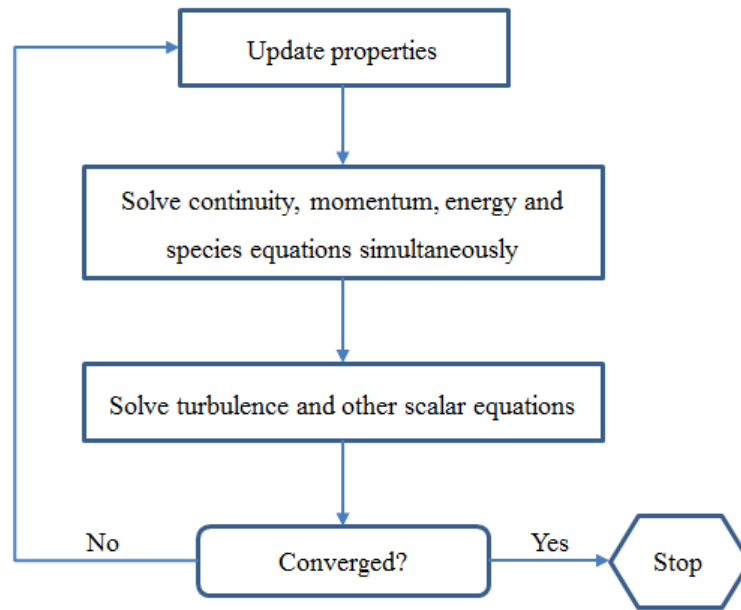


Figure 3.1 Density-based algorithm [30]

As it is seen in Figure 3.1, continuity, momentum, energy and species equations are solved simultaneously. Then, the turbulence and other scalar equations are solved. This procedure is done until the convergence achieved. In this study, steady and unsteady simulations are performed. Therefore, different convergence criteria are defined for steady and unsteady simulations. For the steady simulations, the solution is assumed converged when the residuals drop down to the value of 0.0001 and the change in residuals stop. The unsteady simulations are assumed converged when the last period of the motion repeats the one before. Before starting unsteady simulations, steady simulations are conducted to obtain better initial conditions to the unsteady simulations. With this method, faster convergence is achieved. In this study, the convergence is generally achieved with 3-4 periods.

CHAPTER 4

TEST CASE MODELS AND CFD MODELING

Three different test case models are used for the validation of numerical methods. First one, NACA 0012 airfoil is used to validate the dynamic motion simulation in 2D. Second one, Basic Finner (BF), is a simple four-finned model and other one is the modified form of this model namely; Modified Basic Finner (MBF). In this chapter, geometric specification of the test case models, computational domains generated for pitching and rolling motion simulations, and boundary conditions are explained in details.

4.1 Geometric Specifications and Solid Models

Geometric specification of test case models and solid models generated for CFD simulations are presented in the following sub sections.

4.1.1 Test Case Model – 1

Before starting the 3D simulations of dynamic pitching and rolling motions, NACA0012 airfoil is used for the validation of numerical method in 2D [31]. Simulation results are validated with the experimental data [32] of forced-oscillation pitching motion which is given in Table 4.1.

Table 4.1 Experimental conditions of pitching motion for NACA0012 airfoil [32]

Case	Mach Number	$\alpha_m(^{\circ})$	$\alpha_0(^{\circ})$	$f(\text{Hz})$	k	$\text{Re} \times 10^{-6}$
Case-1	0.6	2.89	2.41	50.32	0.0808	4.8
Case-2	0.6	3.16	4.59	50.32	0.0811	4.8
Case-3	0.6	4.86	2.44	50.32	0.0810	4.8
Case-4	0.755	0.016	2.51	62.50	0.0814	5.5

4.1.2 Test Case Model – 2

BF is a simple four-finned model with no protuberances. It has 2.836 calibers conic nose and has L/D ratio of 10. This model has experimental data for three different center of rotation in other words center of gravity locations [6]-[8]. The center of gravity locations are 5, 5.5 and 6.1 diameter behind the nose. Geometric specification of the model is given in Figure 4.1 and the solid model generated for CFD simulations is given in Figure 4.2.

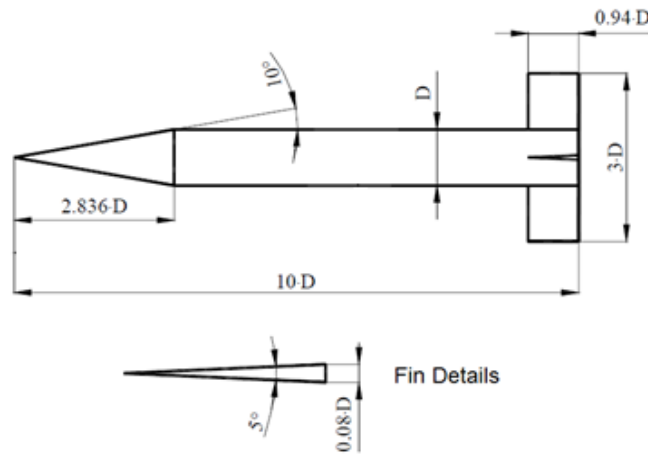


Figure 4.1 Dimensions of BF test model [16]



Figure 4.2 Solid model of BF test model

4.1.3 Test Case Model - 3

MBF model is the modified form of BF model. This model is also four-finned and has no protuberances. It has 2.5 calibers tangent ogive nose and 7.5 calibers cylindrical after body. MBF has experimental data for two different center of gravity locations. The center of gravity locations are 4.8 and 5 diameter behind the nose. Geometric specifications, photos of the model in T-38 wind tunnel test section and solid model are given in Figure 4.3, Figure 4.4 and Figure 4.5 respectively.

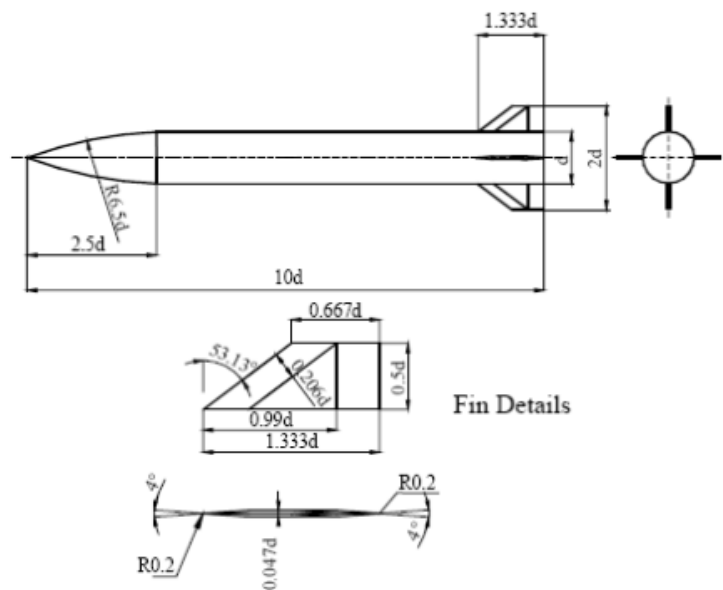


Figure 4.3 Dimensions of MBF test model [6], [7]



Figure 4.4 MBF test model in T-38 Trisonic Wind Tunnel [7]



Figure 4.5 Solid model of MBF

4.2 Grid Generation

In order to model the geometry better, unstructured grids are used. For modeling the NACA0012 airfoil, quadrilateral elements are used for boundary layers and triangular elements are used for the volume grids. On the other hand, for BF and MBF models, triangular elements are used for surfaces, wedge elements are used for boundary layers and tetrahedral elements are used for the rest of solution domain. Type of elements used for modeling the solution domains are shown in Figure 4.6

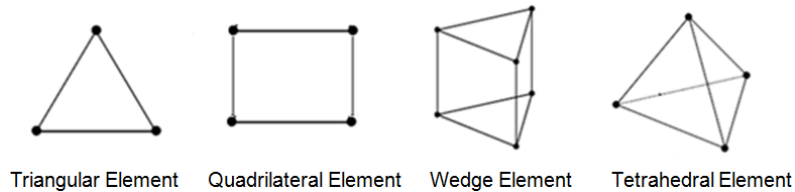


Figure 4.6 Solution domain elements [33]

Surfaces that the flow variables are expected to have bigger gradients are modeled with small size elements and the surfaces that the flow variables are expected to have smaller gradients are modeled with bigger size elements.

Boundary layer grids are composed of two parts and each has 10 prismatic layers. The first layer thickness of the first part for NACA0012 airfoil 0.00005 mm and the first 10 layers grow with a geometric ratio of 1.4. The second part has a 0.001 mm first layer thickness and grows with a last ratio of 50 %. For the BF and MBF models, the first parts have 0.001 mm first height length and grow with a geometric ratio of 1.2. The second parts have 0.006 mm first height length and grow with last ratio of 50 %. The rest of solution domain elements starting from boundary layer grow with a geometric ratio of 1.15.

Three different grids are generated for NACA0012 airfoil as a part of grid convergence study. Same grid generation strategy is applied for these three grids. Only, the number of vertices on the airfoil has been changed. Number of solution domain elements generated for NACA0012 airfoil is given in Table 4.2 and the medium grid of NACA0012 airfoil is shown in Figure 4.7.

Table 4.2 Grid convergence for NACA0012 airfoil

Grid	Triangular Elements	Quadrilateral Elements
Coarse	29,416	6,000
Medium	36,176	10,000
Fine	41,432	16,000

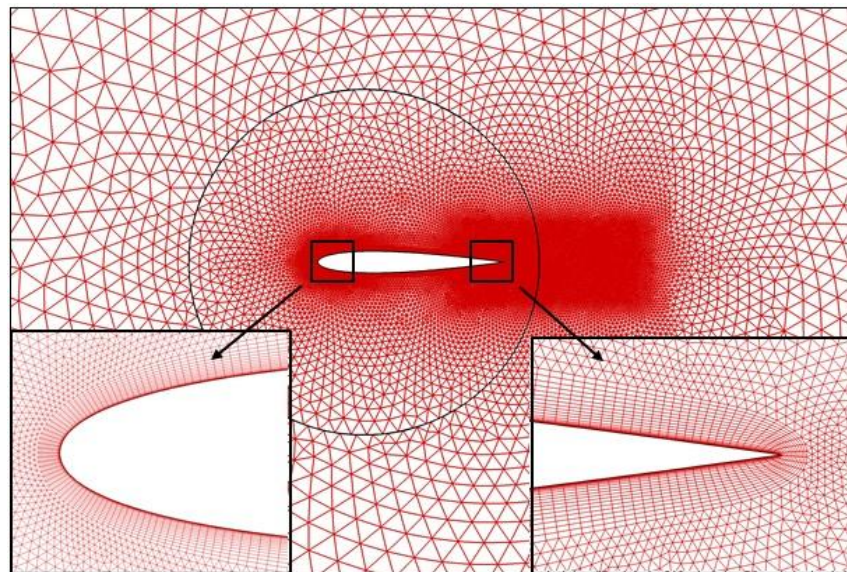


Figure 4.7 Medium grid of NACA0012 airfoil

The BF and MBF models are similar to the each other. Therefore, the grid convergence study is carried out only for MBF model. After determining the appropriate grid for MBF model, similar grids are generated for BF model. Within the grid convergence study, three different surface grids are generated for MBF model. Static aerodynamic analyses are performed with these three grids and the most suitable surface grid is selected for the dynamic motion simulations. The grids generated for rolling motion simulations are used for static aerodynamic analyses of

MBF model. Numbers of solution domain elements generated for rolling motions simulations are given Table 4.3.

Table 4.3 Grid convergence for MBF model

Grid	Triangular Elements	Wedge Elements	Tetrahedral Elements
Coarse	277,722	1,655,240	2,478,093
Medium	364,400	2,225,120	3,146,768
Fine	454,826	2,820,640	3,800,832

Medium grid of MBF model generated for rolling motion simulations is shown in Figure 4.8 and boundary layer grid is shown in Figure 4.9.

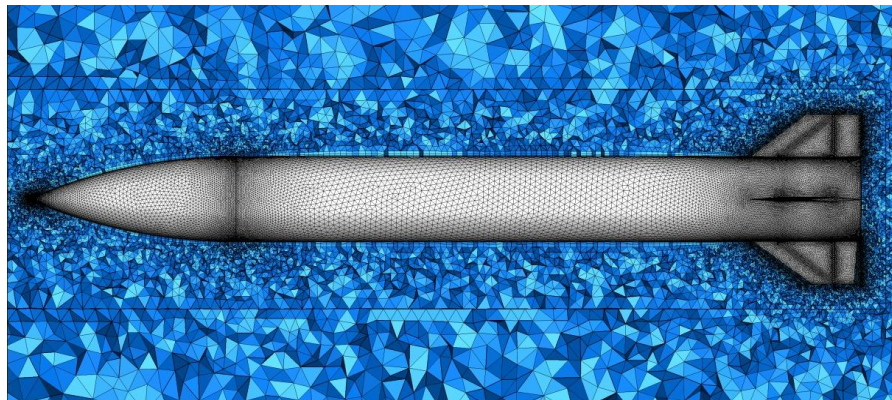


Figure 4.8 Medium volume grid of MBF model

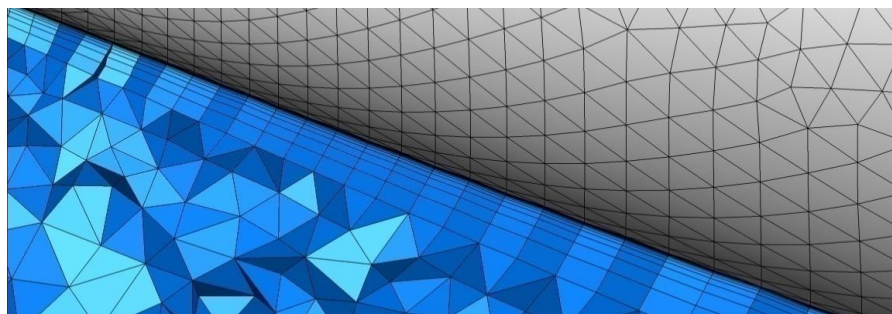


Figure 4.9 Boundary layer grid of MBF model

As a result of grid convergence study, the appropriate surface grid is determined. With this grid, pitching motion simulation grids of MBF model are generated.

Moreover, for BF model, similar surface grid is used for generating the pitching and rolling motion simulation grids.

4.3 Grid Quality Analysis

The quality of solution domain elements affects the simulation results. In order to get better results the quality of elements should be good enough. Generally, the quality of solution domain elements is determined by four basic criteria namely; clustering, smoothness, aspect ratio and skewness [34]. In addition, the boundary layer quality is another important quality parameter for the numerical simulations. In this part, the quality of the solution domain elements is examined in details.

The clustering is about the resolution of solution domain. In other words, solution domain elements should be fine enough to capture the features of the flow that is being analyzed. In order to guarantee the resolution of solution domain the grid refinement study is carried out for NACA0012 airfoil and MBF model from subsonic to supersonic flow regimes. Details of grid convergence study are given in Chapter 5.

Smoothness is the change in size from one element to the other one. In a high quality grid this change in size should be gradual. In this study, the smoothness criterion is achieved with the help of size function tools of GAMBIT® [33]. The growth rate of elements is controlled by defining the size functions for the surface and volume cells.

Another quality parameter is aspect ratio which is the ratio of the longest edge length to the shortest edge length. As expected, the maximum aspect ratio elements are occurred at boundary layer cells because of the nature of the boundary layers. The first layer thickness of the boundary layers corresponding to the y^+ value of one is too small as compared to the edge or surface element sizes. In addition to this, to capture the velocity and pressure gradients, the boundary layer cells should grow gradually. Therefore, this will result in higher aspect ratio elements. In this study, maximum aspect ratio of the elements is kept small as possible by keeping the maximum length of the edge and surface elements small as possible.

In the following parts, the most important quality parameter skewness ratio and then the boundary layer are analyzed. The details of skewness ratio and boundary layer analyses are given in the following parts.

4.3.1 Skewness Ratio

Two methods are commonly used for examining the skewness ratio of solution domain elements [34]. The first one, Equilateral Volume Based Skewness, is based on the equilateral volume and the second one, Normalized Equiangular Skewness, is based on the deviation from a normalized equilateral angle. The first method can be applied only to triangular and tetrahedral elements. The second method can be applied to all cells and faces. In this study, the second method is used to examine the solution domain elements. According to this method, the skewness ratio is defined as follows.

$$Skewness\ Ratio = \max \left[\frac{\theta_{max} - \theta_e}{180 - \theta_e}, \frac{\theta_e - \theta_{min}}{\theta_e} \right] \quad (4-1)$$

Skewness ratio parameters used in above equation are explained in Table 4.4.

Table 4.4 Skewness ratio parameters [34]

Parameter	Explanations
θ_{max}	Largest interior angle of element
θ_{min}	Smallest interior angle of element
θ_e	Interior angle of equilateral triangle or rectangle (60° or 90°)

The skewness ratio analysis of medium grids for BF and MBF models are given Figure 4.10.

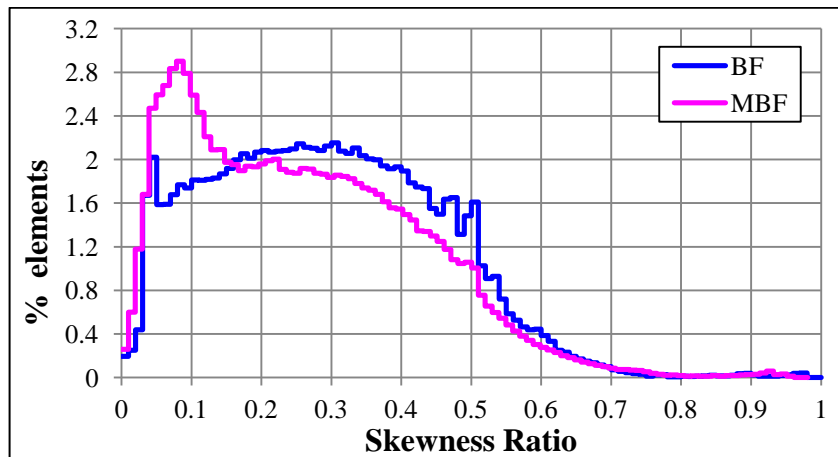


Figure 4.10 Skewness ratio analysis

Quality of the elements and the skewness ratio relation is explained in Table 4.5.

Table 4.5 Skewness ranges and cell quality [34]

Value of Skewness	Cell Quality
1	Degenerate
0.9 - <1	Bad (Sliver)
0.75 - 0.9	Poor
0.5 - 0.75	Fair
0.25 - 0.5	Good
>0 - 0.25	Excellent
0	Equilateral

As it is seen in Skewness ratio analysis in Figure 4.10, most of the solution domain elements have cell quality of good and excellent. Small amount of elements have cell quality of fair and negligible amount of the cells have cell quality of poor and bad. It can be easily said that the quality of solution domain elements is good enough for both models.

4.3.2 Boundary Layer Analysis

Turbulent boundary layer is composed of several regions and within each region different flow behaviors occur. A thin and closest region to the wall is called viscous sub layer. The outer and fully turbulent region of the boundary layer is referred to the fully turbulent region. The region between viscous sub layer and fully turbulent layer is called buffer zone [35].

Turbulent boundary layer is also categorized as inner and outer regions. The inner region involves viscous sub layer, buffer layer and a part of the fully turbulent layer. The outer region includes the remaining part of the fully turbulent layer.

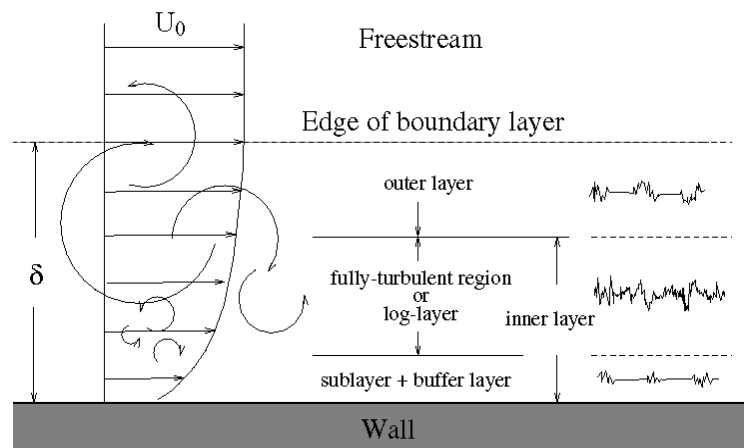


Figure 4.11 Turbulent boundary layer [36]

Turbulent boundary layer is divided into several regions by non-dimensional velocity parameter u^+ and spatial coordinate parameter y^+ . The definitions of these parameters are given in Eq. (4-2) and (4-3).

$$u^+ = \frac{u}{u_\tau} \quad (4-2)$$

$$y^+ = y \frac{u_\tau}{\nu} \quad (4-3)$$

Here, u_τ is the friction velocity and it is defined as follows:

$$u_\tau = \sqrt{\frac{\tau_w}{\rho}} \quad (4-4)$$

In Eq. (4-4), τ_w is the shear stress of the wall and ρ is the density of the fluid. According to these definitions the turbulent boundary layers are divided into several parts which are given in Table 4.6 below.

Table 4.6 y^+ values and boundary layer zones [35]

$y^+ < 2 \sim 8$	Viscous sub layer
$2 \sim 8 < y^+ < 2 \sim 50$	Buffer zone
$y^+ > \sim 50$	Fully turbulent zone
$y^+ < 100 \sim 400$	Inner region
$y^+ > 100 \sim 400$	Outer region

The change of non-dimensional velocity profile versus non-dimensional spatial coordinate over a flat plate for turbulent flow is given in Figure 4.12.

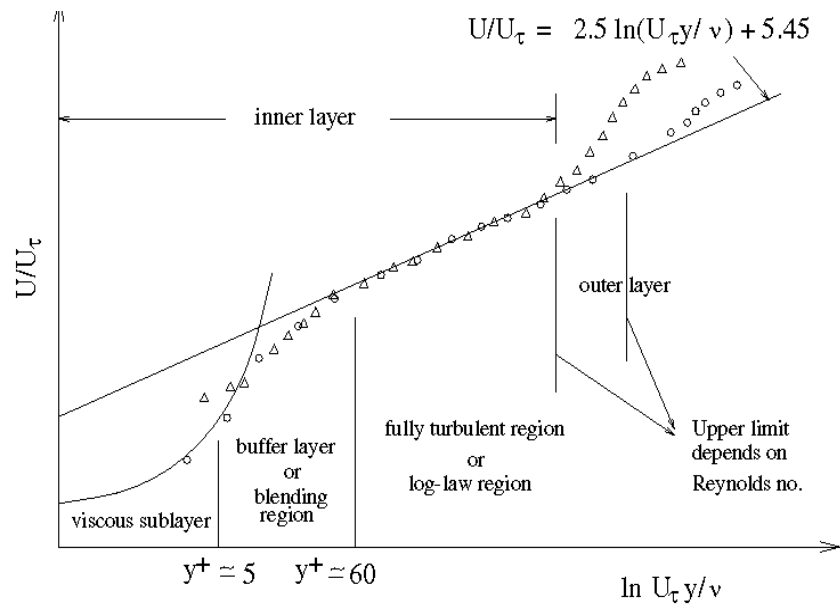


Figure 4.12 u^+ vs. y^+ over a flat plate for turbulent flow [36]

In FLUENT®, “Wall Function” and “Near-Wall Model” approaches are used for modeling the near-wall zones [30]. In “Wall Function” method, the viscous sub layer and buffer layer are not resolved with solution domain elements. Instead of resolving these layers semi-empirical equations are used. In this method, the wall functions play a bridge role between fully turbulent region and the wall. In “Near-Wall Model” method the buffer zone and viscous sub layer are resolved with solution domain elements. The turbulence models are modified to solve these viscosity affected regions. According to wall function approach, the first cell has to be located at fully turbulent region. In other words, the first cell should be located such that y^+ value is greater than about 60. According to near-wall model approach, the cells near the wall have to be finer. In this method, the first cell has to be located such that y^+ value is less than about 5. Generally, near-wall model approach is recommended when the problem has wall-bounded turbulent flows. Therefore, in this study, near-wall model method is selected and used for modeling the dynamic pitching and rolling motions.

In order to generate suitable the boundary layer grid according to the near-wall model the first height thickness of the boundary layer should be calculated accurately. In present study, to be on safe side, first height thickness of the boundary layer cells is calculated according to the y^+ value of one. However, determination of first height thickness is not possible before analysis. In literature, there exists lots of empirical formula about prediction of first height thickness according to desired y^+ values. However, they may not give exact values for all flow types and regimes. The predicted and calculated y^+ values may exhibit great differences. In this study, the first height thickness according to the desired y^+ value is calculated with the following equation [37].

$$fh = \frac{y^+}{Re \left(\sqrt{C_f/2} \right)} \quad (4-5)$$

Here, fh is the first height thickness and C_f is the skin friction coefficient. C_f is calculated with Eq. (4-6).

$$C_f = \frac{0.455}{\ln^2(0.006Re)} \quad (4-6)$$

After the steady analyses, y^+ distributions over test case models are controlled at different Mach numbers. It is seen that the y^+ values are below the desired value of one for all models throughout the whole flow regimes. As an example, y^+ distribution on NACA0012 airfoil at Mach number 0.755 and on MBF model at Mach number 1.75 are given in Figure 4.13 and Figure 4.14 respectively.

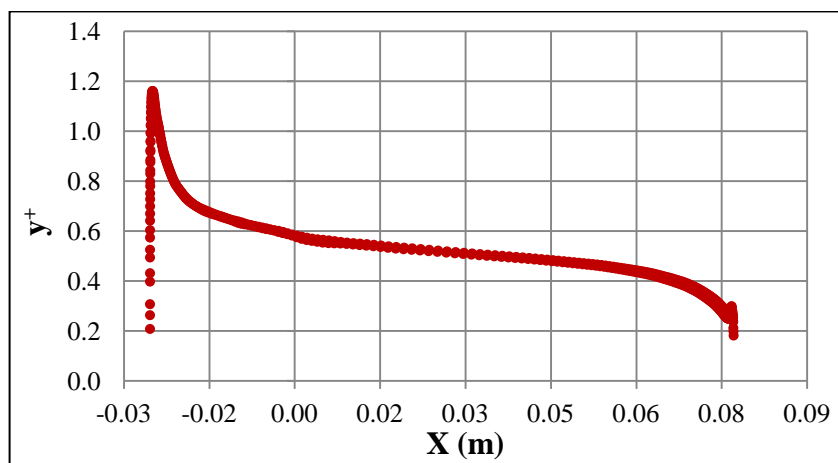


Figure 4.13 y^+ distribution on NACA0012 airfoil (Mach=0.755, $\alpha=0^\circ$)

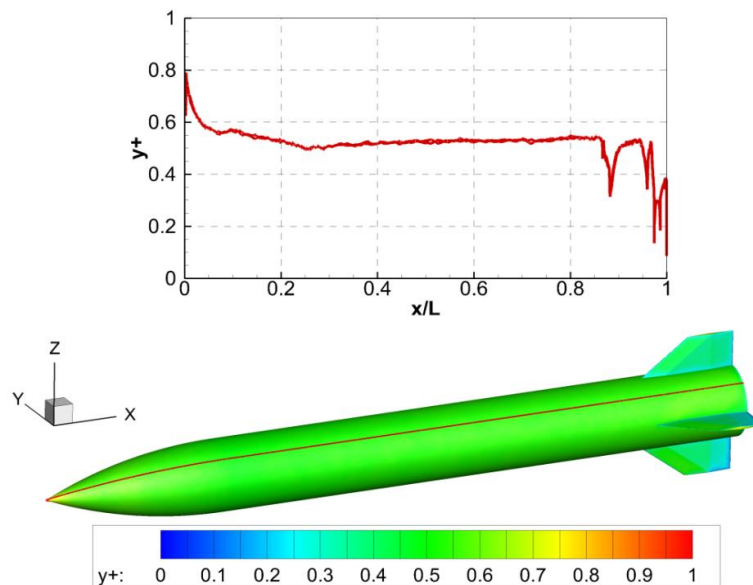


Figure 4.14 y^+ distribution on MBF model (Mach=1.75, $\alpha=0^\circ$)

4.4 Solution Domains and Boundary Conditions

Solution domain of pitching and rolling motion simulations are consisted of inner and outer domains. Inner domain, in which the dynamic motion is defined, is small circular domain for 2D simulations and cylindrical domains for 3D simulations. The outer domains are quadrilateral domain for 2D simulations and cylindrical domains for 3D simulations. The geometric specifications of inner and outer domains for 2D and 3D simulations are given in Table 4.7 and Table 4.8.

Table 4.7 Geometric specifications of solution domains for NACA0012 airfoil

Domain	Radius (m)	Width (m)	Length (m)
Inner	0.1016	N/A	N/A
Outer	N/A	3.4544	4.7752

The schematic view of solution domains and boundary conditions for NACA0012 airfoil is given in Figure 4.15.

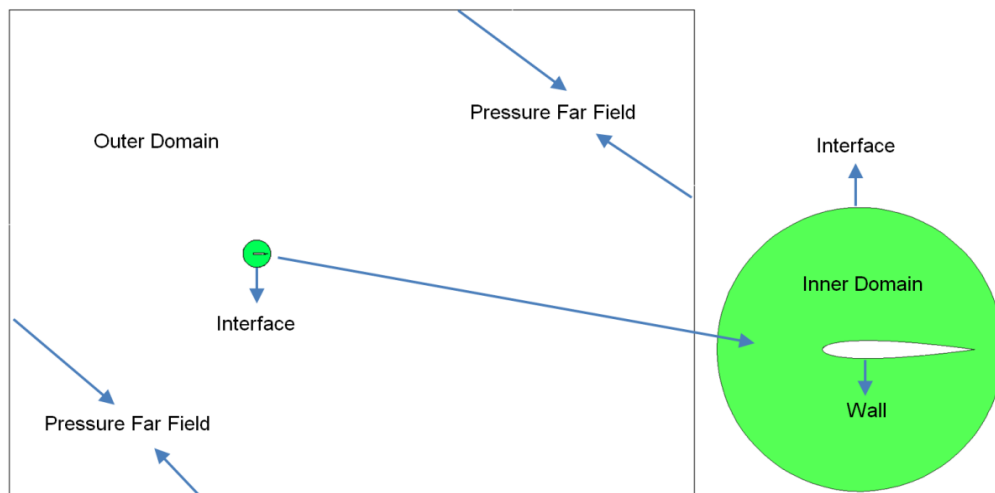


Figure 4.15 Solution domain and boundary conditions of NACA0012 for pitching motion simulations

Table 4.8 Geometric specifications of solution domains for BF and MBF models

Pitching Motion			Rolling Motion		
Domain	Diameter (m)	Length (m)	Domain	Diameter (m)	Length (m)
Inner	0.4	0.12	Inner	0.15	0.4
Outer	10.2	19.2	Outer	10.2	19.2

The schematic view of solution domains and boundary conditions for MBF model are given in Figure 4.16 and Figure 4.17.

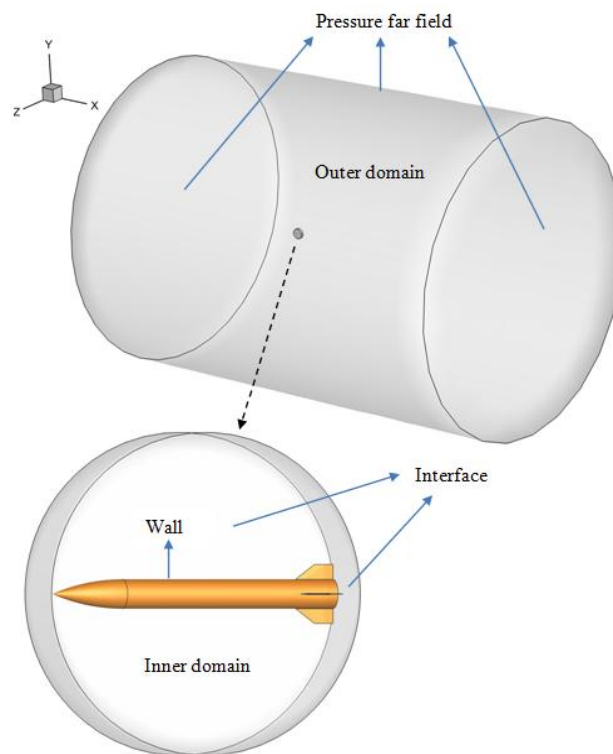


Figure 4.16 Solution domain and boundary conditions of MBF model for pitching motion simulations

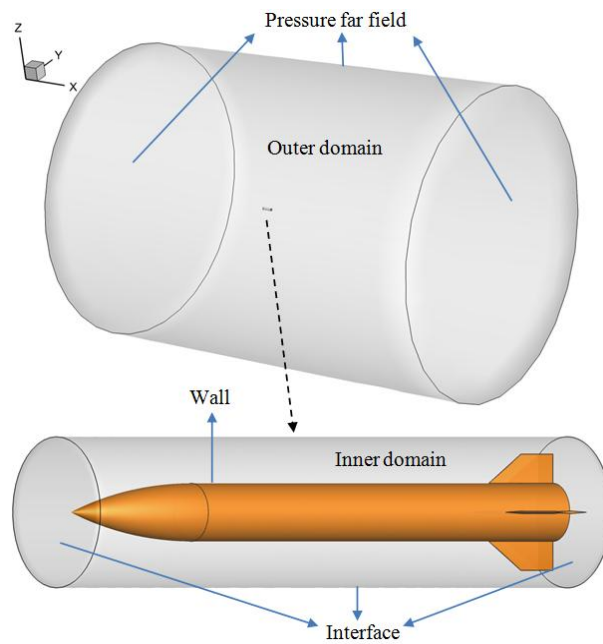


Figure 4.17 Solution domain and boundary conditions of MBF model for rolling motion simulations

As it is seen in Figure 4.15, Figure 4.16 and Figure 4.17, the edge of the NACA0012 airfoil and the surfaces of BF and MBF models are defined as wall boundary conditions. The outer edges of the NACA0012 solution domain and the outer surfaces of BF and MBF models' solution domains are defined as pressure far field (characteristic) boundary conditions. The edges and/or faces between the inner and outer domains are defined as interface boundary conditions. Detailed information about the characteristics of boundary conditions is explained in the following parts.

4.4.1 Wall Boundary Condition

Wall boundary conditions are used for defining the boundaries of solid and fluid regions. For the problems involving viscous flows, no-slip boundary conditions are enforced to the walls [38]. This condition is carried out with the help of ghost cells. In this problem, the surfaces of the test case models are defined as no-slip wall boundary conditions.

4.4.2 Pressure Far Field (Characteristic) Boundary Condition

In external flow problems, pressure far field boundary conditions should be defined on surfaces which are far away from the effects of the model. In this boundary condition, free stream velocities are defined with free stream Mach numbers, static pressures and static temperatures. This boundary condition is non-reflecting and it is based on Riemann invariants (characteristic variables) for 1D flow normal to the boundaries [38]. Corresponding to incoming and outgoing waves, two Riemann invariants exist for subsonic flow problems which are:

$$R_{\infty} = v_{n_{\infty}} - \frac{2c_{\infty}}{\gamma - 1} \quad (4-7)$$

$$R_i = v_{n_i} + \frac{2c_i}{\gamma - 1} \quad (4-8)$$

Here, the subscript “ ∞ ” refers to the boundary conditions (conditions at infinity) and the subscript “ i ” refers to the conditions of the cell adjacent to the boundary. The variable v_n represents the magnitude of the velocity normal to the boundary, γ represents the specific heat ratio and c represents the local speed of sound. By adding and subtracting the Eq. (4-7) and (4-8) the following equations are obtained.

$$v_n = \frac{1}{2}(R_i + R_{\infty}) \quad (4-9)$$

$$c = \frac{\gamma - 1}{4}(R_i - R_{\infty}) \quad (4-10)$$

In Eq. (4-9) and (4-10) v_n is the normal velocity applied on the boundary and c is the speed of sound applied on boundary. The entropy and tangential velocity components are taken as free stream values at an inflow faces on the other hand these are extrapolated from the interior cells at an outflow faces. Density, velocity, temperature and pressure values at the boundary cells can be calculated by using the v_n , c , entropy and the tangential velocity values.

4.4.3 Interface Boundary Condition

Two or more domains (cell zones) are used for modeling the moving mesh problems and each cell zone has its own surfaces where it meets with opposing cell zones. These adjacent surfaces of cell zones are associated with the opposing one to form an interface boundary condition. Along the mesh interface boundary, each cell zone moves relative to one another. The solution variables of the cell zones are interpolated to each other along this boundary whether it has conformal or non-conformal meshes [30].

CHAPTER 5

VALIDATION STUDIES

In this chapter, details of validation studies are presented. Firstly, the numerical method of dynamic motion simulation is validated by using a 2D test case model NACA0012 airfoil. After validating the numerical method, grid convergence study are conducted with MBF model and turbulence model selection studies are carried out with BF and MBF models. Then, parametric studies are performed with these models for both dynamic pitching and rolling motions. Finally, the computed results of pitch and roll damping coefficients are compared with the experimental data obtained from different wind tunnels and free flight tests.

5.1 Validation of Numerical Method

The sinusoidal pitching motion can be shown as follows.

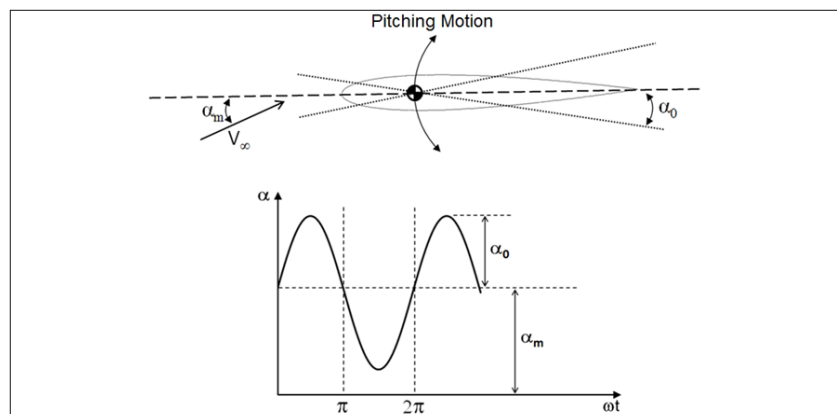


Figure 5.1 Schematic view of pitching motion of NACA0012 airfoil

Here, α_m is the mean angle of attack in which the airfoil oscillates around this point, α_0 is the amplitude of oscillation angle of attack. These definitions can be formulated as follows.

$$\alpha(t) = \alpha_m + \alpha_0 \sin(2\pi ft) \quad (5-1)$$

According to the experimental conditions, sinusoidal pitching rates are given to the airfoil and these pitching rates can be obtained by taking the time derivative of angle of attack which is given in Eq. (5-1).

$$q(t) = \dot{\alpha}(t) = \alpha_0 2\pi f \cos(2\pi ft) \quad (5-2)$$

The rotation point of pitching motion is at the quarter chord from the leading edge. The change of forced-oscillation pitching rates given to the airfoil according to this center of rotation for all cases is shown in Figure 5.2.

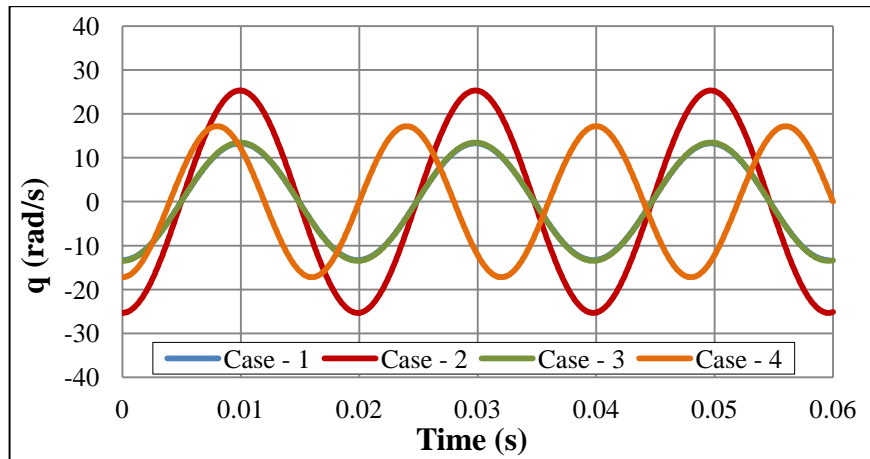


Figure 5.2 Sinusoidal pitching rates given to the NACA0012 airfoil

Pitching rate of Case-1 and Case-3 are very close to the each other, this is why the pitching rate of Case-1 is not seen in Figure 5.2. As mentioned in Chapter 4, three different grids are generated within the grid convergence study. The dynamic pitching motion simulations are performed with these grids by using Spalart-

Allmaras turbulence model for all cases. The results of the simulations conducted with these grids for Case-4 are given in Figure 5.3.

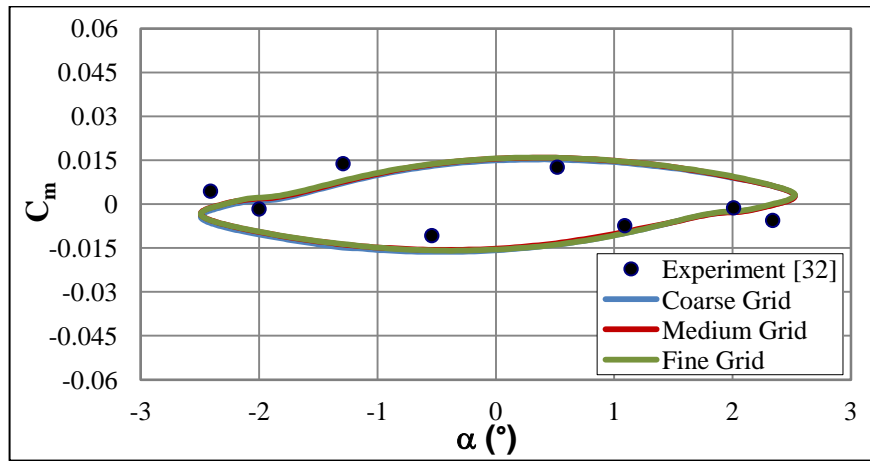


Figure 5.3 Pitching moment coefficient vs. angle of attack for different grids, Case-4

As it is seen in Figure 5.3, the results of all grids are exactly the same. Therefore, it can be said that the results are independent of grids and any of these three grids can be selected to use in dynamic motion simulations. However, by taking into account the computational time, medium grid is selected to use in dynamic motion simulations. After selecting the appropriate grid, turbulence model selection studies are carried out. Four different turbulence models namely; Spalart-Allmaras, $k-\epsilon$, $k-\omega$ and Reynolds Stress Model (RSM) are tried on all cases because turbulence models may show differences for different Mach numbers and angle of attacks. The results of simulations performed with different turbulence models for Case-4 are given as an example in Figure 5.4.

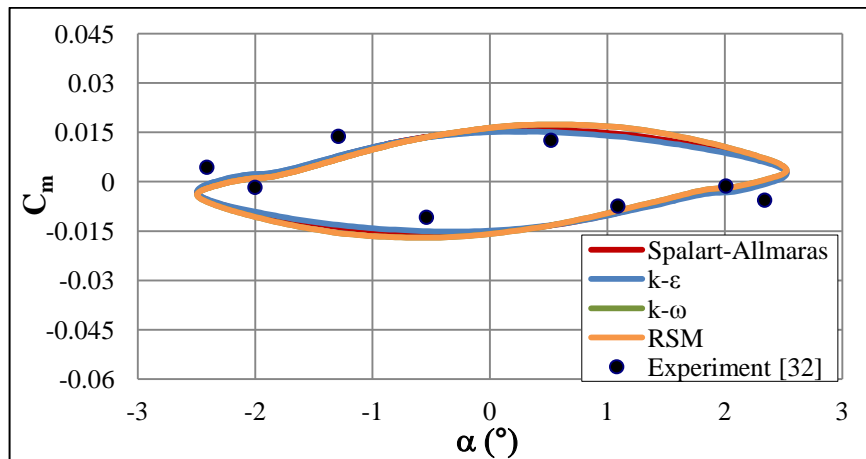


Figure 5.4 Pitching moment coefficient vs. angle of attack for different turbulence models, Case-4

As it is easily seen from Figure 5.4, the results of Spalart-Allmaras, $k-\epsilon$ and $k-\omega$ turbulence model simulations are almost same. The results of RSM turbulence model simulations only show small differences as compared to the other models. The results of Case-1, Case-2 and Case-3 are also consistent with the results of Case-4. By taking into account the simplicity and computational time, one equation turbulence model, Spalart-Allmaras is chosen and used in the dynamic motion simulations. After selecting the appropriate turbulence model, dynamic motion simulations are conducted and the computed results are compared with experimental which are given in Figure 5.5, Figure 5.6, Figure 5.7 and Figure 5.8.

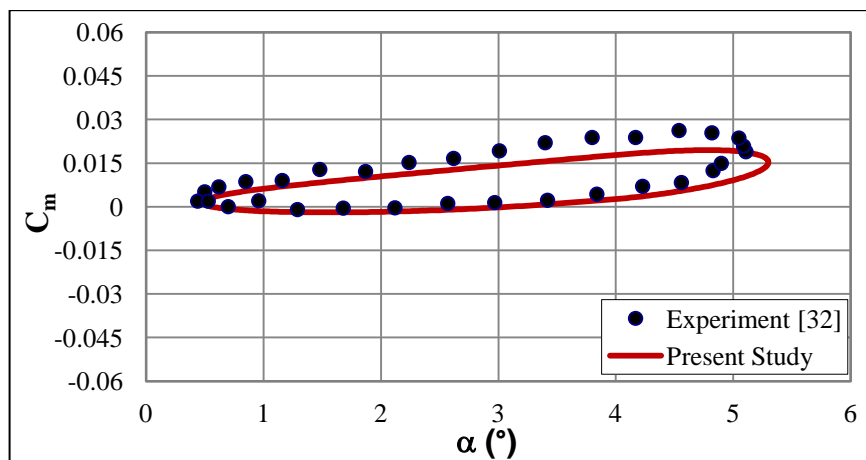


Figure 5.5 Pitching moment coefficient vs. angle of attack, Case-1

As it is seen in Figure 5.5, the numerical results of the half period are very close to experimental data. However, the numerical results of remaining half period have small differences with experimental results. These small differences may be resulted from the errors in experimental data or the lack of capability of CFD modeling. However, as it will be seen in the following figures the numerical results are very close to the experimental data for the same Mach number and similar angle of attacks. Therefore, the differences between the numerical and experimental results are most probably resulted from the errors in experimental results.

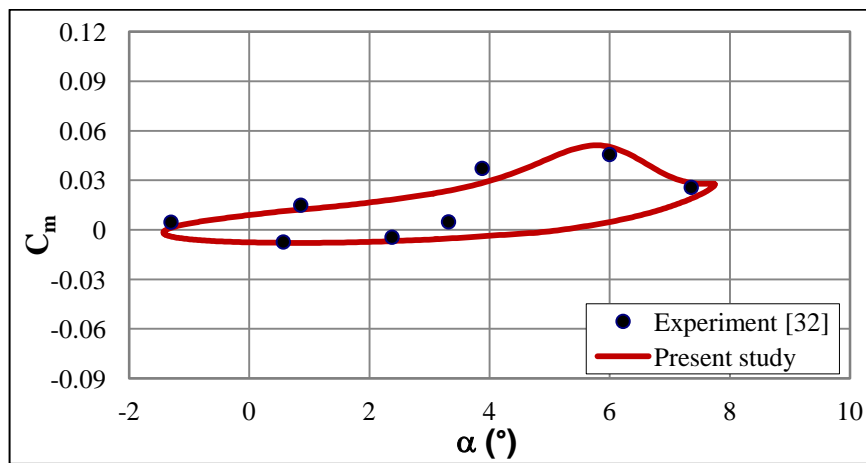


Figure 5.6 Pitching moment coefficient vs. angle of attack, Case-2

In this case, despite having a greater range of angle of attack than Case-1, the numerical results are nearly the same as experimental data. Therefore, it can be easily said that the CFD modeling has the capability of capturing the features of flow for this kind of problems.

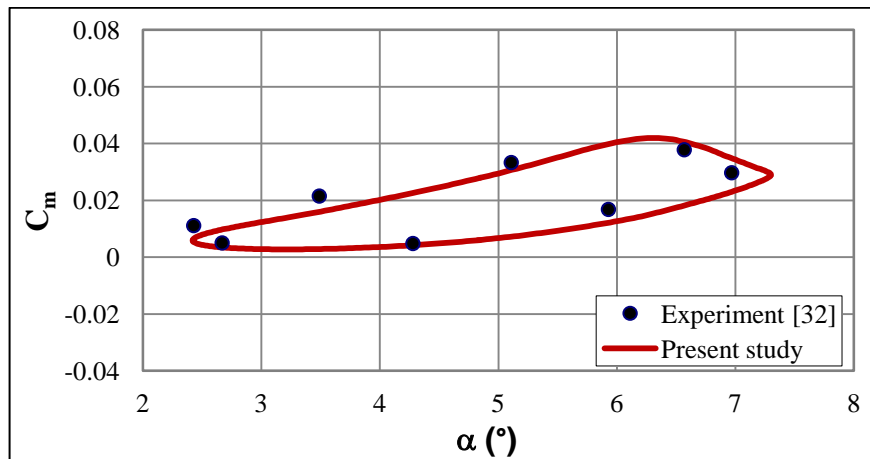


Figure 5.7 Pitching moment coefficient vs. angle of attack, Case-3

The numerical results change of pitching moment coefficient with angle of attack for the whole period for Case-3 is also consistent with the experimental data.

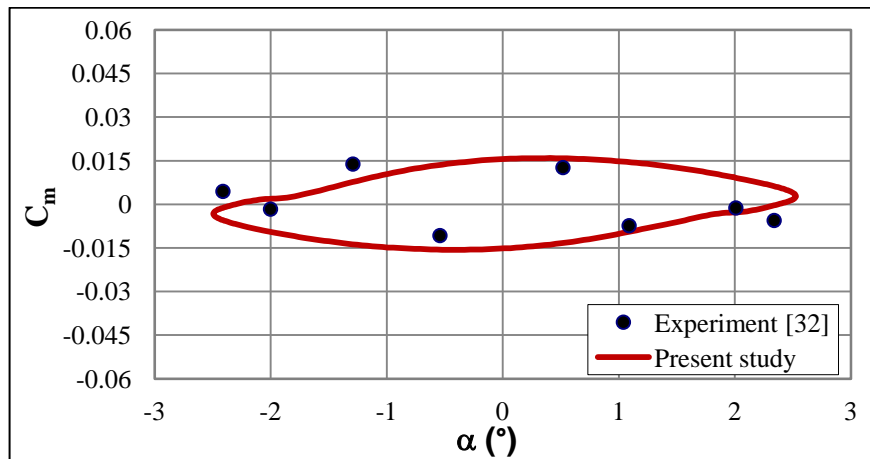


Figure 5.8 Pitching moment coefficient vs. angle of attack, Case-4

As it is observed in above figure, numerical and experimental results of Case-4 are also in good agreement with each other.

It is shown in Figure 5.5, Figure 5.6, Figure 5.7 and Figure 5.8 that the numerical and experimental results show good agreement. It can be easily concluded with this comparisons that the numerical method used for dynamic motion simulations is validated. However, in addition to the comparisons of numerical and experimental results, flow field analyses are carried out to complete the validation studies. For this

purpose, the pressure and velocity distributions at specified time steps for all cases are examined in details. Despite having different periods, to be consistent with each other, 0.06 seconds of the simulations results are presented for all cases. Moreover, the pressure and velocity distribution of same specified time steps are used for all cases.

Time history of pitching moment coefficient and expected angle of attack due to the forced pitching rate for Case-1 is given in Figure 5.9.

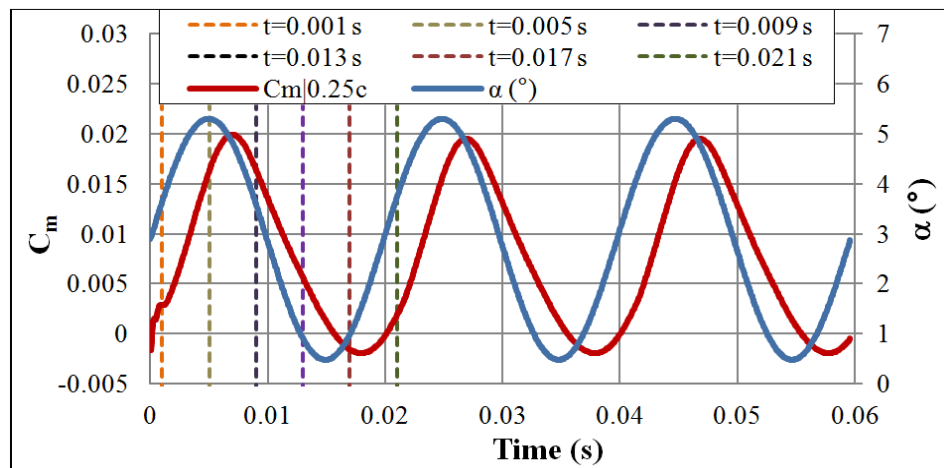


Figure 5.9 Change of pitching moment coefficient and angle of attack with time for Case-1

The oscillation angle of attack range for this case is 0.48 to 5.3 degree. The computed minimum and maximum angle of attacks has to be occurred at 0.00495 and 0.0149 second. Pressure and velocity distribution at time steps shown in Figure 5.9 are given in Figure 5.10 and Figure 5.11.

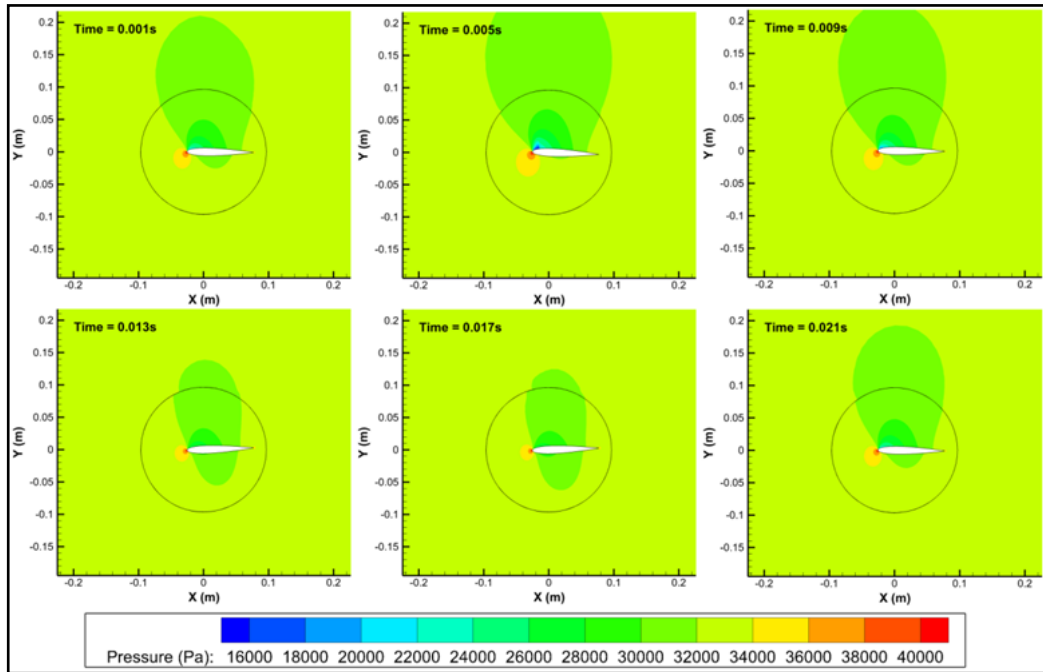


Figure 5.10 Pressure distribution at different time steps, Case-1

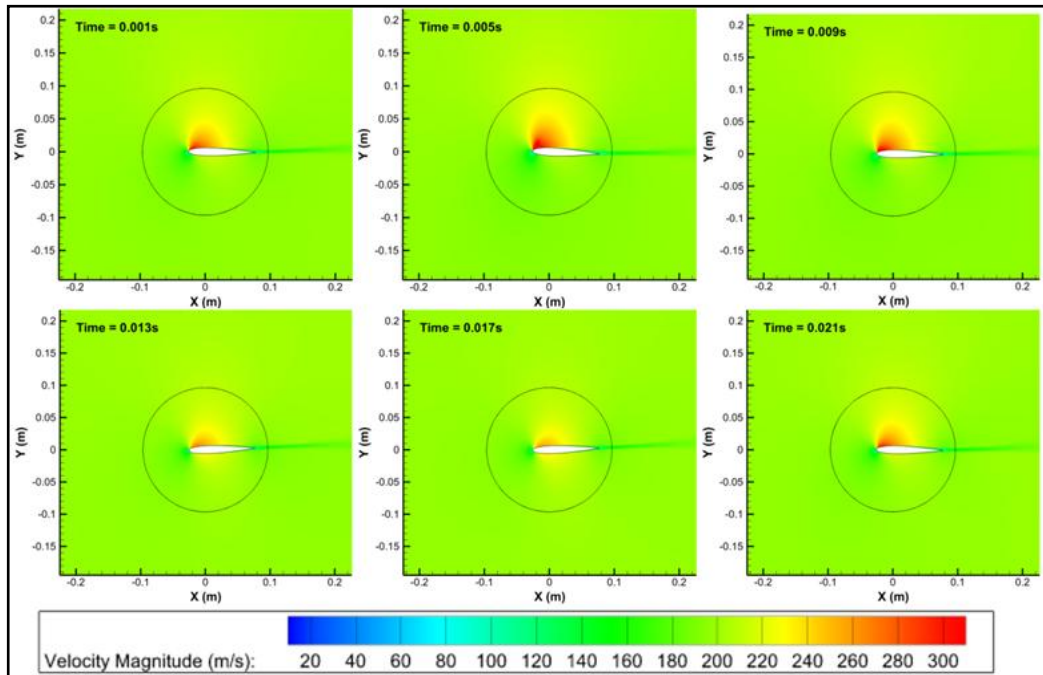


Figure 5.11 Velocity distribution at different time steps, Case-1

For Case-1, the change of angle of attack seen in pressure and velocity distributions is matched with the change of angle of attack given in Figure 5.9. In other words, the pressure and velocity distribution for Case-1 is totally consistent with the computed

angle of attacks shown in Figure 5.9. Change of pitching moment coefficient with time and change of angle of attack due to the forced pitching rate for Case-2 is given in Figure 5.12. Pressure and velocity distribution at different time steps specified in above figure are given in Figure 5.13 and Figure 5.14.

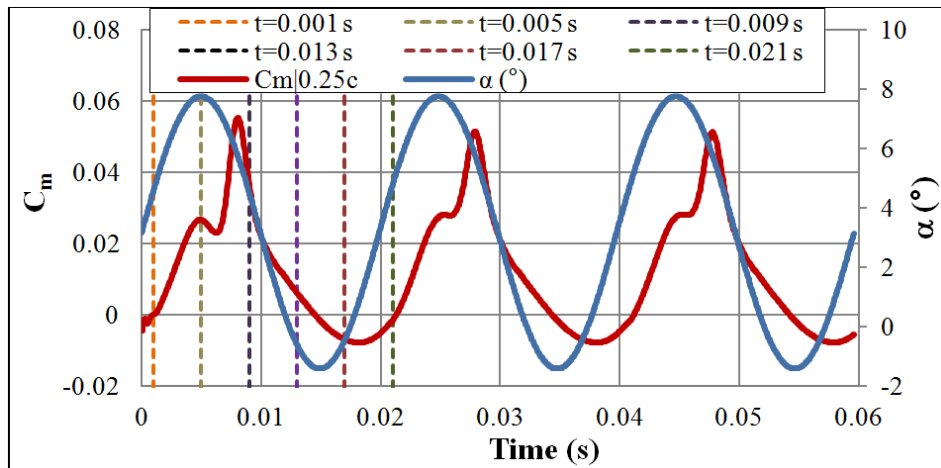


Figure 5.12 Change of pitching moment coefficient and angle of attack with time for Case-2

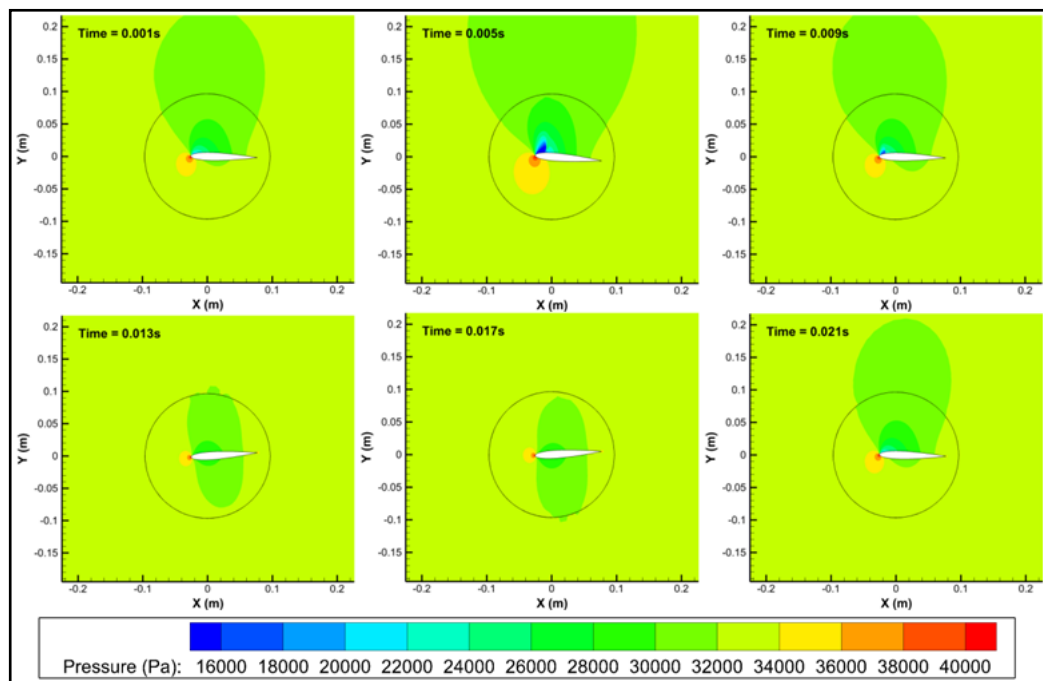


Figure 5.13 Pressure distribution at different time steps, Case-2

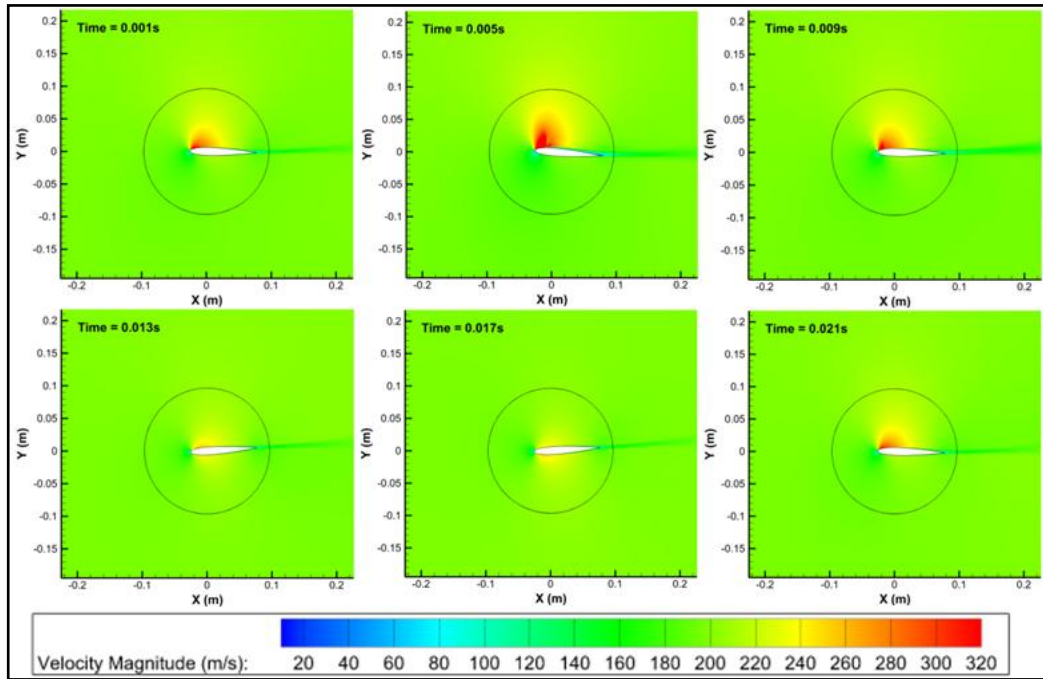


Figure 5.14 Velocity distribution at different time steps, Case-2

For Case-2, the maximum angle of attack is expected to occur at about 0.005 seconds. The minimum angle of attack and pitching moment are expected to occur at about 0.017 second. These expected values are exactly matched with the pressure and velocity distributions given in Figure 5.13 and Figure 5.14 respectively. Moreover, the pressure and velocity distributions of other time steps are also agree with expected values.

Time history of pitching moment coefficient and the computed angle of attack for Case-3 is given in Figure 5.15.

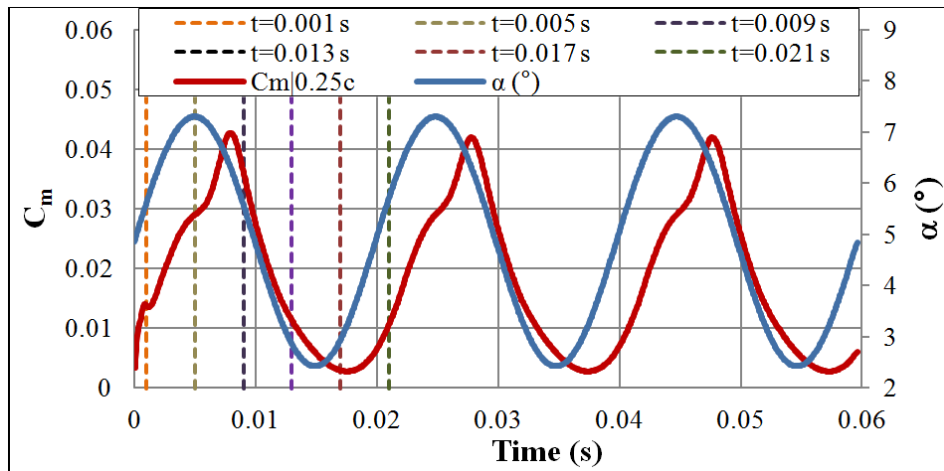


Figure 5.15 Change of pitching moment coefficient and angle of attack with time for Case-3

The oscillation angle of attack range for this case is between 2.42 and 7.3 degree angle of attacks. The maximum exposed angle of attack is expected to occur at 0.00495 second. Moreover, angle of attack of 2.85 degree has to be occurred at 0.013 second. Pressure and velocity distributions at specified time steps are given in Figure 5.16 and Figure 5.17 respectively.

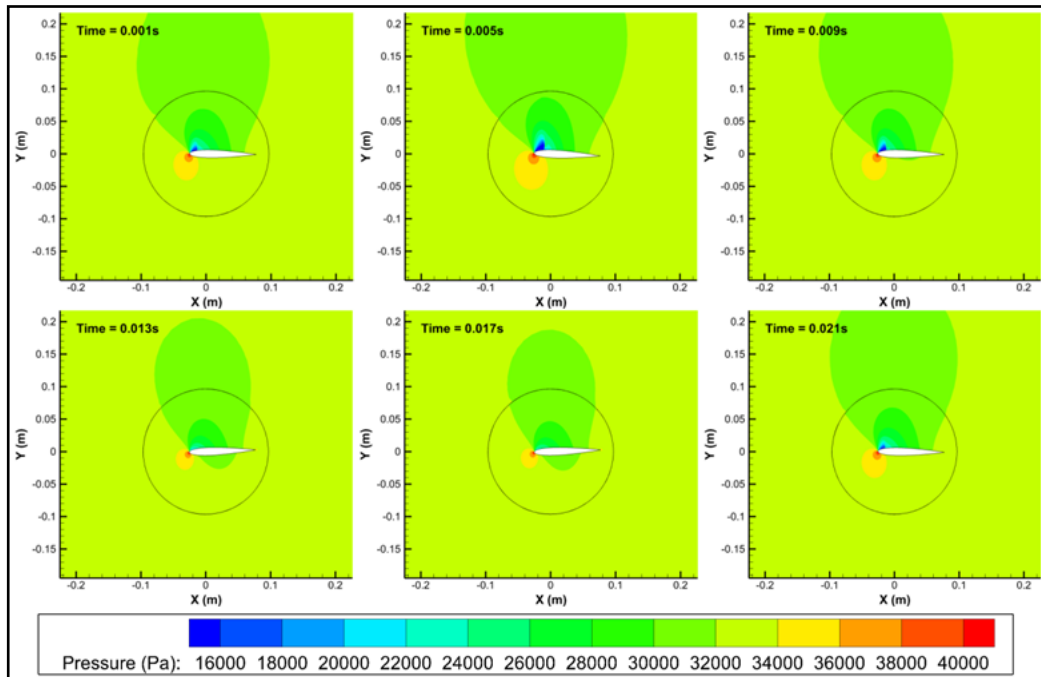


Figure 5.16 Pressure distribution at different time steps, Case-3

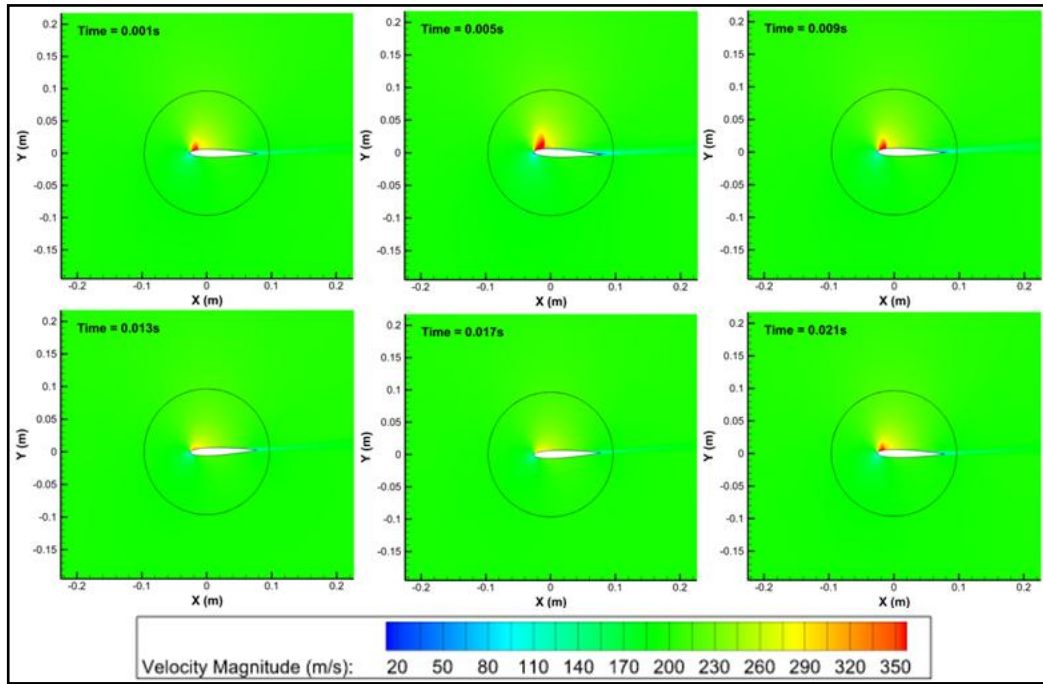


Figure 5.17 Velocity distribution at different time steps, Case-3

It is easily seen in Figure 5.16 and Figure 5.17 that the maximum angle of attack due to the forced pitching rate occurred at about 0.005 second. In addition, the angle of attack at 0.013 second is also seemed to be same as the expected value of 2.85 degree. Therefore, it can be said that the pressure and velocity distributions seen in Figure 5.16 and Figure 5.17 are totally consistent with the computed values given in Figure 5.15.

In Figure 5.18, the change of pitching moment coefficient and computed angle of attack due to the forced pitching rate with time for Case-4 are presented.

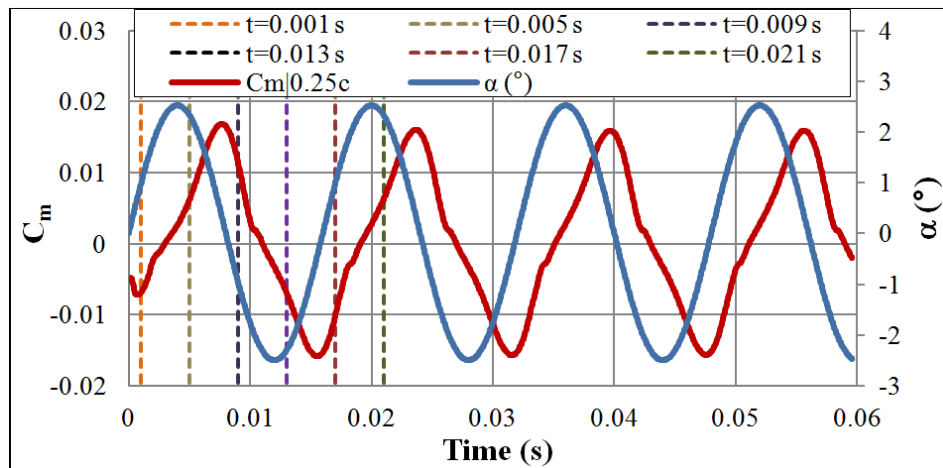


Figure 5.18 Change of pitching moment coefficient and angle of attack with time for Case-4

The oscillation angle of attack range of this case is about -2.49 to 2.53 degree. The computed maximum angle of attack should be occurred at 0.004 second and the computed minimum angle of attack should be occurred at 0.012 second. The pressure and velocity distribution of this case for different time steps are given in Figure 5.19 and Figure 5.20.

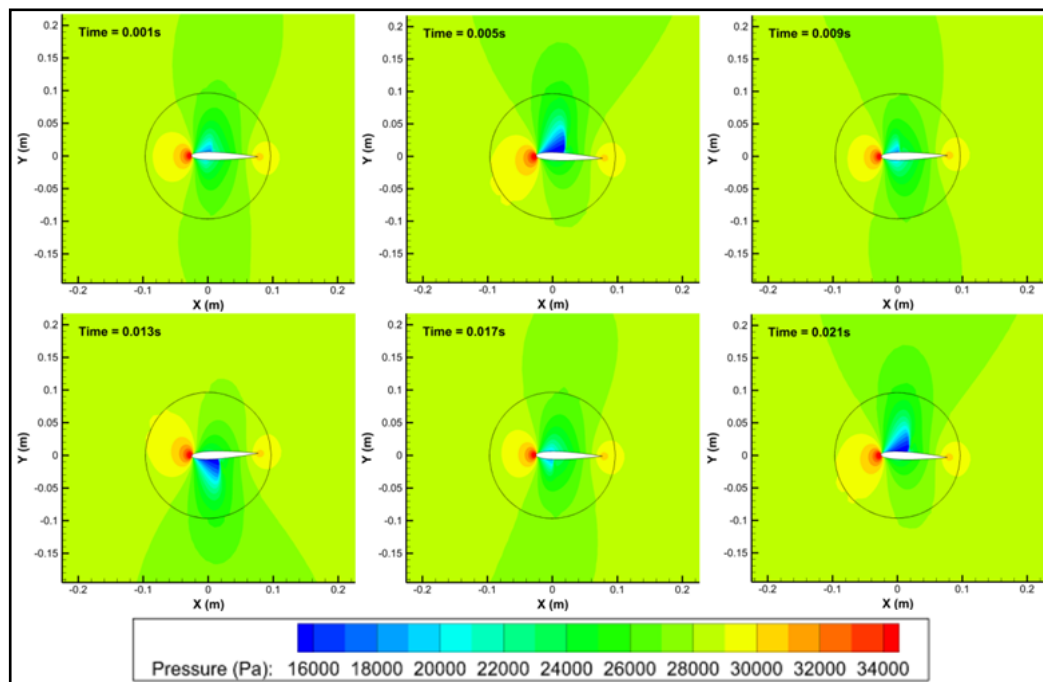


Figure 5.19 Pressure distribution at different time steps, Case-4

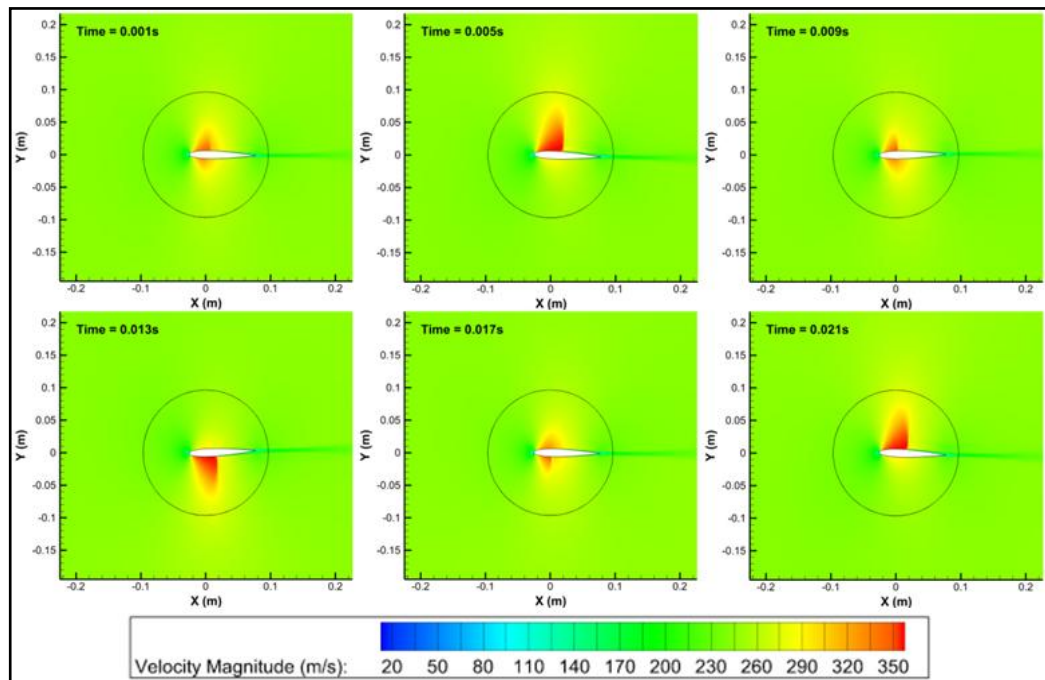


Figure 5.20 Velocity distribution at different time steps, Case-4

It is easily seen from Figure 5.19 and Figure 5.20 that the change of position of airfoil and the change of pressure and velocity distribution with time is consistent with the expected angle of attack due to the forced pitching rates given to the airfoil. To sum up, in this part of the thesis, the numerical method of dynamic motion simulation is validated with the comparisons of numerical and experimental results, and detailed flow field analyses. As a result of this study, it can be concluded that the numerical method validated with a 2D test case model can be used for the simulation of dynamic pitching and rolling motion of missiles.

5.2 Grid Convergence Study for MBF model

As stated in Chapter 4, grid convergence study is carried out with MBF model which has experimental data of static and dynamic aerodynamic coefficients at Mach numbers ranging from subsonic to supersonic flow regimes. Within the grid convergence study, three different surface grids are generated for MBF model. By using these surface grids, it is possible to generate dynamic pitching and rolling motion simulation grids as well as steady simulation grids. As a matter of fact, there

is no need to generate steady simulation grids because it is also possible to perform steady simulations with dynamic pitching or rolling motion simulation grids. Therefore, with these three different surface grids, dynamic rolling motion simulation grids are generated and used within the grid convergence study. Turbulence model of Realizable $k-\epsilon$ is chosen and used in numerical analyses. Grid dependency simulations are performed at three different Mach numbers. Mach numbers are selected from subsonic, transonic and supersonic flow regimes. The grid dependency simulations are performed at these three different flow regimes because the flow may show different characteristics at different flow regimes. The numerical results of axial force coefficients, normal force coefficient slopes and pitching moment coefficient slopes obtained with different grids are compared with each other to see the dependency of the results on grids. The comparisons of simulation results are shown in Figure 5.21, Figure 5.22 and Figure 5.23.

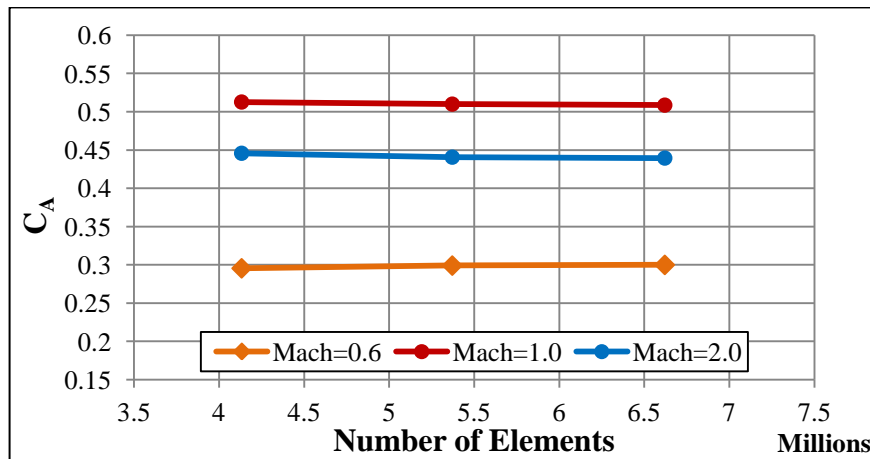


Figure 5.21 Grid convergence for axial force coefficient (MBF model)

Small changes are seen between the coarse and medium grid solutions for all Mach numbers. However, no differences are seen between the results of fine and medium grids. The solutions seem to converge at medium grid because the solutions do not change anymore for all Mach numbers with the increasing number of elements. Therefore, the medium grid is said to be fine enough for the axial force coefficient calculations.

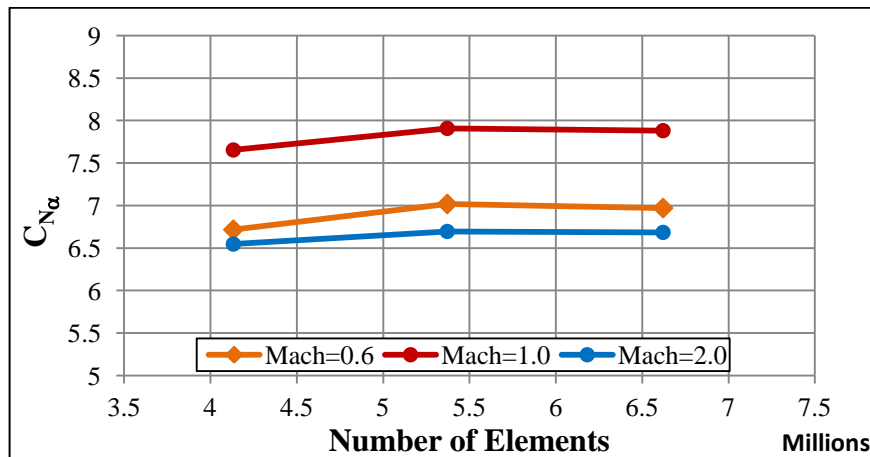


Figure 5.22 Grid convergence for normal force coefficient slope (MBF model)

Relatively great differences are seen between the results of coarse and medium grids. The normal force coefficient slopes increase for all Mach numbers as the number of elements increase. However, the change in normal force coefficient slopes stops at medium grids. In other words, more elements than that of medium grid do not change the normal force coefficient slopes. Therefore, it can be said that the medium grid is fine enough and there is no need to use finer grids.

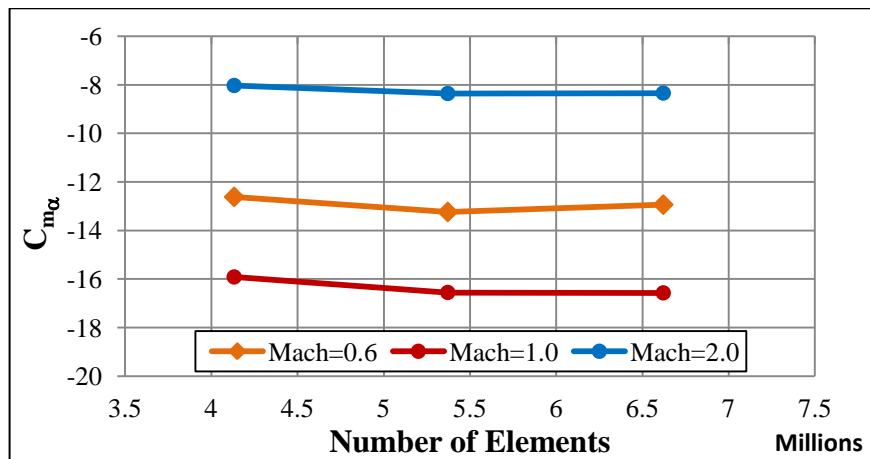


Figure 5.23 Grid convergence for pitching moment coefficient slope (MBF model)

The pitching moment coefficient slopes have same trends with normal force coefficient slopes. The results of coarse and medium grids have relatively great differences. Again, more elements than that of medium grid do not change the results. As a result of grid refinement study, it can be concluded that the medium grid

is fine enough and there is no need to use finer grids for the dynamic motion simulations.

The quality of computational grids also changes the convergence time, or in other words, number of iterations to converge. As an example, the change of residuals during the simulation conducted with medium grid at Mach number 1.0 is given in Figure 5.24.

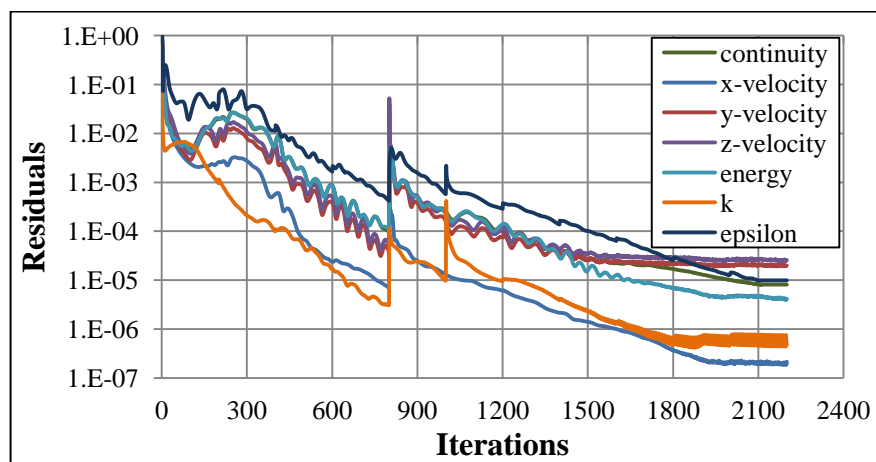


Figure 5.24 Residuals of steady simulations with medium grid (MBF model, Mach=1.0, $\alpha=0^\circ$)

As it is seen in Figure 5.24, the flow variables are changed into a second order discretization at 800th iteration, turbulence kinetic energy, k, and turbulence dissipation rate, ϵ , are changed into a second order discretization at 1000th iteration. It is also seen that all the residuals drop down below the logarithmic value of 0.0001 about 1500 iterations. However, the simulation is not stopped at this point. It is stopped at 2200th iteration where the drop in residuals stopped, or in other words, the residuals converged.

5.3 Turbulence Model Selection for BF and MBF Models

Comprehensive turbulence modeling study is conducted to better model the missile aerodynamics. Because, capabilities of turbulence models may change at different

flow regimes and also they may exhibit different characteristics for different types of geometries. For this reason, steady state CFD analyses are carried out for both BF and MBF models at Mach numbers from subsonic to supersonic regimes. Three different turbulence models namely; Realizable k- ϵ , SST k- ω and Spalart-Allmaras are tried on these models. To validate the numerical results, axial force coefficients, normal force coefficient slopes and pitching moment coefficient slopes of the models are compared with wind tunnel and free flight data available in ref. [8]. In the following sub sections, turbulence model selection study is explained in details.

5.3.1 Test Case Model – 2

Numerical results obtained with different turbulence model simulations are compared with wind tunnel and free flight data [8]. Comparison of axial force coefficients, normal force coefficient slopes and pitching moment coefficient slopes for BF model are given in Figure 5.25, Figure 5.26 and Figure 5.27.

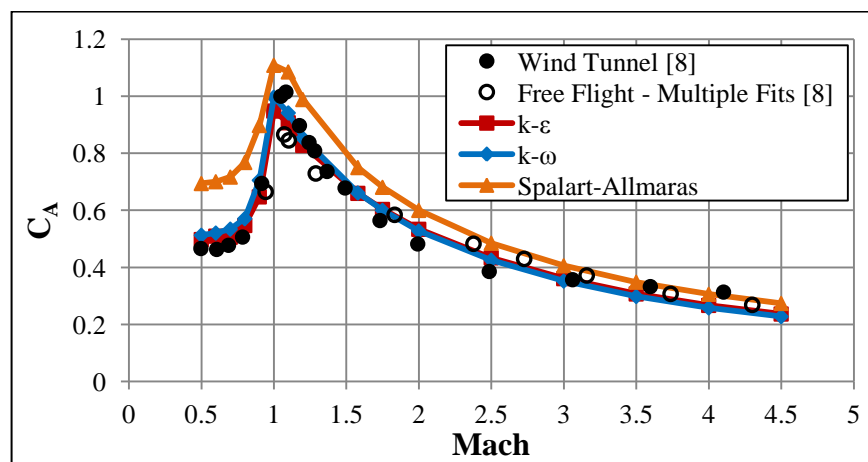


Figure 5.25 Axial force coefficient for different turbulence models (BF model $\alpha=0^\circ$)

Spalart-Allmaras turbulence model simulation results have great differences with experimental data. On the other hand, results of k- ϵ and k- ω turbulence model simulations are very close to each other and also the experimental data. They only have small differences at subsonic and transonic flow regimes. At these regimes, the

results of $k-\epsilon$ turbulence model simulations are closer to the experimental data than that of $k-\omega$ turbulence model.

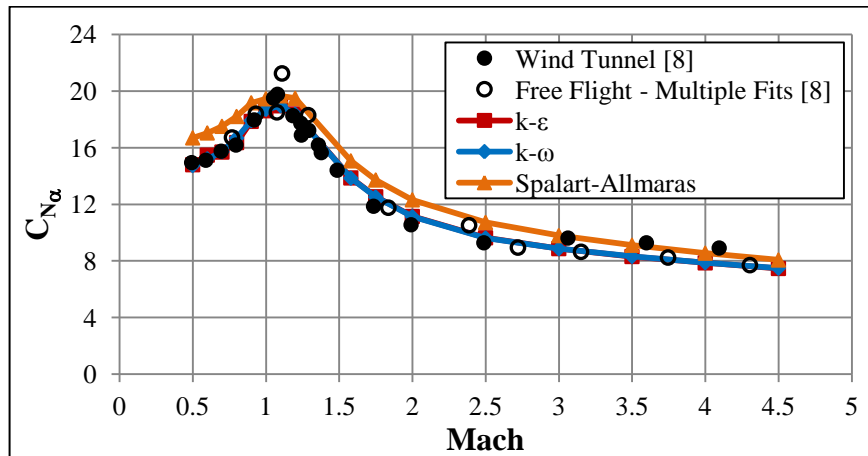


Figure 5.26 Normal force coefficient slope for different turbulence models (BF model)

Similar to the axial force coefficient, Spalart-Allmaras turbulence model simulation results for normal force coefficient slopes have differences with experimental data. However, results of $k-\epsilon$ and $k-\omega$ turbulence model simulations are exactly the same as each other and experimental data throughout the whole flow regime.

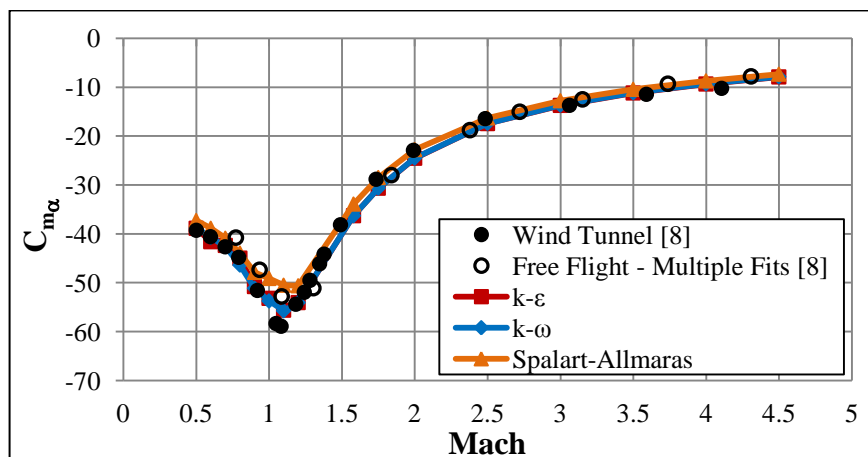


Figure 5.27 Pitching moment coefficient slope for different turbulence models (BF model)

Distinct from the axial force coefficients and normal force coefficient slopes, results of pitching moment coefficients for all turbulence models are close to each other. However, again, results of Spalart-Allmaras turbulence model simulations show small differences with other models between Mach numbers 0.5 and 2. The results of k- ϵ and k- ω turbulence model simulations are again exactly the same as each other and experimental data.

To sum up, numerical results of Spalart-Allmaras turbulence model have deficiencies for the prediction of axial force coefficients and normal force coefficient slopes. The results of k- ϵ and k- ω turbulence model simulations are in general very close to each other and experimental data. However, despite having exactly the same normal force coefficient and pitching moment coefficient slopes, at subsonic and transonic regimes, the results of k- ϵ turbulence model simulations for axial force coefficients are closer to the experimental data than that of k- ω turbulence model. As a result, it can be concluded that numerical results of k- ϵ turbulence model simulations best fit with the experimental data for BF model for all flow regimes. Therefore, this model can be selected and used for the dynamic motion simulations of BF model.

5.3.2 Test Case Model - 3

This model has no wind tunnel data of static aerodynamic coefficients. It has only free flight test data and these experimental data has discrepancies. Comparison of numerical results with free flight test data for axial force coefficient, normal force coefficient slopes and pitching moment coefficient slopes are given in Figure 5.28, Figure 5.29 and Figure 5.30 respectively.

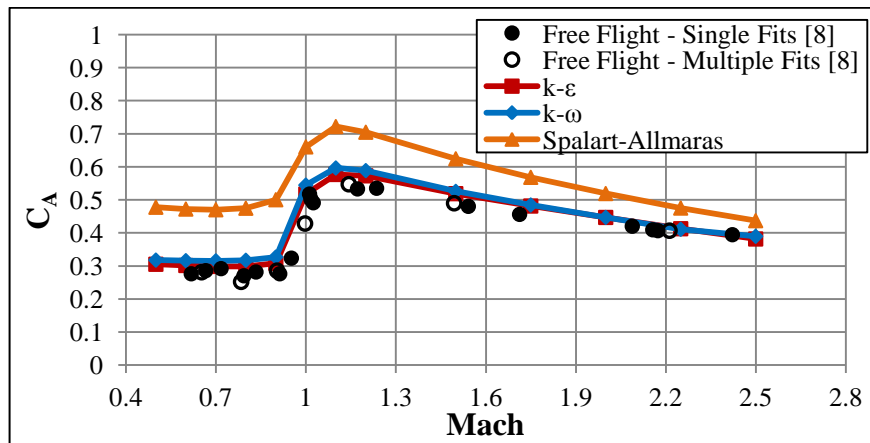


Figure 5.28 Axial force coefficient for different turbulence models (MBF model, $\alpha=0^\circ$)

Similar to the BF model, the axial force coefficient results of Spalart-Allmaras turbulence model simulations have great differences with the results of other turbulence models simulations and experimental data. Again, k- ϵ turbulence model simulation results are closer to the experimental data at subsonic and transonic flow regimes than the results of k- ω turbulence model simulations.

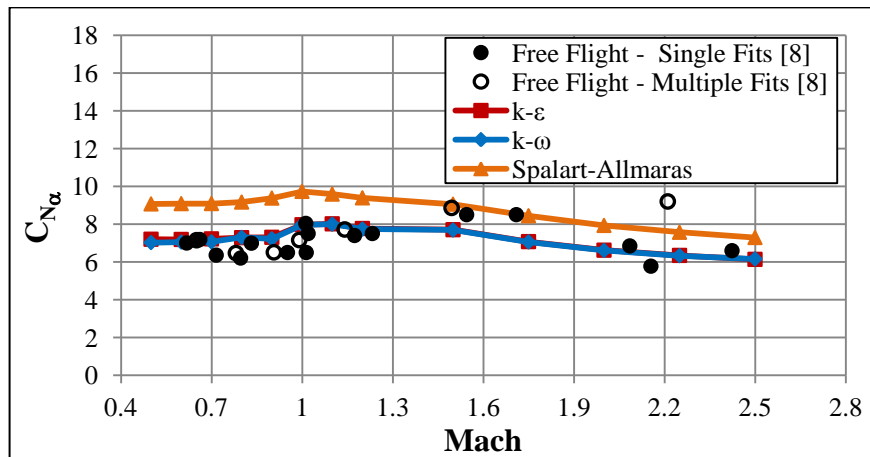


Figure 5.29 Normal force coefficient slope for different turbulence models (MBF model)

As it is shown in Figure 5.29, the trends of all turbulence model simulation results are similar to each other. However, Spalart-Allmaras turbulence model simulation results have great differences with experimental data. The results of other turbulence

models simulations are exactly the same and they show good agreement with experimental data throughout the whole flow regimes.

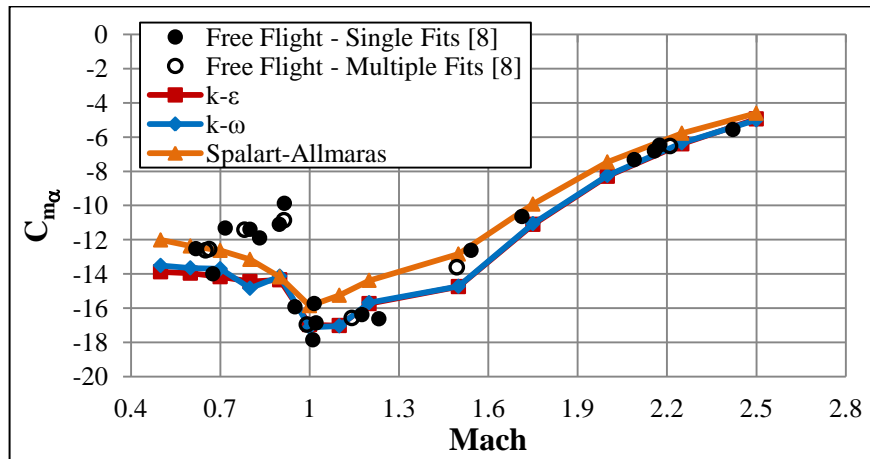


Figure 5.30 Pitching moment coefficient slope for different turbulence models (MBF model)

Especially at subsonic regime, great discrepancies are seen in experimental data. Therefore, the experimental results of this regime may not be reliable. The numerical results of pitching moment coefficient slopes for different turbulence model simulations are similar to the BF model. The results of Spalart-Allmaras turbulence model simulations have great differences with experimental data and the other turbulence model simulations results. The results of $k-\epsilon$ and $k-\omega$ turbulence model simulation results are again very close to each other for all Mach numbers.

As a result of turbulence model selection study, it is shown that the numerical results of $k-\epsilon$ turbulence model simulations best fit with the experimental data. Therefore, it can be concluded that $k-\epsilon$ turbulence model is the most suitable turbulence model for these types of geometries at these flow regimes. This turbulence model is also expected to give better results for dynamic motion simulations.

Before finishing the turbulence model selection study, the flow field analyses are performed. For this purpose, pressure and Mach number distribution over MBF model and flow field at Mach number 1.5 at zero angle of attack are given as an example in Figure 5.31 and Figure 5.32 respectively.

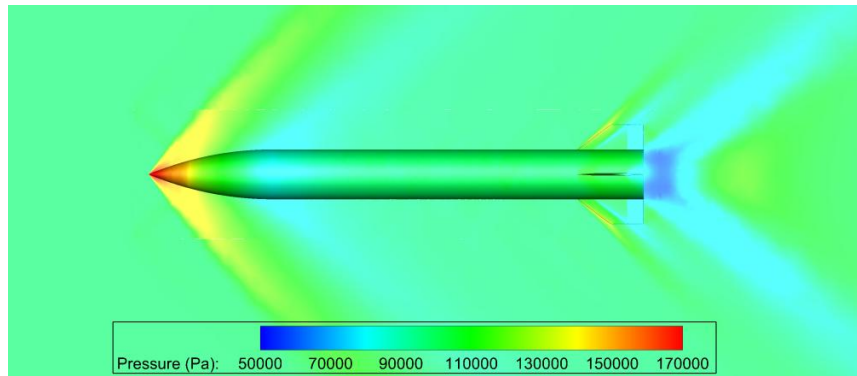


Figure 5.31 Pressure distribution over MBF model and flow field (Mach=1.5, $\alpha=0^\circ$)

High static pressure is shown at the nose of the MBF model because of the oblique shock. At the junction region between the nose and the body, the expansion is seen and thus at this region the static pressure decreases smoothly. Resulting from the leading edge angles of the fins, again, oblique shocks occur and the higher increase in static pressure is seen at the leading edges of the fins. At the base region of the model due to the higher change in surface angle, strong expansion and thus the higher drop in static pressure is seen.

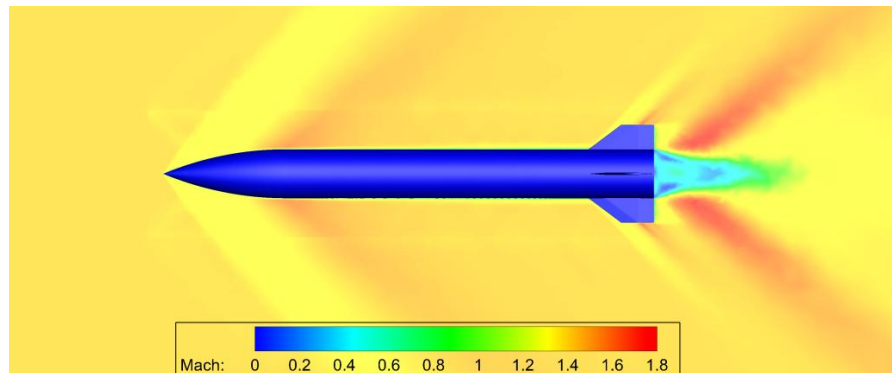


Figure 5.32 Mach number distribution over MBF model and flow field (Mach=1.5, $\alpha=0^\circ$)

As expected, due to the no-slip boundary conditions defined for the surfaces, zero Mach number occurs at the surfaces of the model. Oblique shocks are seen at the nose and at the leading edge of the fins. At the base region of the model, strong expansion is shown and after that at the wake region again strong oblique shock occurs.

5.4 Parametric Study

In this part of the thesis, parametric studies conducted for dynamic pitching and rolling motion simulations are explained in details. The parametric studies are carried out to reveal the characteristics of dynamic pitching and rolling motions. After getting enough knowledge about the characteristics of dynamic pitching and rolling motion, the comparison of the numerical and experimental results are presented. Details of parametric studies are explained in the following sub sections.

5.4.1 Pitching motion Simulations

In Eq. (1-8), the pitching rate is defined as a sinusoidal function. The variables of this function are the pitching rate amplitude (A) and the pitching rate frequency (f). In this part of the thesis, the effects of these variables and also the pitching motion at different angle of attacks are investigated individually.

5.4.1.1 Effects of Pitching Rate Amplitude

In this part, effects of pitching rate amplitude are investigated. Four different pitching rate amplitudes are given to the MBF model at different Mach numbers by keeping the pitching rate frequency constant ($f=62.5$ Hz). The changes of pitching rate amplitudes with time used in numerical simulations are given in Figure 5.33.

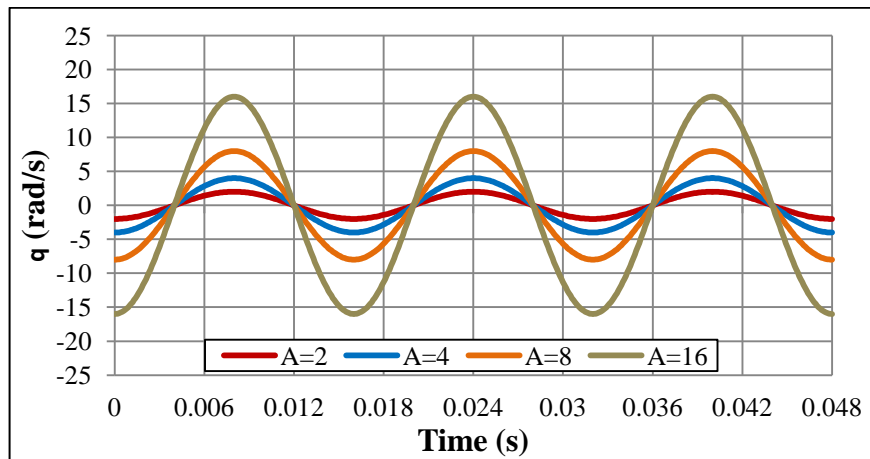


Figure 5.33 Sinusoidal pitching rates for different pitching rate amplitudes

As it is shown in Figure 5.33, simulations are performed to complete three periods. Time histories of resultant pitching moment coefficients for the simulations conducted with different pitching rates at Mach number 0.6 is given in Figure 5.34.

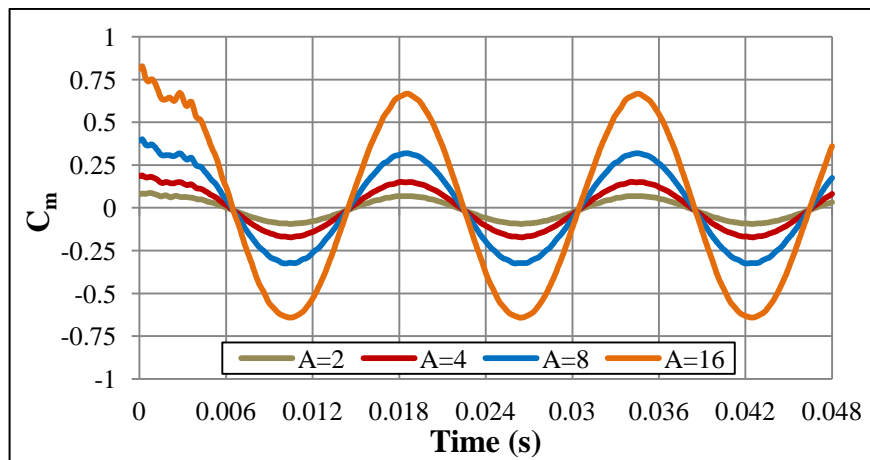


Figure 5.34 Pitching moment coefficient vs. time for different pitching rate amplitudes (MBF model, Mach=0.6)

It is seen in Figure 5.34 that small oscillations occur at the beginning of simulations. At about 0.004 second, which is the quarter period, the oscillations diminish and the pitching moment coefficients start to converge. It is also seen that the third period repeats the one before. Therefore, it can be said that for this case three periods is enough to achieve converged solutions. The changes of pitching moment coefficient with angle of attack belonging to the last periods are shown in Figure 5.35.

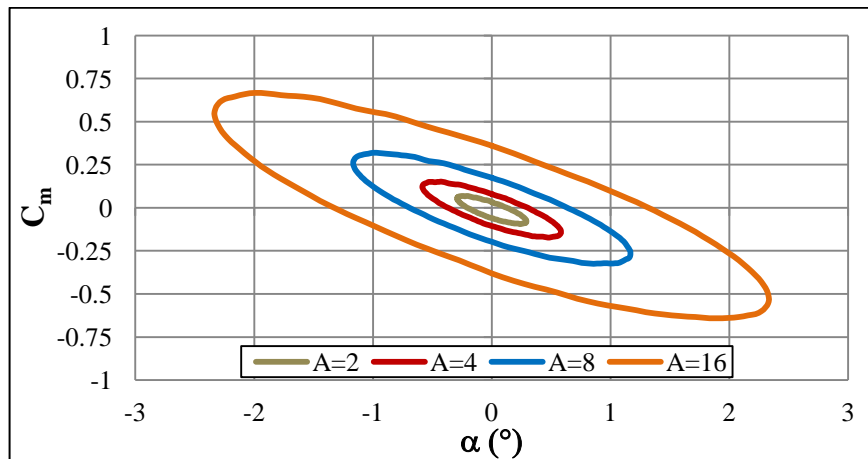


Figure 5.35 Pitching moment coefficient vs. angle of attack for different pitching rate amplitudes (MBF model, Mach=0.6)

MBF model is exposed to different resultant angle of attacks because while using different pitching rate amplitudes, same pitching rate frequencies ($f=62.5$ Hz) are used in the simulations. As expected with increasing pitching rate amplitudes, the pitching moment coefficient increases for the same angle of attacks. In other words, the hystereses in the pitching moment coefficient curves grow with increasing pitching rate amplitudes.

The changes of dynamic pitching moment coefficients with reduced frequencies for the last period results are given in Figure 5.36.

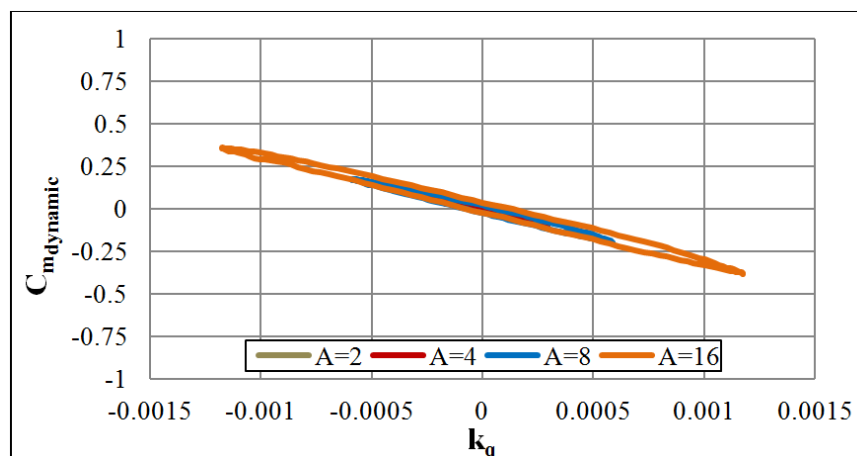


Figure 5.36 Dynamic pitching moment coefficient vs. reduced frequency for different pitching rate amplitudes (MBF model, Mach=0.6)

As assumed, dynamic pitching moment coefficients change almost linearly with reduced frequencies. Only small hysteresis is seen in the simulations of 16 rad/s pitching rate amplitude. Because, for this pitching rate amplitude the model is exposed to larger angle of attacks in which the non-linear effects start. As a result, the smaller pitching rate amplitudes are more convenient for the simulations of pitching motion at subsonic speeds.

As a second case, pitching moment simulations conducted at Mach number 1.2 is examined. Time histories of resultant pitching moment coefficients for this Mach number are given in Figure 5.37.

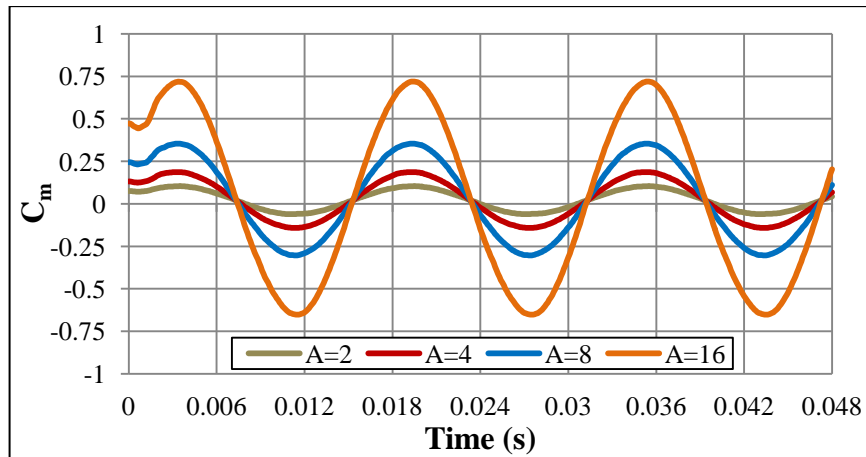


Figure 5.37 Pitching moment coefficient vs. time for different pitching rate amplitudes (MBF model, Mach=1.2)

Again small oscillations are seen at the beginning of the simulations. However, this time the oscillations diminish at about 0.002 seconds and the time history of pitching moment coefficients of third period repeats the one before.

The changes of pitching moment coefficients with resultant angle of attacks belonging to the third periods are given in Figure 5.38.

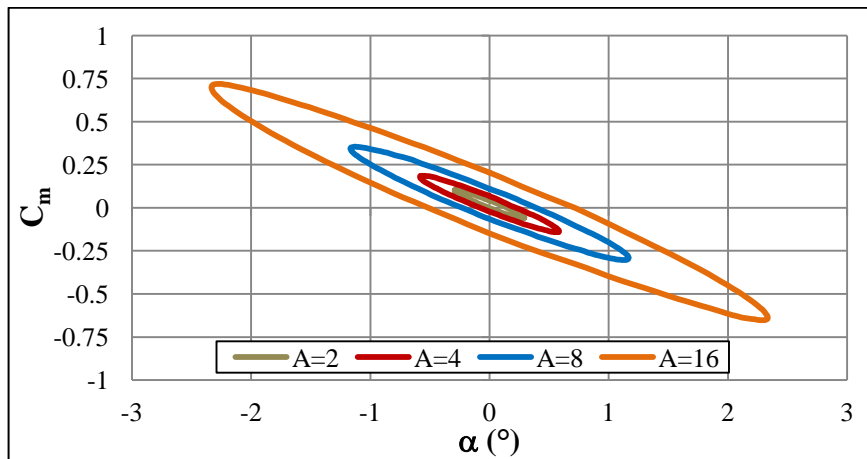


Figure 5.38 Pitching moment coefficient vs. angle of attack for different pitching rate amplitudes (MBF model, Mach=1.2)

Similar to the subsonic case, the pitching moment coefficient curves have hystereses of different magnitudes. However, at this Mach number, the hystereses in the pitching moment coefficient are smaller than the ones at Mach number 0.6.

The changes of dynamic pitching moment coefficients with reduced frequencies for the results of last periods are given in Figure 5.39.

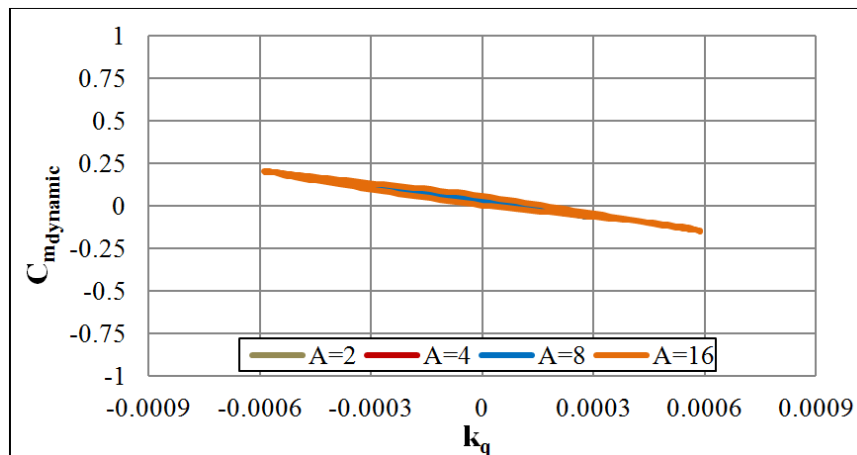


Figure 5.39 Dynamic pitching moment coefficient vs. reduced frequency for different pitching rate amplitudes (MBF model, Mach=1.2)

Again as expected, the dynamic pitching moment coefficients change almost linearly with reduced frequencies for all pitching rates. Again, for this case, the non-linearity effects are seen in the simulation having pitching rate amplitude of 16 rad/s.

Finally, the comparison of the computed pitch damping coefficients belonging to different pitching rate amplitudes is presented in Figure 5.40.

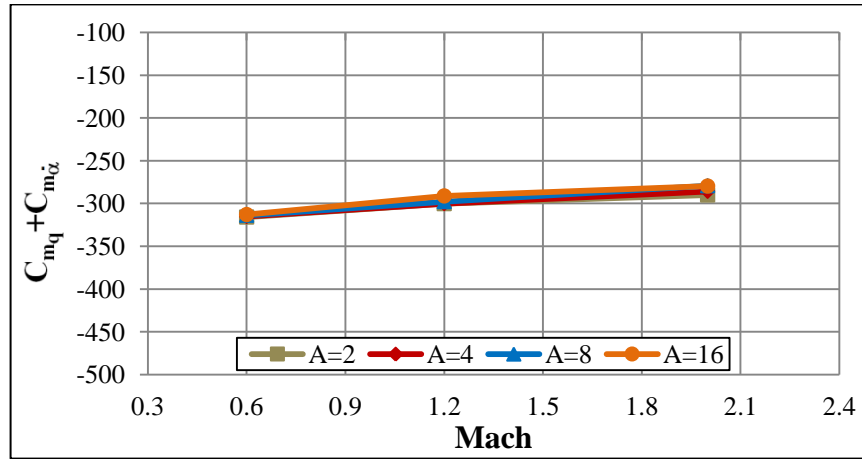


Figure 5.40 Pitch damping coefficients of MBF model for different pitching rate amplitudes

Computed results of all different pitching rate amplitude simulations are very close each other. Small differences are seen in supersonic flow regime however, these small differences are negligible.

As a result of parametric study on pitching rate amplitude, it is seen that the exposed angle of attack resulting from the pitching rate amplitude should be less than one degree for both subsonic and supersonic flow regimes. Because, at angle of attacks greater than one degree, the assumption of linearity of the dynamic pitching moment coefficient vs. reduced frequency curve fails. It is also concluded that the pitch damping coefficient is independent of pitching rate amplitudes in feasible ranges.

5.4.1.2 Effects of Pitching Rate Frequency

In this part, effects of pitching rate frequency are investigated. Four different pitching rate frequencies (f) are given to the MBF model at different Mach numbers by keeping the pitching rate amplitude constant ($A=2$ rad/s). Two different Mach numbers are used in parametric study. One of them is at subsonic and the other one is at supersonic flow regimes.

The changes of pitching rates with time for both cases are shown in Figure 5.41.

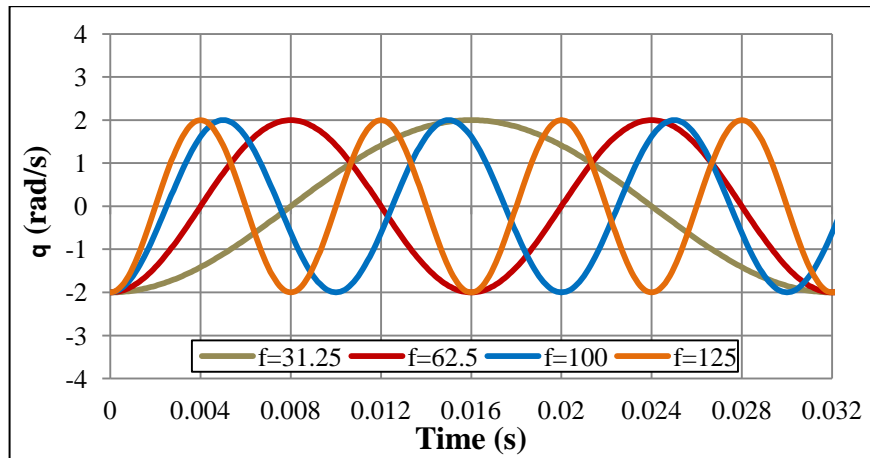


Figure 5.41 Sinusoidal pitching rates for different pitching rate frequencies

Simulations are performed to complete at least three periods. However, in Figure 5.41, only the 0.032 seconds of the pitching rates are shown for better illustration.

Time histories of pitching moment coefficients for the simulations carried out with different pitching rate frequencies at Mach number 0.6 are given in Figure 5.42.

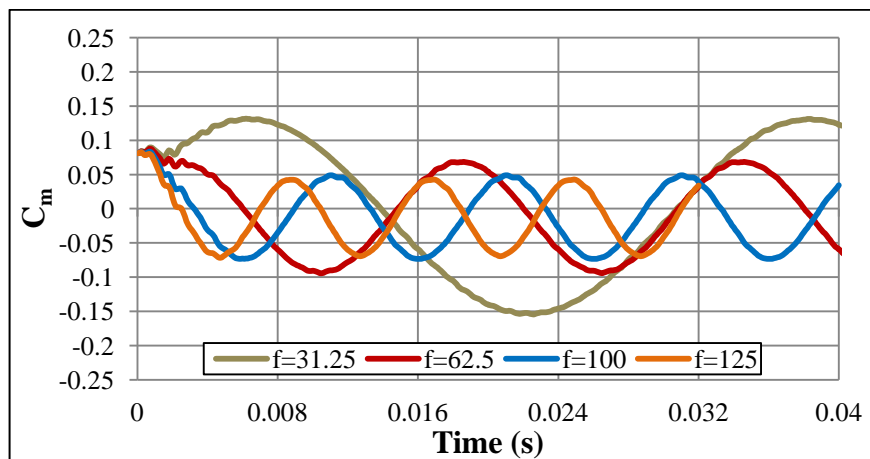


Figure 5.42 Pitching moment coefficient vs. time for different pitching rate frequencies (MBF model, Mach=0.6)

Small oscillations are seen up to 0.005 seconds which is about the half period of the smallest period ($f=125$ Hz). From this point the oscillations diminish and the pitching

moment coefficients start to converge. The simulations are finished when the results of last period repeats the one before. This is achieved at four periods for the frequency of 100 and 125 Hz, and at three periods for the frequency of 31.25 and 62.5 Hz.

The changes of resultant pitching moment coefficients with resultant angle of attacks belonging to the last periods are given in Figure 5.43.

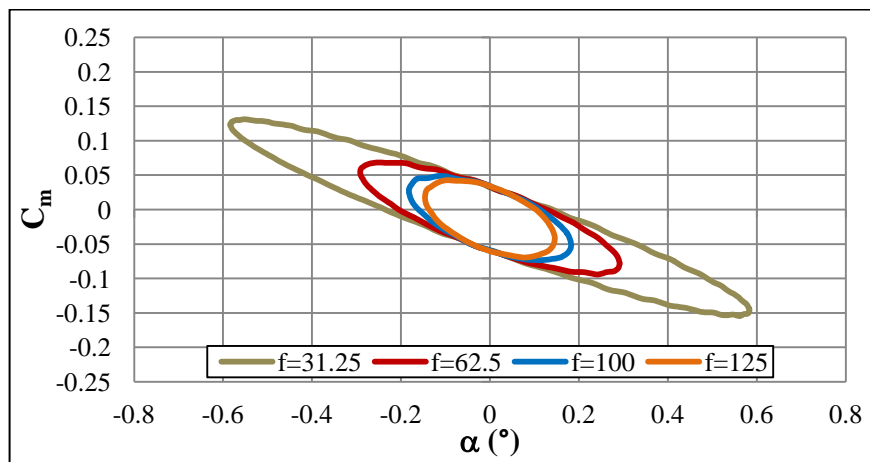


Figure 5.43 Pitching moment coefficient vs. angle of attack for different pitching rate frequencies (MBF model, Mach=0.6)

The hysteresis loop of pitching moment coefficients increases while the frequency of the sinusoidal pitching rate decreases. However, as it is seen in Figure 5.43, all the hysteresis crosses the same value of pitching moment coefficient at zero angle of attack. This is an expected result because all the sinusoidal pitching rates have same pitching rate amplitude of 2 rad/s.

The changes of dynamic pitching moment coefficients with reduced frequencies for Mach number 0.6 are given in Figure 5.44.

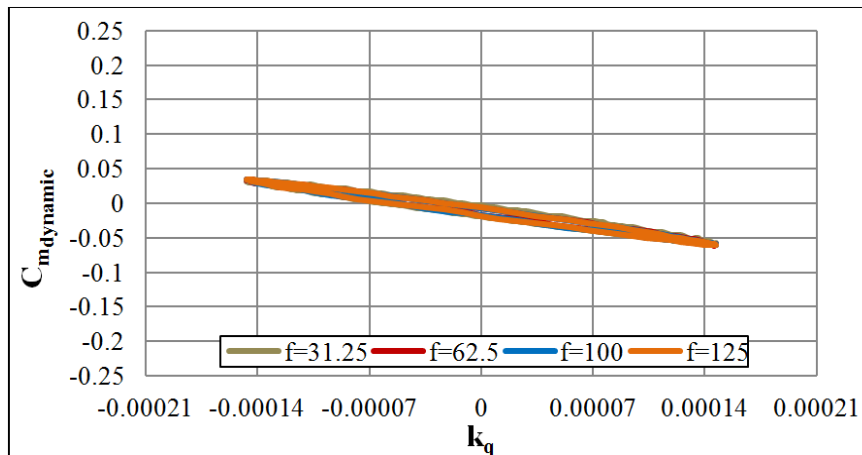


Figure 5.44 Dynamic pitching moment coefficient vs. reduced frequency for different pitching rate frequencies (MBF model, Mach=0.6)

As it is seen in above figure, the curves of all pitching rate simulations are exactly same. Small hystereses are seen in the curves. However, the hysteresis are negligible and the curves can be assumed as linear. Time histories of pitching moment coefficients for the simulations conducted at Mach 1.2 are shown in Figure 5.45.

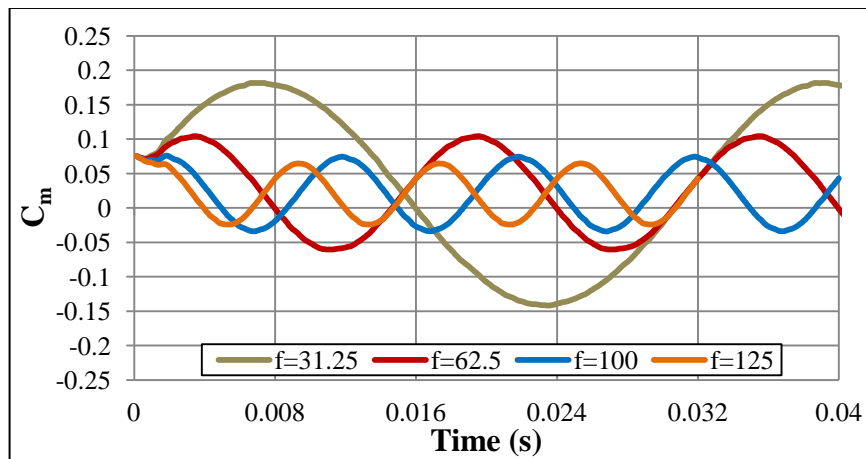


Figure 5.45 Pitching moment coefficient vs. time for different pitching rate frequencies (MBF model, Mach=1.2)

Similar to the subsonic case, small oscillations are seen in pitching moment coefficients. However, for this case, the convergences are achieved earlier than that of subsonic case. Again three periods are completed for the simulations having pitching rate frequencies of 31.25 and 62.5 Hz, and four periods are completed for the simulations having the pitching rate frequencies of 100 and 125 Hz.

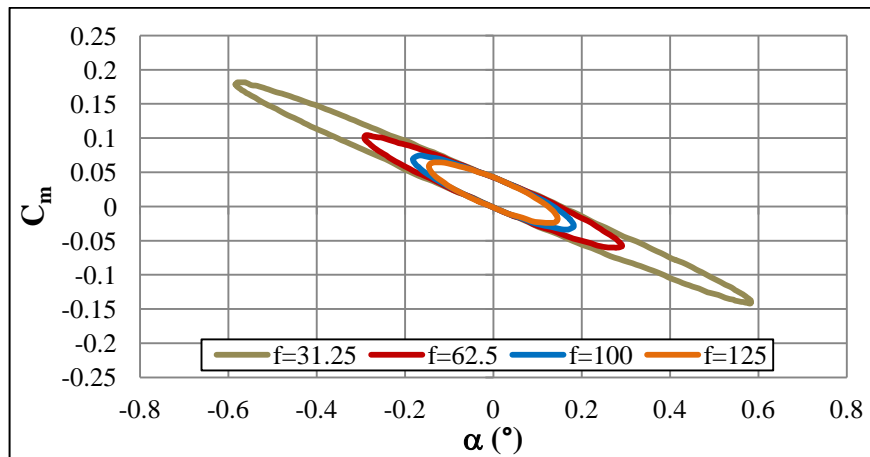


Figure 5.46 Pitching moment coefficient vs. angle of attack for different pitching rate frequencies (MBF model, Mach=1.2)

Similar to the Mach number 0.6 simulations, the hysteresis loop of pitching moment coefficient increases with the decrease in frequency. Again, all the hysteresis crosses the same value of pitching moment coefficient at zero angle of attack. This is also an expected result because all the sinusoidal pitching rates have same pitching rate amplitudes amplitude of 2 rad/s.

In Figure 5.47, the changes of dynamic pitching moment coefficient with respect to reduced for the results of last periods are given.

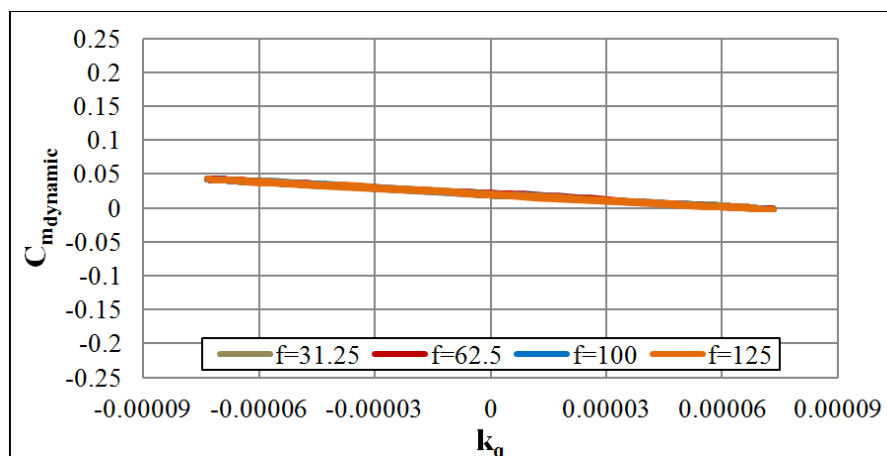


Figure 5.47 Pitching moment coefficient vs. reduced frequency for different pitching rate frequencies (MBF model, Mach=1.2)

The curves of dynamic pitching moment coefficient versus reduced frequency are exactly the same as each other. Moreover, they all have absolutely linear trends. Therefore, it can be easily said that the assumption of linearity is totally valid for all pitching rates. It can be also concluded that the frequency of the sinusoidal pitching rate have no effect on the dynamic pitching moment coefficient versus reduced frequency curve. The computed results of pitch damping coefficients are presented in Figure 5.48.

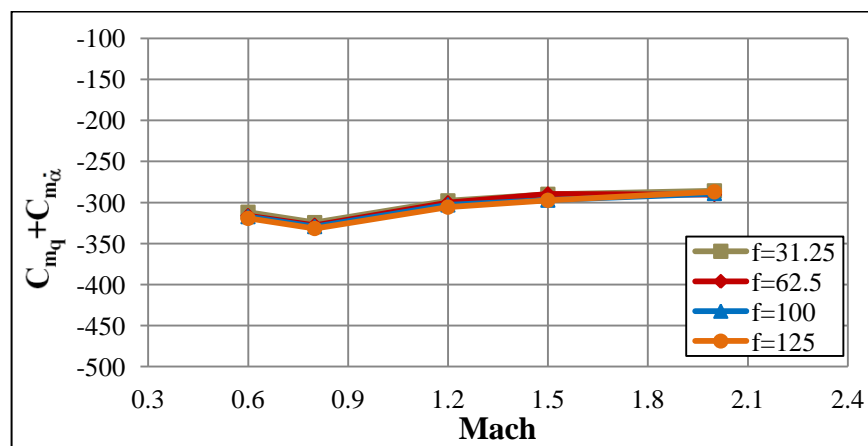


Figure 5.48 Pitch damping coefficients of MBF model for different pitching rate frequencies

The computed pitch damping coefficients by using different pitching rate frequencies shows good agreement. The maximum differences between the numerical results occur at Mach number 1.5 which is less than 5 %. It is obviously seen from these results that pitch damping coefficient is independent of pitching rate frequency. As a result of parametric study conducted on pitching rate frequencies, it can be concluded that any feasible pitching rate frequencies as investigated in this study can be used for the calculation of pitch damping coefficient.

5.4.1.3 Effects of Angle of Attack

The same procedure used for pitching motion simulations at zero angle of attack is also used for the simulations performed at any angle of attacks. The only difference is the angle of attacks defined to the pressure far field boundary conditions.

It is found in literature that both BF and MBF models have experimental data at different angle of attacks and Mach numbers. The MBF model has experimental data at small angle of attacks ranging from -2 to 5 degree at Mach number 1.75 available in ref. [7]. The BF model has experimental data up to 20 degree angle of attack at Mach number 1.96 available in ref. [39]. In this part of the study, only the MBF model is examined in details. The results of the BF model are presented in the following section.

Pitching rate frequency of 62.5 Hz and pitching rate amplitude of 2 rad/s are forced to both models for all angles of attacks. The simulations are performed to complete three periods. Because, it is known from the previous analyses that simulation of three periods are enough for achieving converged solutions with this pitching rate frequency and amplitude. Time histories of pitching moment coefficients for MBF model at different angle of attack simulations are given as an example.

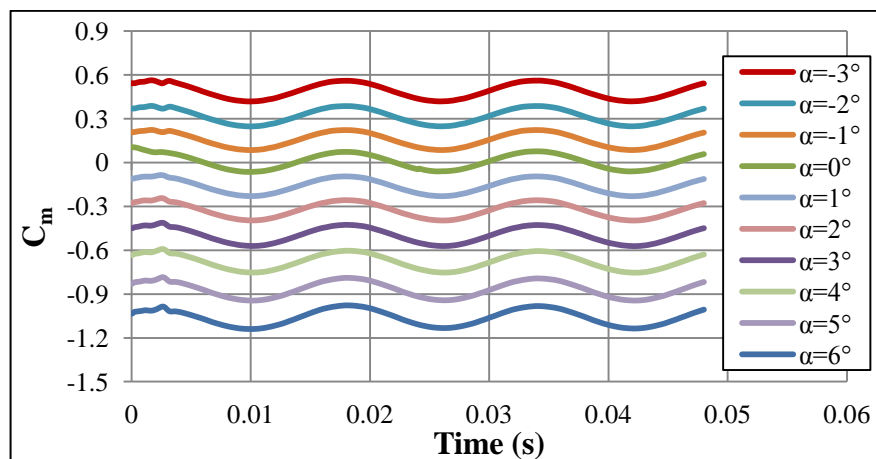


Figure 5.49 Pitching moment coefficient vs. time for different mean angle of attacks (MBF model, $X_{CG}=5D$, Mach=1.75)

As expected sinusoidal waves of pitching moment coefficients are shown. At the beginning of the simulations small oscillations are seen at about quarter periods. Then the solutions start to converge to sinusoidal waves. As it is seen in Figure 5.49, the increment in angle of attacks is a constant value of one degree. The differences between the sinusoidal pitching moment coefficient curves are also seen constant for all angles of attacks. As it is mentioned before, for small angle of attacks the change in pitching moment coefficients is almost linear. Therefore, the computed pitch

damping coefficients from these small angles of attacks are expected to have closer values. The changes of pitching moment coefficients with angle of attacks for the last periods of the simulations are given in Figure 5.50.

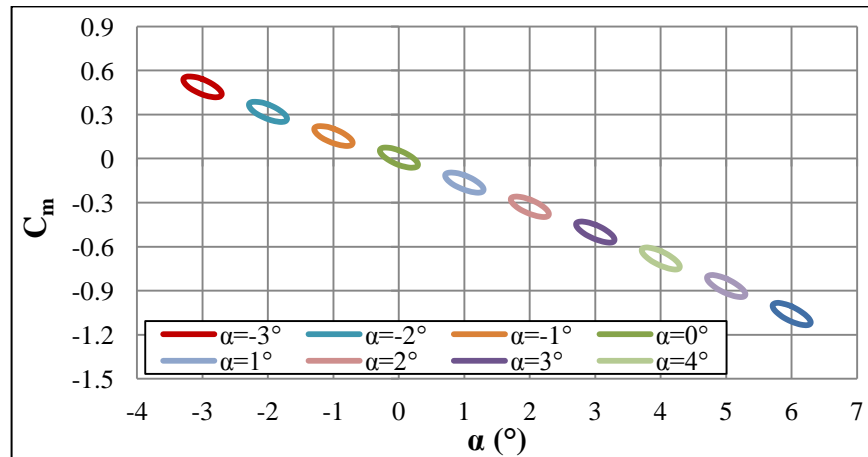


Figure 5.50 Pitching moment coefficient vs. angle of attack, (MBF model, $X_{CG}=5D$, Mach=1.75)

Similar hystereses, as expected, occur at different angle of attacks. As mentioned before, all the simulations have the same pitching rate amplitude and frequency. Therefore, the pitch damping coefficient for these small angles of attacks are expected to be close to each other.

5.4.1.4 Results

The comparisons of the numerical and experimental results of pitching damping coefficients are presented here. Firstly, pitch damping coefficients of BF and MBF models at zero angle of attack are compared. Then, the comparisons of numerical and experimental results for both models at angle of attacks are presented. All the results of pitching motion simulations used in the comparisons have the same pitching rate amplitude of 2 rad/s and frequency of 62.5 Hz.

The comparison of numerical and experimental results for BF model at zero angle of attack is given in Figure 5.51.

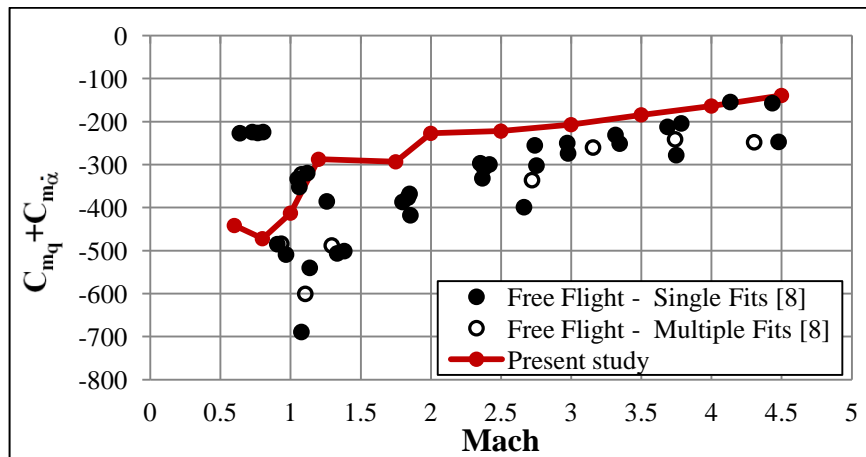


Figure 5.51 Pitch damping coefficient vs. Mach number (BF model, $X_{CG}=5.5D$, $\alpha=0^\circ$)

As stated before, great discrepancies are seen in the experimental results. As it is seen in Figure 5.51, these discrepancies may be greater than 100 %. These great discrepancies may be resulted from the difficulties of free flight tests. Because conducting the free flight tests and obtaining the aerodynamic coefficients from these tests are very difficult as compared to the wind tunnels. This is why the wind tunnel results have small discrepancies as compared to the free flight tests.

The comparison of numerical and experimental results should be done by considering these difficulties and discrepancies.

At subsonic regime, great differences are seen between the experimental and numerical results. Between the Mach numbers 0.9 and 1.5, where the experimental data has great discrepancies, the numerical results have great jumps in the range of experimental data. The trends of numerical and experimental results show good agreement at flow regimes greater than Mach number 1.5. The discrepancies in experimental data get smaller at this regime. Moreover, the differences between the numerical and experimental results decrease with an increasing Mach number. Another point is that, the pitch damping coefficient decreases in magnitude with an increasing Mach number.

The comparison of numerical and experimental results for MBF model at zero angle of attack is shown in Figure 5.52.

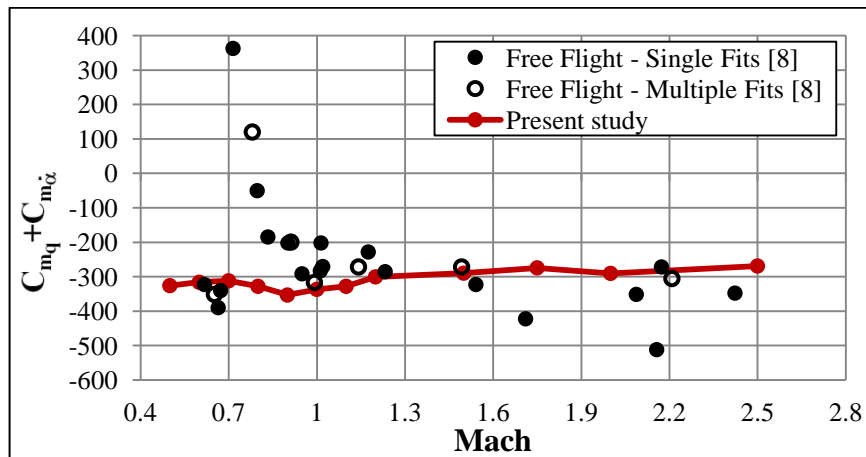


Figure 5.52 Pitch damping coefficient vs. Mach number (MBF model, $X_{CG}=4.8D$, $\alpha=0^\circ$)

Similar to the BF model, experimental results of MBF model have also great discrepancies especially at subsonic flow regime. Between Mach numbers 0.7 and 0.8, experimental results of pitch damping coefficient are positive which is physically meaningless. Apart from this region, the numerical and experimental results are in good agreement with an acceptable error margins. Distinct from the BF model, the pitch damping coefficients are almost remain constant with an increasing Mach number.

The pitch damping coefficients at different angle of attacks are also investigated as a part of present study. Firstly, effect of small angle of attacks is investigated. It is found in literature that two different wind tunnels [39] have measurements of pitch damping coefficient for MBF model at small angle of attacks. Therefore, this model is used for the comparisons of the numerical and experimental results. Then, the pitch damping coefficients at large angle of attacks are investigated. The BF model is used for this purpose because it has wind tunnel measurement [40] of pitch damping coefficients up to 20 degree angle of attacks.

Numerical and experimental results of pitch damping coefficients at small angle of attacks at Mach number 1.75 are compared in the following figure.

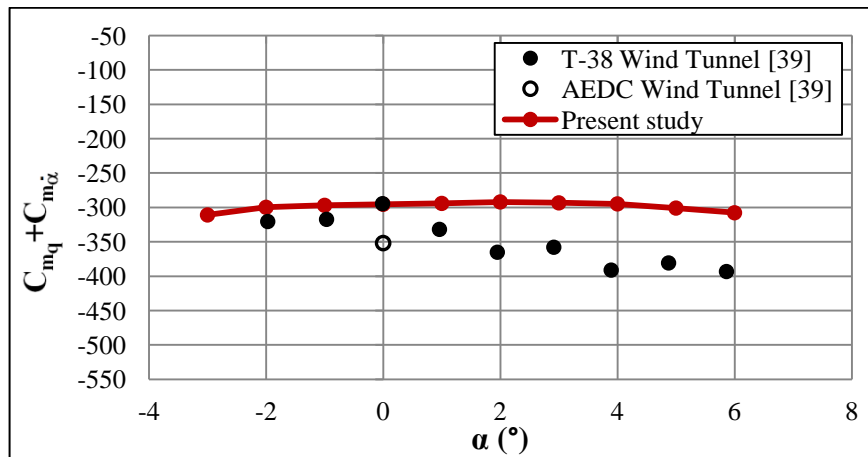


Figure 5.53 Pitch damping coefficient vs. angle of attack [39], (MBF model, $X_{CG}=5D$, Mach=1.75)

Small increase in magnitude of pitch damping coefficient is seen in experimental data with the increase of angle of attack. However, this increase is not seen in numerical results. The numerical results have negligible changes within this angle of attack range.

The change of pitching moment coefficient with angle of attack for BF model at Mach number 1.96 is given in Figure 5.54.

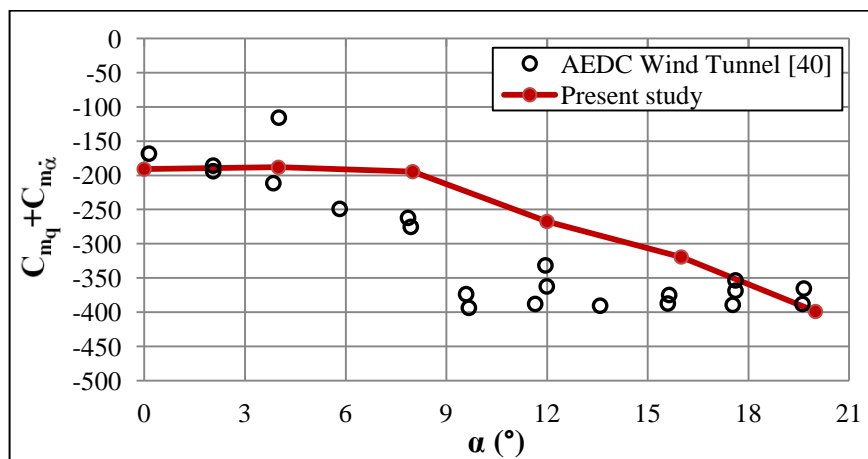


Figure 5.54 Pitch damping coefficient vs. angle of attack (BF model, $X_{CG}=6.1D$, Mach=1.96)

Similar to the MBF model, no change in pitching moment coefficient is seen at small angle of attacks. However, at angle of attacks greater than eight, the magnitude of

pitch damping coefficient increases with an increasing angle of attacks. Same trend is seen in both numerical and experimental results. The numerical and experimental results are close to each other throughout the whole angle of attack range.

To sum up, determination of pitch damping coefficient with experiment and CFD techniques is very difficult. Even in wind tunnels and free flight tests, more than 100 % discrepancies are seen for the tests run at same flight conditions. Besides these discrepancies, wind tunnel and free flight tests are very expensive and time consuming. Moreover, conducting these tests is not possible at the preliminary and conceptual design phases of the missiles. At this point, determination of pitch damping coefficients with CFD techniques takes an important role. As it is seen from the comparisons of numerical results with experimental data, the numerical results are very accurate and reliable. In conclusion, the numerical method presented in this study can be used for the prediction of pitch damping coefficient at the conceptual and detailed design phases of any missile configurations.

5.4.1.5 Flow Field Visualization

In order to better understand the characteristics of dynamic pitching motions, the flow field analyses are performed for one case. For this purpose, the pitching motion of MBF model at Mach number 0.6 and zero angle of attack is examined in details. The case has pitching rate amplitude of 16 rad/s and pitching rate frequency of 62.5 Hz. In flow field analyzes the expected and the resultant flow features are compared with each other. For this purpose, it is focused on the expected and the resultant values of the surface flow and angle of attacks (position in pitch plane).

The change of pressure and surface flow over MBF model at specified time steps are given in Table 5.1.

Table 5.1 Pressure distribution and surface flow on MBF model (Mach=0.6, A=16 rad/s, f=62.5 Hz)

Pitch Rate and Angle of Attack	Pressure (Pa)	
Time = 0.001 s q = -14.7821 rad/s $\alpha = -0.8934^\circ$		
Time = 0.003 s q = -6.1229 rad/s $\alpha = -2.1567^\circ$		
Time = 0.005 s q = 6.1229 rad/s $\alpha = -2.1567^\circ$		
Time = 0.007 s q = 14.7821 rad/s $\alpha = -0.8934^\circ$		
Time = 0.009 s q = 14.7821 rad/s $\alpha = 0.8934^\circ$		
Time = 0.011 s q = 6.1229 rad/s $\alpha = 2.1567^\circ$		

As stated before, the period of the pitching motion is 0.016 seconds ($f=62.5$ Hz) and the pitching motion starts at zero angle of attack.

At 0.001 second the model is expected to have pitch down motion with a decreasing pitching rate. Therefore, at this time step the model should have negative angle of attack. As is it easily seen in Table 5.1, the positions and surface flow of the model shown in the figures is consistent with the expected values.

At 0.004 second, which is the quarter period of the motion, the MBF model is expected to have the lowest angle of attack and zero pitching rate. In Table 5.1, the pressure and surface flow of the model at 0.003 and 0.005 seconds are given. At these two time steps the model is expected to be on same positions. Moreover, for the time step 0.003 the model is expected to have pitch down motion with a decreasing

pitching rate and for the time step 0.005 the model is expected to have pitch up motion with an increasing pitching rate. Therefore, despite the being at same position the model is expected have surface flows of opposite directions. The figures of these time steps shown in Table 5.1 are totally consistent with the expected values.

At 0.008 second, which is the half period of the motion, the model is expected to return the starting point which is the zero angle of attack. In Table 5.1, the figures of 0.001 second before and after the half period are presented. Due to the nature of sinusoidal pitching rates the model is expected to have same magnitude of angle of attacks with different signs. The model is expected to come to the zero angle of attack position with a pitching up motion in the figure belonging to 0.007 second. In the figure belonging to 0.009 second, the model is also expected to have pitching up motion. However, for this time step, the model is expected to have positive angle of attacks. In addition, the surface flows of the model for these two time steps are expected to be similar. The surface flows and angle of attacks shown in figures for these time steps given in Table 5.1 totally agree with the expected results mentioned here.

At 0.012 second, the model should have completed the 3 quarter periods. In other words, the model should be exposed to maximum positive angle of attacks. It should stop at this time step and then returns to the initial position, that is, zero angle of attack position. In Table 5.1, the figure of 0.011 second is given. At this time step, the model is expected to have pitching up motion with a decreasing pitching rate. The model is also expected to have greater angle of attacks than that of 0.009 second. As it is easily seen in Table 5.1, the surface flows and positions of models seen in figure belonging to 0.011 second is absolutely consistent with the expected values.

To sum up, the flow field analyses show that the model does the same motion as it is defined to do. The surface flows and exposed angle of attacks are exactly the same as the expected values.

5.4.2 Rolling Motion Simulations

In Eq. (1-15), the rolling rate is defined as a sinusoidal function. The variables of this function are the rolling rate amplitude (A) and the rolling rate frequency (f). In this part of the study, the effects of these variables and also the angle of attacks on rolling motion are investigated one by one. Parametric studies are carried out on BF model. Because this model has wide range of experimental data containing subsonic, transonic, supersonic flow regimes and different angle of attacks. Details of the parametric studies are explained in the following sub sections.

5.4.2.1 Effects of Rolling Rate Amplitude

In this part, effects of rolling rate amplitude are investigated. Four different rolling rate amplitudes are given to the BF model at different Mach numbers by keeping the rolling rate frequency constant ($f=100$ Hz). The changes of rolling rate amplitudes with time used in present study are given in Figure 5.55.

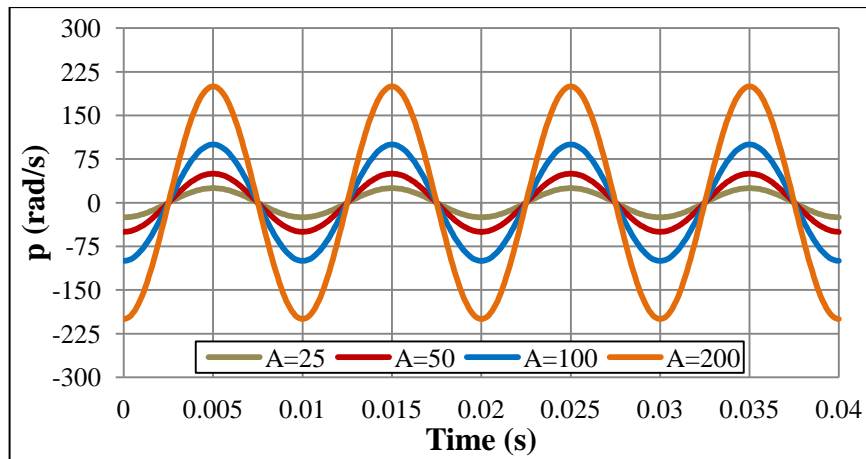


Figure 5.55 Sinusoidal rolling rates for different rolling rate amplitudes

As it is shown in Figure 5.55, simulations are performed to complete 4 periods. Two different Mach numbers are examined in details for better understanding the effects of rolling rate amplitude on dynamic rolling motion. One of them is at subsonic and the other one is at supersonic flow regime. Time histories of rolling moment

coefficients belonging to different rolling rate amplitude simulations for Mach number 0.7 are given in Figure 5.56.

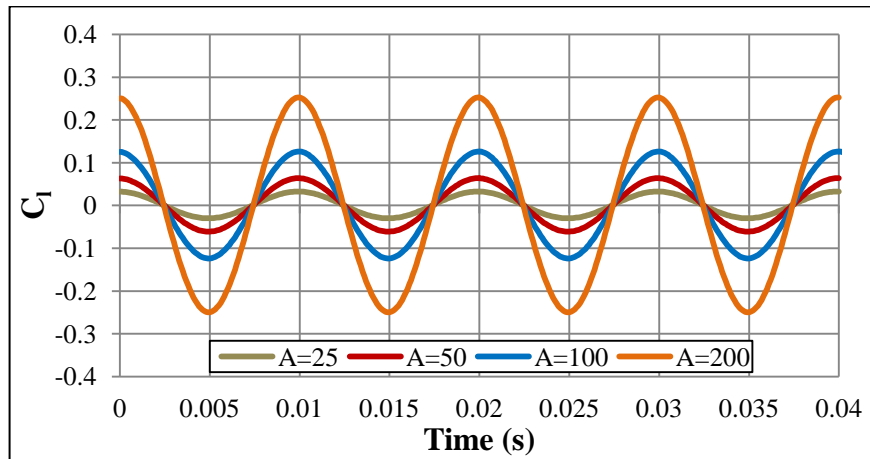


Figure 5.56 Rolling moment coefficient vs. time for different rolling rate amplitudes (BF model, Mach=0.7)

As it is shown in above figure, the initial conditions given to the dynamic motion simulations seem to be good because no oscillations are seen at the beginning of the simulations. It can also be concluded that the proper time step size is given to the model because smooth sinusoidal waves are seen throughout the simulations. In addition to this, the simulations are converged before completing the four periods. The changes of rolling moment coefficients with roll angles for Mach number 0.7 are shown in Figure 5.57.

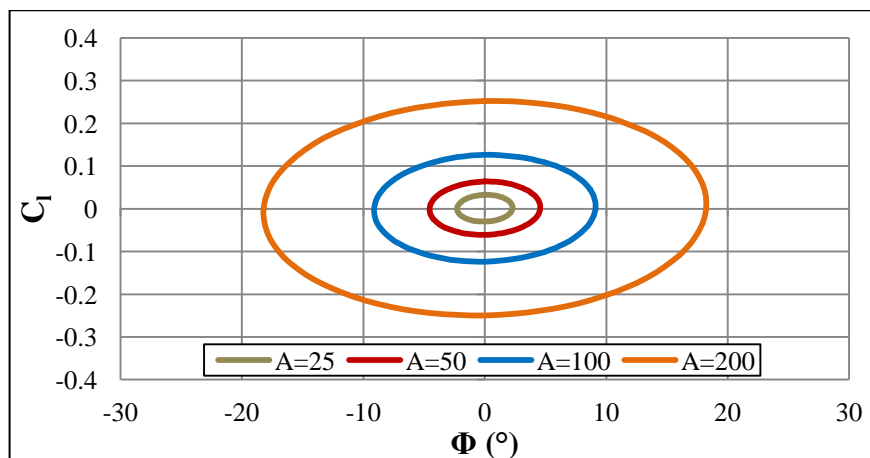


Figure 5.57 Rolling moment coefficient vs. roll angle for different rolling rate amplitudes (BF model, Mach=0.7)

Different from the pitching motion simulations, the model is exposed to large roll angles. Moreover, different from pitching moment coefficient, rolling moment coefficient does not have linear trends with roll angles. In other words, the pitching moment coefficient increases in magnitude as the angle of attack increases whereas the rolling moment coefficient does not increase in magnitude as the roll angle increases. Further, the model has closer rolling moment values for the same magnitude of positive and negative roll angles. Therefore, the change of rolling moment coefficients with roll angles seems like a circle as it is seen in Figure 5.57. Besides, as expected, bigger circular curves occur with bigger rolling rate amplitude simulations. The changes of dynamic rolling moment coefficients with reduced frequencies for all different rolling rate amplitude simulations are given in Figure 5.58.

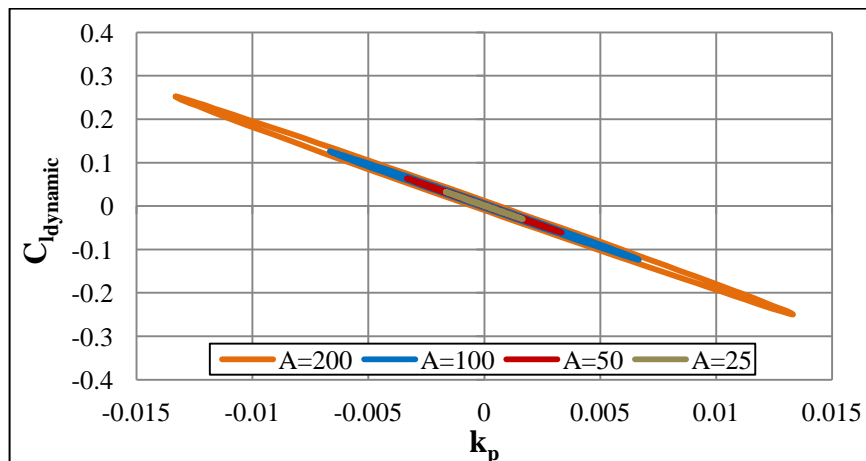


Figure 5.58 Dynamic rolling moment coefficient vs. reduced frequency for different rolling rate amplitudes (BF model, Mach=0.7)

All the dynamic rolling moment coefficients belonging to different rolling rate amplitude simulations are almost changing linearly with reduced frequencies. All these curves lie on the same linear curves. The only difference between these dynamic rolling moment coefficient curves is their lengths. Therefore, it can be concluded that the assumption of linear change in dynamic rolling moment coefficient vs. reduced frequency curves is valid for subsonic flows and for these pitching rate amplitudes. Moreover, the roll damping coefficient calculated with these results are expected to be same as each other.

Time histories of rolling moment coefficients for different rolling rate amplitude simulations carried out for second case which is Mach number 1.5 are given in Figure 5.59.

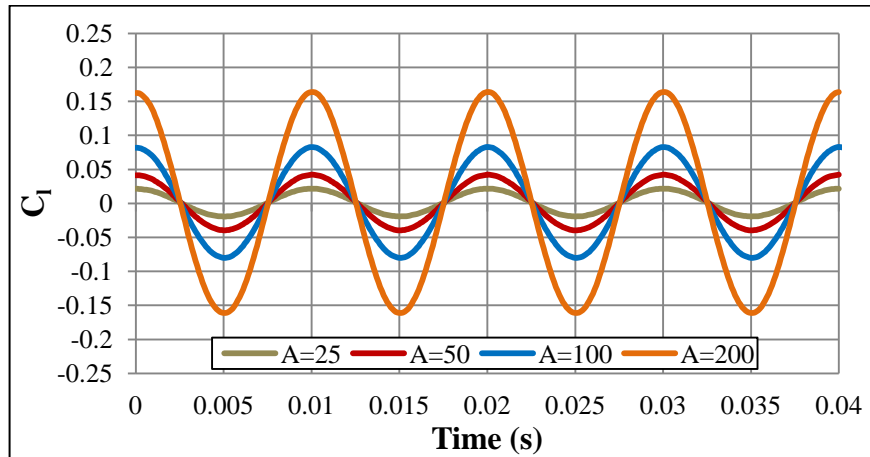


Figure 5.59 Rolling moment coefficient vs. time for different rolling rate amplitudes (BF model, Mach=1.5)

Similar to the subsonic case, the resultant rolling moment coefficients are like sinusoidal waves. The simulations also converge before completing the four periods. The changes of rolling moment coefficients with regarding rolling angles for the last period results of simulations done at Mach number 1.5 is given in Figure 5.60.

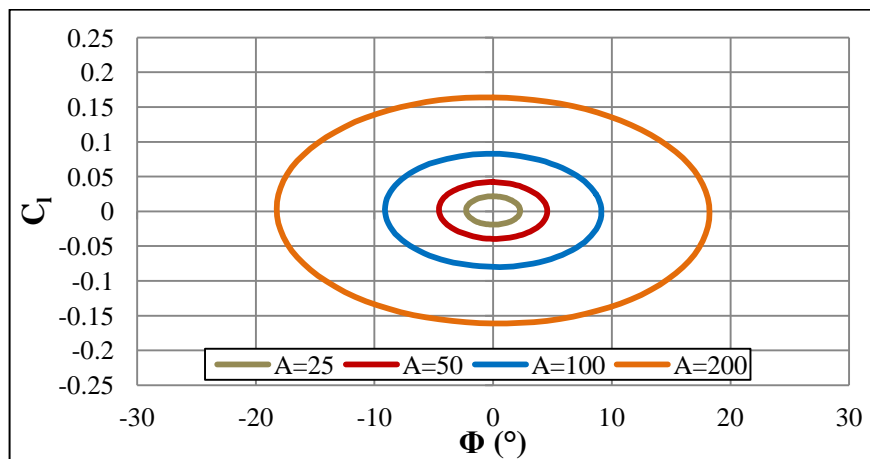


Figure 5.60 Rolling moment coefficient vs. roll angle for different rolling rate amplitudes (BF model, Mach=1.5)

As it is explained for the subsonic case, the circular curves of rolling moment coefficients shown in Figure 5.60 are expected. The characteristics of the curves are similar to the ones in subsonic case. The only difference between the curves is their magnitudes. The magnitude of the rolling moment coefficients at supersonic regime is smaller than the ones at subsonic regime. Therefore, it can be said that the characteristics of the curves do not change with flow regimes.

The changes of dynamic rolling moment coefficients with regarding reduced frequencies are given in Figure 5.61.

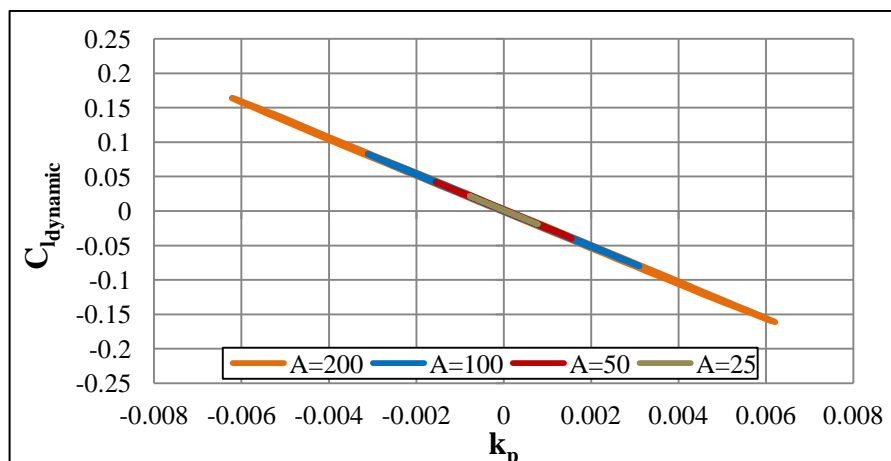


Figure 5.61 Dynamic rolling moment coefficient vs. reduced frequency for different rolling rate amplitudes (BF model, Mach=1.5)

As it is shown in Figure 5.61, the curves of dynamic rolling moment coefficients for different rolling rate amplitude simulations are exactly linear. In addition, all the curves have the same slope. Therefore, the roll damping coefficients calculated from these rolling rate amplitude simulations should be same. Again, as that of subsonic case, the assumption of linear change in dynamic rolling moment coefficient vs. reduced frequency curves is also valid for supersonic flows and for these pitching rate amplitudes.

The roll damping coefficients computed from different rolling rate amplitude simulations are presented in Figure 5.62.

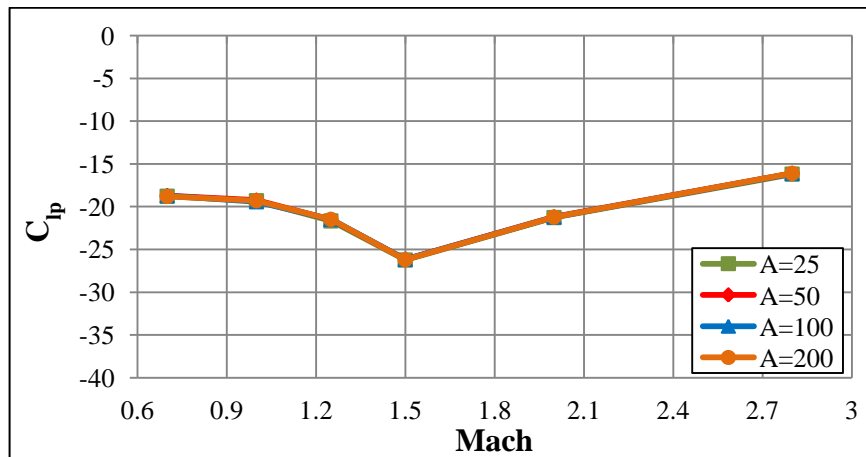


Figure 5.62 Roll damping coefficients of BF model for different rolling rate amplitudes

The roll damping coefficients calculated from different rolling rate amplitude simulations are exactly the same throughout the whole flow regime. The amplitude of rolling rate changes the magnitude of rolling moment coefficients and reduced frequencies. However, the slope of the dynamic rolling moment coefficient with reduced frequency does not change with the change of amplitudes of rolling rates. As a result of this parametric study, it can be concluded that the feasible amplitudes of rolling rates like the ones used in this study do not have any effects on roll damping coefficients.

5.4.2.2 Effects of Rolling Rate Frequency

In this part of the study, effects of rolling rate frequencies are investigated. Four different rolling rate frequencies are given to the BF model at different Mach numbers by keeping the rolling rate amplitude constant ($A=100$ rad/s). Similar to the parametric study conducted on rolling rate amplitudes, two different Mach numbers are examined in details for better understanding the effects of rolling rate frequency on dynamic rolling motion. One of them is at subsonic and the other one is at supersonic flow regime. The changes of rolling rate frequencies with time given to the BF model for the simulations are given in Figure 5.63.

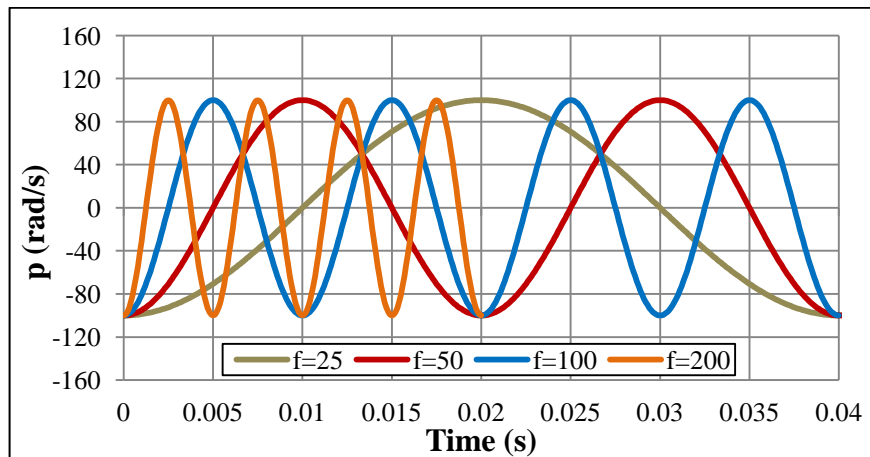


Figure 5.63 Sinusoidal rolling rates for different rolling rate frequencies

Simulations are performed to complete at least 3 periods. However, in Figure 5.63, only the 0.04 seconds of the rolling rates are shown for better illustration. The simulations performed with the frequencies of 25 and 50 Hz complete three periods and the simulations performed with the frequencies of 100 and 200 Hz complete four periods.

Time histories resultant rolling moment coefficients for Mach number 0.7 is shown in Figure 5.64.

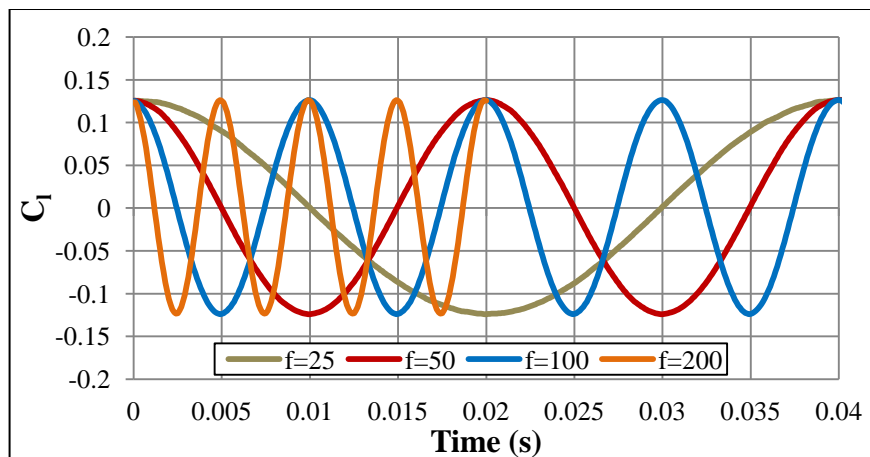


Figure 5.64 Rolling moment coefficient vs. time for different rolling rate frequencies (BF model, Mach=0.7)

Again only the 0.04 seconds of the simulation results are presented. As it is easily seen in Figure 5.64, no oscillations occur at the beginning of the simulations. The convergence is achieved at third periods for all rolling rate simulations.

The changes of resultant rolling moment coefficients with roll angles belonging to the last periods of the different rolling rate frequency simulations are presented in Figure 5.65.

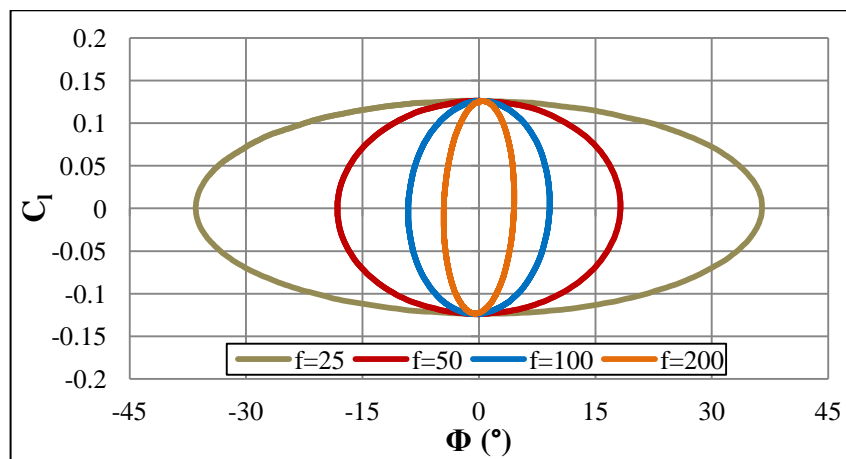


Figure 5.65 Rolling moment coefficient vs. roll angle for different rolling rate frequencies (BF model, Mach=0.7)

The curves of all different rolling moment coefficients belonging to the different roll rate frequencies have the same value at zero roll angles. This is because of having the same rolling rate amplitudes. The only difference between these curves is the exposed rolling angles. These differences are resulted from the differences in rolling rate frequencies.

The changes of dynamic rolling moment coefficients with reduced frequencies for Mach number 0.7 for all rolling rate frequency simulations are shown in Figure 5.66.

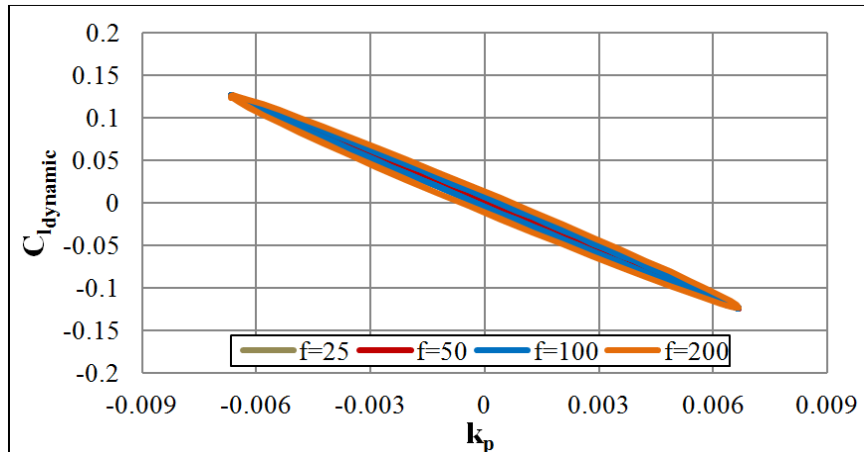


Figure 5.66 Dynamic rolling moment coefficient vs. reduced frequency for different rolling rate frequencies (BF model, Mach=0.7)

Small hysteresis is seen for the case having the frequency of 200 Hz. The other cases having smaller frequencies have linear trends and these results are consistent with the linear change assumptions. Therefore, it can be concluded that the frequencies smaller than 200 Hz are more convenient for roll damping coefficient calculations for the subsonic flow problems. Time histories of rolling moment coefficients for Mach number 1.5 are shown in Figure 5.67.

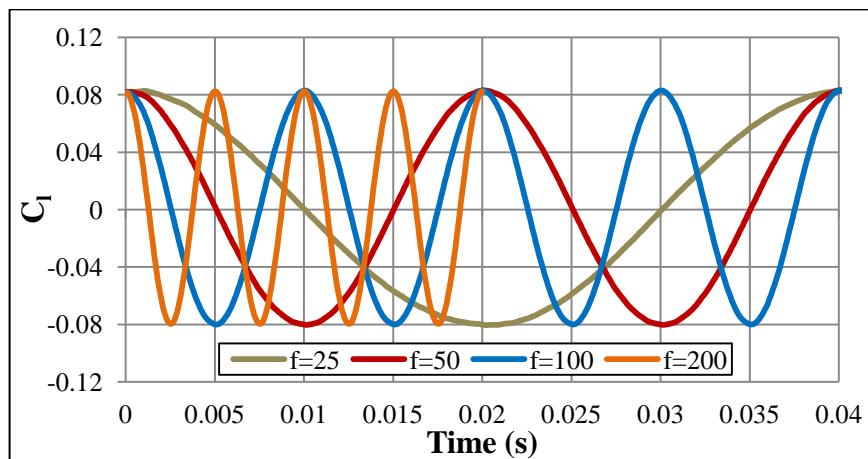


Figure 5.67 Rolling moment coefficient vs. time for different rolling rate frequencies (BF model, Mach=1.5)

Again only the 0.04 seconds of the simulation results are presented in Figure 5.67. No oscillations are seen at the beginning of the simulations. Moreover, the simulations converge at third periods for all rolling rates. The maximum resultant

rolling moment coefficients for all different rolling rate frequencies are nearly the same as each other. The changes of rolling moment coefficients with rolling angles belonging to different rolling rate frequency simulations carried out at Mach number 1.5 is given in Figure 5.68.

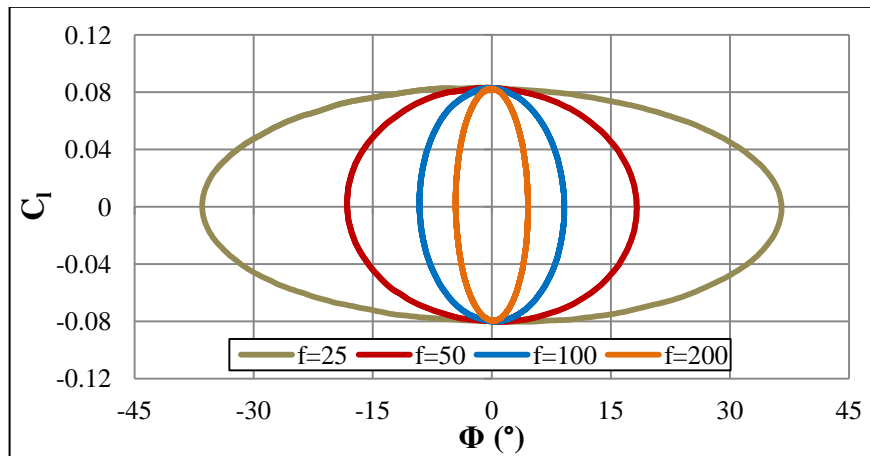


Figure 5.68 Rolling moment coefficient vs. roll angle for different rolling rate frequencies (BF model, Mach=1.5)

The resultant rolling moment coefficients have the same values at zero roll angles. The characteristics of the curves belonging to different rolling rate frequency simulations are similar to the ones at subsonic flow. Only the magnitudes of the curves exhibit differences. The effects of rolling rate frequencies on dynamic rolling moment coefficient vs. reduced frequency curves are shown in Figure 5.69.

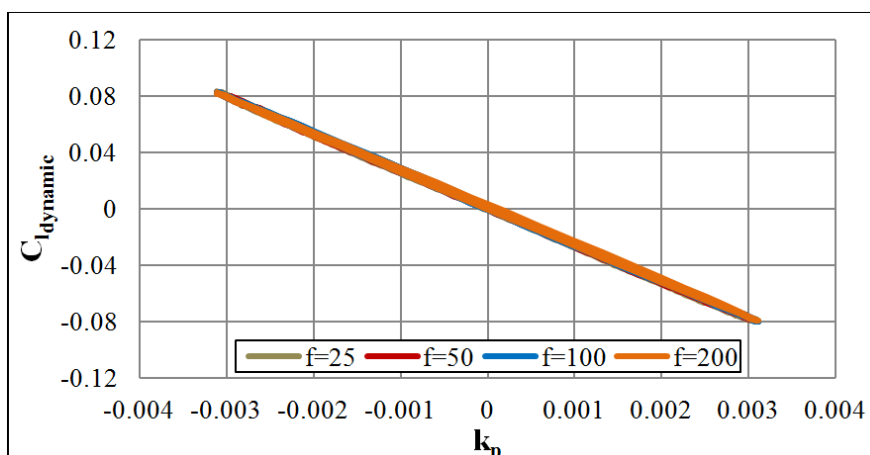


Figure 5.69 Dynamic rolling moment coefficient vs. reduced frequency for different rolling rate frequencies (BF model, Mach=1.5)

Distinct from the subsonic case, all the resultant dynamic rolling moment coefficients change linearly with reduced frequencies. The curves of dynamic rolling moment coefficients also lie on the same line. In other words, the roll damping coefficients calculated from these different rolling rate frequency simulations should be exactly the same as each other.

In Figure 5.70, the computed roll damping coefficients belonging to different rolling rate frequency simulations are compared with each other.

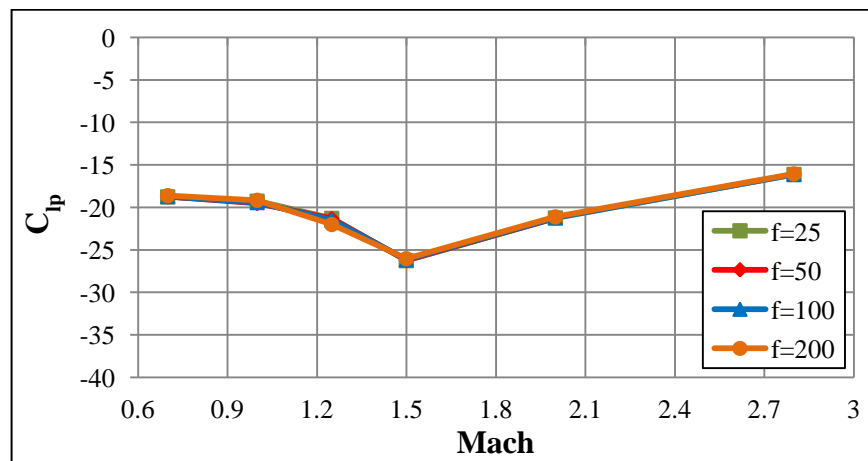


Figure 5.70 Roll damping coefficients of BF model for different rolling rate frequencies

As it is shown in above figure the roll damping coefficients belonging to different rolling rate frequency simulations are nearly the same as each other. Small differences are seen at Mach number 1.25. However, these differences are too small and negligible. As a result of parametric study carried out on rolling rate frequency, it is seen that the rolling rate frequency does not have any effects on roll damping coefficients. It only changes the magnitude of the exposed roll angle. Moreover, it can be concluded that roll damping coefficients of missiles can be calculated by using any feasible rolling rate frequencies similar to the ones presented in this study.

5.4.2.3 Effects of Angle of Attack

Same procedure used for rolling motion simulations at zero angle of attack is also used for rolling motion simulations performed at any angle of attacks. The only difference is that the angle of attack information defined to the pressure far field boundary conditions.

It is found in literature that MBF model has experimental data at small angles of attack ranging from -5 to 7 degree at Mach numbers 0.6 and 1.75 [7][7]. In this part, only the supersonic case is investigated in details and the results of subsonic and supersonic cases are compared with experimental data in the following part. The rolling rate amplitude of 100 rad/s and rolling rate frequency of 100 Hz are used in the rolling motion simulations.

Time histories of rolling moment coefficients belonging to the simulations conducted at different angle of attacks are shown in Figure 5.71.

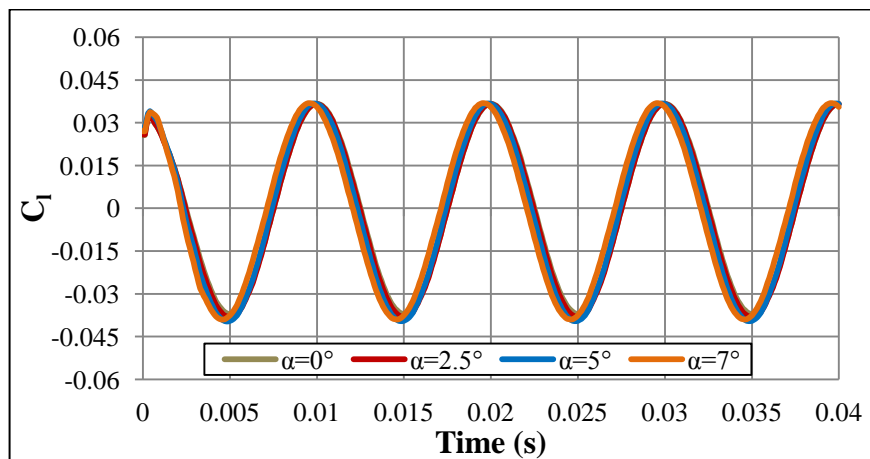


Figure 5.71 Rolling moment coefficient vs. time for different angle of attacks (MBF model, Mach=1.75)

The maximum and minimum rolling moment coefficients are nearly the same as each other for all angle of attack simulations. However, small shifts are seen in the curves and thus the maximum-minimum points of the sinusoidal curves occur at different time steps.

The changes of rolling moment coefficients with roll angles belonging to the last periods of simulations are given in Figure 5.72.

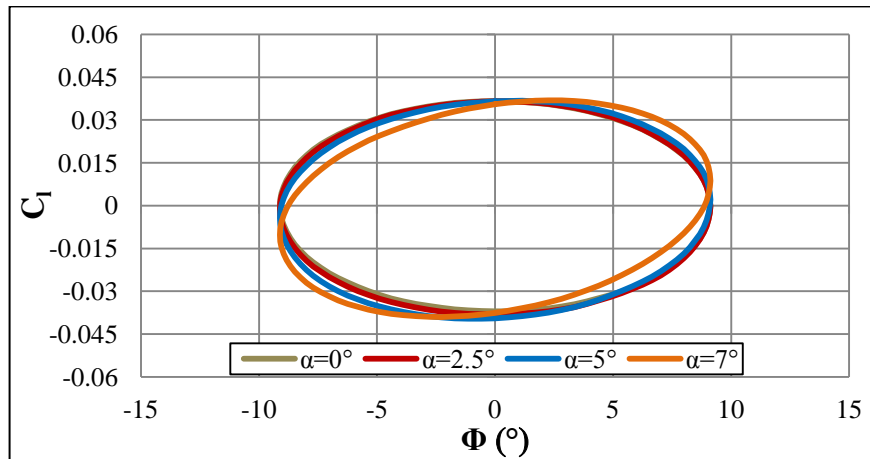


Figure 5.72 Rolling moment coefficient vs. roll angle for different angle of attacks (MBF model, Mach=1.75)

The rolling moment coefficients vs. roll angle curves show different characteristics for different angle of attacks. These differences are clearly seen at 7 degree angle of attack results. The changes of dynamic rolling moment coefficients vs. reduced frequencies for different angle of attack simulations are given in Figure 5.73.

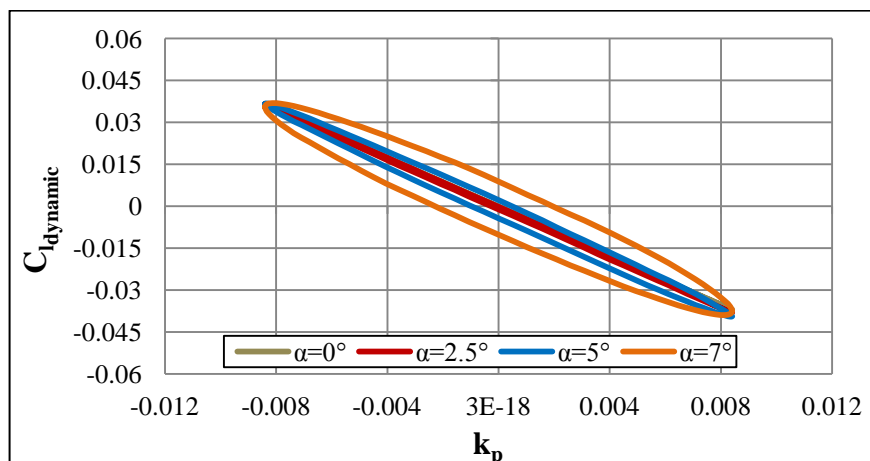


Figure 5.73 Rolling moment coefficient vs. reduced frequency for different angle of attacks (MBF model, Mach=1.75)

The maximum and minimum points of the curves are nearly the same as each other. However, the trends of the curves are totally different. As the angle of attack

increases, the hystereses of dynamic rolling moment coefficient vs. reduced frequency curves increase. The assumption of linear variation of dynamic rolling moment coefficient vs. reduced frequency cannot be accepted for seven degree angle of attack simulation. Therefore, it can be concluded that, for the simulations conducted at angle of attacks greater than five degree, the assumption of linear variation is not valid.

5.4.2.4 Results

The comparisons of numerical and experimental results are presented here. Firstly, the roll damping coefficients of BF model at zero angle of attack is compared with available free flight test data. Then, the effects of angle of attack on roll damping coefficient are analyzed with MBF model which has experimental data at subsonic and supersonic flow regimes. The comparison of computed roll damping coefficients with experimental data for BF model is presented in Figure 5.74.

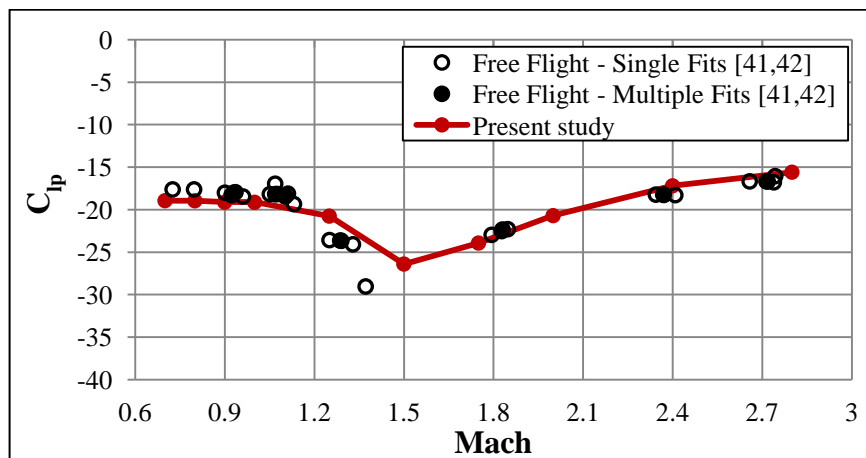


Figure 5.74 Roll damping coefficient vs. Mach number (BF model, $\alpha=0^\circ$)

Unlike pitch damping coefficients, the experimental data of roll damping coefficient for BF model has no discrepancies. The experimental results are very close to each other throughout the whole flow regime. As it is obviously seen in Figure 5.74 that the numerical results presented in this study shows good agreement with experimental data. It can be obviously concluded from these results that the

numerical method explained in this study can be used for the prediction of roll damping coefficient of missiles at zero angle of attack throughout the whole flow regimes. The effects of angle of attack on roll damping coefficient are analyzed in details before. Here, the computed results at Mach number 0.6 and 1.75 are compared with experimental data in Figure 5.75 and Figure 5.76.

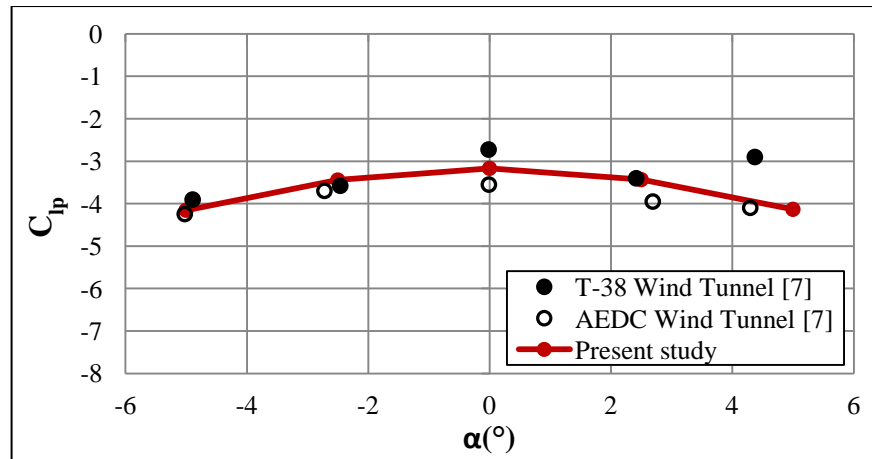


Figure 5.75 Roll damping coefficient vs. angle of attack (MBF model, Mach=0.6)

As it is expected symmetric behaviors with respect to angle of attack are seen in numerical and experimental results. The computed results are in good agreement with the experimental data obtained from different wind tunnels. Here, the remarkable point is the increase in magnitude of roll damping coefficient with the increase in magnitude of angle of attack. However, it should not be forgotten that these results are valid at small angle of attacks at subsonic flows. At large angle of attacks and different flow regimes the characteristics of roll damping coefficient may show different behaviors.

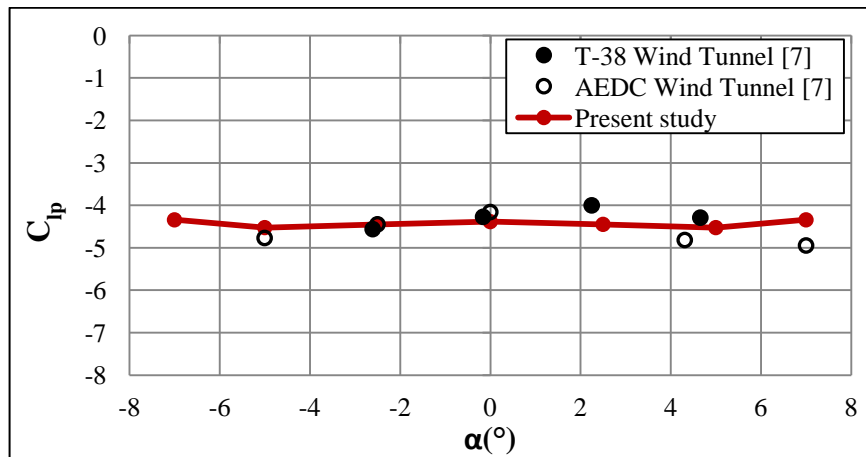


Figure 5.76 Roll damping coefficient vs. angle of attack (MBF model, Mach=1.75)

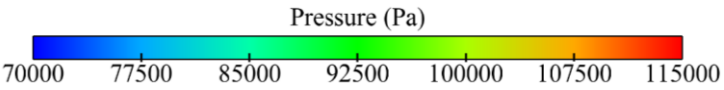
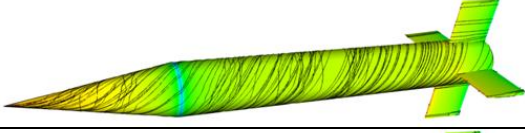
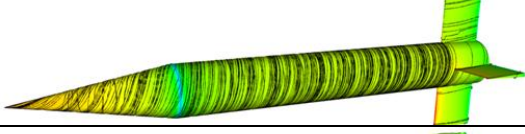
As that of subsonic case, the numerical and experimental results are symmetric with respect to angle of attack. Again, the computed results are in good agreement with experimental data for all angles of attacks. In this case similar to the subsonic one, the magnitude of roll damping coefficients increase with the increase in magnitude of angle of attack up to five degree. However, at seven degree angle of attacks numerical results show different characteristics as compared to the experimental results. This may be resulted from the non-linearity of the dynamic rolling moment coefficient vs. reduced frequency curves. Therefore, it can be said that by using the numerical method presented in this study, the roll damping coefficients can be calculated accurately up to five degree angle of attacks. The simulations having greater angle of attacks may give unreliable and inaccurate results.

To sum up, the computed results of roll damping coefficients for both models at different Mach numbers and angle of attacks up to five degree show good agreement with experimental data. By using the feasible rolling rate amplitudes and frequencies, the numerical method of roll motion simulation presented in this study can be used for the prediction of roll damping coefficient for all missile configurations.

5.4.2.5 Flow Field Visualization

In order to better understand the characteristics of rolling motions, the flow field analyses are performed for one case. The rolling motion of BF model at Mach number 0.7 and zero angle of attack is examined in details. In flow field analyzes the expected and the resultant flow features are compared with each other. For this purpose, it is focused on the expected and the resultant values of the surface flow and roll angles (position in fins). The examined case has rolling rate amplitude of 200 rad/s and rolling rate frequency of 100 Hz. The changes of pressure and surface flow over BF model at specified time steps are given in Table 5.2.

Table 5.2 Pressure distribution and surface flow on BF model (Mach=0.7, A=200 rad/s, f=100 Hz)

Roll Rate and Roll Angle	
Time = 0.001 s p = -161.80 rad/s $\Phi = -10.72^\circ$	
Time = 0.003 s p = 61.80 rad/s $\Phi = -17.35^\circ$	
Time = 0.005 s p = 200 rad/s $\Phi = 0^\circ$	
Time = 0.007 s p = 61.80 rad/s $\Phi = 17.35^\circ$	
Time = 0.009 s p = -161.80 rad/s $\Phi = 10.72^\circ$	

The period of the rolling motion is 0.01 seconds (f=100 Hz) and the rolling motion starts at zero roll angle.

At 0.001 second, the model is exposed to a decreasing rolling rate of -161.8 rad/s. Due to this rolling rate it is expected to have a roll angle of -10.72 degree. The surface flows and the position of the model given in figure in Table 5.2 seems to be consistent with expected values.

At 0.003 second, the model has to finish the quarter period and start to roll on opposite directions. The surface flows and positions of the model shown in figure given in Table 5.2 are in good agreement with the expected values.

At 0.005 second, the model should finish the half of the period and be on the initial position. Therefore, it is expected to have zero roll angles and rolling rate of 200 rad/s. The positions and surface flow shown in figure given in Table 5.2 is totally agreed with the expected physical behavior.

At 0.007 second, the model is about to finish the 3 quarter periods. It should have a decreasing rolling rate of 61.8 rad/s and roll angle of 17.35 degree. The positions of the fins shown in figure in Table 5.2 agree with the computed values. The surface flows of the figures also seem physically meaningful.

At 0.009 second, the model is about the finish the one period of the motion. It is expected to have a decreasing rolling rate of -161.8 rad/s and roll angle of 10.72 degree. The surface flows of the model at this time step is expected to be similar with the ones at time step 0.001. Because, these two time steps have the same rolling rate amplitudes. The only difference between these time steps is that one has a decreasing rolling rate and the other one has an increasing rolling rate. In addition, the roll angles at these time steps should be same values with opposite signs. The expected values of flow features are consistent with the ones in figures given in Table 5.2.

To sum up, the figures shown in Table 5.2 show that the model does the same motion as it is defined to do. The surface flows and positions of the models are exactly the same as expected values.

Rolling moment coefficients are almost resulted from the fins of the models. Because, the cross sectional area of the model exposed to the flow directions of rolling motion mostly resulted from the fins. The differences of static pressures between the sides of fins during the rolling motion at specified time steps are given in Figure 5.77 for better illustrating the origination of rolling moment coefficients.

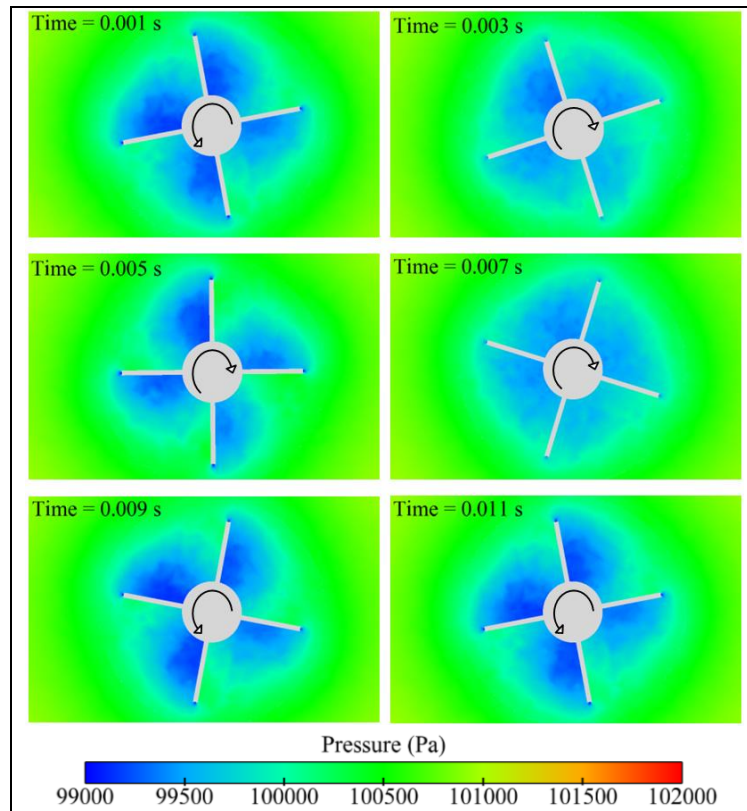


Figure 5.77 Pressure distribution at the back of the BF model (Mach=0.7, $A=200$ rad/s, $f=100$ Hz)

The low pressure regions occur at the back side of the fins according to the rolling motion directions. Moreover, the biggest pressure differences are seen for the time steps where the rolling rates have bigger values. At 0.003 second where the model has an increasing rolling rate, the differences in static pressure also tend to increase. At 0.007 second where the model is about to stop and return to another direction, the low pressure region is seen at both sides of the fins. To sum up, the features of static pressure seen in Figure 5.77 are totally consistent with expected values and also physically meaningful.

CHAPTER 6

CONCLUSION AND DISCUSSION

In this study, as it is done in wind tunnels, forced-oscillation motion is given to the test case models to predict the pitch and roll damping coefficients. In order to understand the characteristics of dynamic pitching and rolling motions of missiles, parametric studies are carried out. The amplitude and frequency of forced-oscillation motion are investigated one by one. In addition to this, the effects of angle of attacks are investigated for both pitching and rolling motions.

As a result of parametric study on pitching rate amplitude, it is seen that the exposed angle of attack resulting from the pitching rate amplitude should be less than one degree. Because, at angle of attacks greater than one degree, the assumption of linearity of the dynamic pitching moment coefficient vs. reduced frequency curve fails. It is also concluded that the pitch damping coefficient is independent of pitching rate amplitudes in feasible ranges like the ones presented in this study.

It is obviously seen from the comparison of numerical and experimental results that the pitch damping coefficient is independent of pitching rate frequency with proper pitching rate amplitude. The assumption of linearity of dynamic pitching moment coefficient vs. reduced frequency curve is also valid for feasible pitching rate frequencies. The important point is that the pitching rate frequency and amplitude should be selected such that the exposed angle of attack should be less than one degree. As a result of parametric study conducted on pitching rate frequencies, it can be concluded that any feasible pitching rate frequencies as the ones investigated in this study can be used for the calculation of pitch damping coefficient.

No change in pitch damping coefficient is observed at small angle of attacks. However, at angle of attacks greater than eight degree, the magnitude of pitch damping coefficient increases with an increasing angle of attacks. Same trend is seen in both numerical and experimental results. The numerical and experimental results are close to each other throughout the whole angle of attack range. As a result, the numerical method of dynamic pitching motion simulations is also valid for the whole angle of attack range.

The roll damping coefficients calculated from different rolling rate amplitude simulations are exactly the same as each other. The amplitude of rolling rate changes the magnitude of rolling moment coefficients and reduced frequencies. However, the slope of dynamic rolling moment coefficient with reduced frequency curve does not change with the change of amplitude of rolling rates. As a result of this parametric study, it can be concluded that the feasible amplitudes of rolling rates like the ones used in this study do not have any effects on roll damping coefficients.

Roll damping coefficients belonging to different rolling rate frequency simulations are nearly the same as each other. Small differences are seen at transonic flow regime. However, these differences are too small and negligible. As a result of parametric study carried out on rolling rate frequency, it is seen that the rolling rate frequency does not have any effects on roll damping coefficients. It only changes the magnitude of the exposed roll angle. Moreover, it can be concluded that roll damping coefficients of missiles can be calculated by using any feasible rolling rate frequencies similar to the ones presented in this study.

As it is expected symmetric behaviors with respect to angle of attack are seen in numerical and experimental results. The computed results are in good agreement with the experimental data obtained from different wind tunnels. The remarkable point is the increase in magnitude of roll damping coefficient with the increase in magnitude of angle of attack up to five degree. However, at seven degree angle of attacks numerical results show different characteristics as compared to the experimental results. This may be resulted from the non-linearity of the dynamic

rolling moment coefficient vs. reduced frequency curves. Therefore, it can be said that by using the numerical method presented in this study, the roll damping coefficients can be calculated accurately up to five degree angle of attack. The simulations having greater angle of attacks may give unreliable and inaccurate results.

To sum up, in this study, pitch and roll damping coefficients of missiles are numerically investigated in details. The parametric studies of amplitude and the frequency of forced oscillation motions are tried on two different 3D test case models. The effects of angle of attacks on dynamic pitching and rolling motions are also investigated in details. These parametric studies reveal the general features of dynamic pitching and rolling motions. After deeply understanding the general characteristics of dynamic motions, numerical results of pitch and roll damping coefficients are compared with the experimental data.

In conclusion, by using the numerical method presented in this study, pitch and roll damping coefficients of any missile configurations can be calculated accurately.

REFERENCES

- [1] Nielsen, J. N., “*Missile Aerodynamics*”, Vidya, Inc., Stanford Industrial Park, Palo Alto, California, 1960
- [2] Fleeman, E. L., “*Tactical Missile Design*”, AIAA Education Series, 2001
- [3] Kovar, A., Schülein, E., “*Effect of Side Jets in a Supersonic Cross Flow Measured and Calculated on a Flat Plate and a Generic Missile Configuration*”, Innovative Missile Systems (pp 37-1 – 37-14), 2006
- [4] Ağsarlıoğlu, E., “*Numerical Investigation of Lateral Jets for Missile Aerodynamics*”, Ms. Thesis, METU, 2011
- [5] George, P. S. , Oscar, B., “*Rocket Propulsion Elements*”, 7th Edition
- [6] Samardzic, M., Anastasijevic, Z., Marinkovski, D. “*Some Experimental Results of Subsonic Derivative Obtained in the T-38 Wind Tunnel by Forced Oscillation*”, Scientific Technical Review, Vol. LVII, NO. 3-4, 2007
- [7] Anastasijevic, Z., Samardzic M., Marinkovski, D., Vrtlar, S., Rodic, M., “*Determination of the T-38 Wind Tunnel Oscillatory Data of the Dynamic Calibration Missile Model*”, Scientific Technical Review, Vol. LIX, NO. 2, 2009
- [8] Bhagwandin, V. A., Sahu, J., “*Numerical Prediction of Pitch Damping Stability Derivatives for Finned Projectiles*”, AIAA 2011-3028, June 2011
- [9] Anderson, J. D., “*Introduction to Flight*”, 3rd Edition, McGraw-Hill., 1989
- [10] Kayabaşı, İ., Akgül, A., and Sunay, Y. E., “*Computational Fluid Dynamics Prediction of Pitch and Roll Damping for the Missile Models and Comparison with Experiment*”, OTEH 2011 On Defensive Technologies, Belgrade, Serbia, October 2011
- [11] Danberg, J. E., Weinacht, P., “*An Approximate Method for Pitch-Damping Prediction*”, ARL-TR-3007, July 2003
- [12] Weinacht, P., “*Navier-Stokes Predictions of the Individual Components of the Pitch-Damping Coefficient Sum*”, ARL-TR-3169, April 2004

- [13] Weinacht, P. and Danberg, E. J., “*Prediction of the Pitch-Damping Coefficients Using Sacks’s Relations*”, Journal of Spacecraft and Rockets, Vol. 42, No. 5, September–October 2005
- [14] Park, S. Y., Kwon, J. H., “*Prediction of Damping Coefficients Using the Unsteady Euler Equations*”, Journal of Spacecraft and Rockets, Vol. 40, No. 3, May–June 2003
- [15] Park, S. Y., Kwon, J. H., “*Navier–Stokes Computation of Pitch–Damping Coefficients Using Steady Coning Motions*”, Journal of Spacecraft and Rockets, Vol. 41, No. 5, September–October 2004
- [16] Murman, S. M., “*Reduced-Frequency Approach for Calculating Dynamic Derivatives*”, AIAA Journal, Vol. 45, No 6, June 2007
- [17] Sahu, J., “*Numerical Computations of Dynamic Derivatives of a Finned Projectile Using a Time-Accurate CFD Method*”, AIAA 2007-6581, August 2007
- [18] Sahu, J., “*Time-Accurate Numerical Prediction of Free-Flight Aerodynamics of a Finned Projectile*”, Journal of Spacecraft and Rockets, Vol. 45, No. 5, September–October 2008
- [19] DeSpirito, J., Sifton, S. I., Weinacht, P., “*Navier-Stokes Predictions of Dynamic Stability Derivatives: Evaluation of Steady-State Methods*”, ARL-TR-4605, September 2008
- [20] Moore, F. G., Moore, L. Y., “*New Methods to Predict Nonlinear Pitch Damping Moments*”, Journal of Spacecraft and Rockets, Vol. 45, No. 3, May–June 2008
- [21] Sifton, S. I., “*Navier-Stokes Predictions of Aerodynamic Coefficients and Dynamic Derivatives of a 0.50-cal Projectile*”, AIAA 2011-3030, June 2011
- [22] Lizhi, Y., Minghai, W., and Zhenghong, G., “*Numerical Investigation of Unsteady Aerodynamic Characteristics of a Pitching Missile*”, Aerospace Science and Technology, July 2010
- [23] Göngç, O. L., “*Computation of External Flow Around Rotating Bodies*”, Phd Thesis, METU, March 2005
- [24] Morote, J., and Liano, G., “*Prediction of Nonlinear Rolling and Magnus Coefficients of Cruciform-Finned Missiles*”, Journal of Aircraft, August 2010

- [25] DeSpirito, J., and Heavey, K., R., “*CFD Computation of Magnus Moment and Roll Damping Moment of a Spinning Projectile*”, AIAA 2004-4713, August 2004
- [26] Moore, F. G., Moore, L. Y., “*New Methods to Predict Nonlinear Roll Damping Moments*”, Journal of Spacecraft and Rockets, Vol. 45, No. 5, September-October 2008
- [27] Hirt, C. W., Amsden, A. A., and Cook, J. L., “*An Arbitrary Lagrangian-Eulerian Computing Method for All Flow Speeds*”, Journal of Computational Physics, Vol. 14, No. 3, pp.227-253, March 1974
- [28] Hughson, M., “*A 3-D Unstructured CFD Method for Maneuvering Vehicles*”, Mississippi State University, December 1998
- [29] White, F., M., “*Viscous Fluid Flow*”, McGraw and Hill, 1991
- [30] “*FLUENT Theory Guide*”, ANSYS Inc.,2009
- [31] Kayabaşı İ., Akgül A., Kurtuluş D., F., “*NACA0012 Kanat Profili için Sinusoidal Yunuslama Hareketinin Hesaplamalı Akışkanlar Dinamiği ile Modellenmesi*”, UHUK-2012-078, September 2012
- [32] “*Compendium of Unsteady Aerodynamic Measurements*”, AGARD-R-702, August 1982
- [33] “*GAMBIT 2.3 User Guide*”, ANSYS, Inc.,2006
- [34] “*TGRID 3.6 User Guide*”, Fluent, Inc., 2004
- [35] Hoffmann, K. A., “*Computational Fluid Dynamics Vol. 3*”, Engineering Education System, Wichita, 2000
- [36] “*Modeling Turbulent Flows with FLUENT*”, Dr. Aleksey Gerasimov, ANSYS Inc., October 2006
- [37] Uygun, M., & Tuncer, İ. H., “*A Computational Study of Subsonic Flows over a Medium Range Cargo Aircraft*”. 21st Applied Aerodynamic Conference, Orlando, Florida, AIAA 2003-3661, 23-26 June 2003
- [38] “*FLUENT User Guide*”, ANSYS Inc.,2009
- [39] Samardzic, M., Anastasijevic, Z., Marinkovski, D., Isakovic, J., and Curcic, D., “*The Sting Plunging Effect on Measured Pitch Damping Derivative*”, OTEH 2011 On Defensive Technologies, Belgrade, Serbia, October 2011

- [40] Uselton, B. L., and Uselton, J. C., “*Test Mechanism for Measuring Pitch Damping Derivatives of Missile Configurations at High Angles of Attack*”, AEDC Technical Report, AEDC-TR-75-43, May 1975
- [41] Sahu, J., K. R. Heavey, and E. N. Ferry, “*Computational Fluid Dynamics for Multiple Projectile Configurations*”, Proceedings of the 3rd Overset Composite Grid and Solution Technology Symposium, Los Alamos, NM, October 1996
- [42] Sahu, J., K. R. Heavey, and C. J. Nietubicz, “*Time-Dependent Navier-Stokes Computations for Submunitions in Relative Motion*”, 6th International Symposium on Computational Fluid Dynamics, Lake Tahoe, NV, September 1995